MATHEMATICAL MODELING, SIMULATION, AND OPTIMAL DESIGN OF PHARMACEUTICAL CRYSTALLIZERS

BY

MICHAEL LAWRENCE RASCHE

DISSERTATION

Submitted in partial fulfillment of the requirements
for the degree of Doctor of Philosophy in Chemical Engineering
in the Graduate College of the
University of Illinois at Urbana-Champaign, 2015

Urbana, Illinois

Doctoral Committee:

Professor Richard D. Braatz, Chair
Professor Paul J. A. Kenis
Professor Kenneth S. Suslick
Associate Professor Chris V. Rao

ABSTRACT

Crystallization is the most important purification process in the pharmaceutical industry. In addition to purification, this process can generate solid particles for incorporation with excipients into drug products such as tablets with precisely tunable quantities of active pharmaceutical ingredients. The mathematical modeling and simulation of crystallization processes are useful in systems engineering, with the key conservation equation for the particle size distribution being a partial differential equation known as the *population balance equation*.

This thesis constructs population balance models for three distinct particulate processes:

1) the breakage of crystals due to ultrasonication,
2) a semi-batch anti-solvent crystallization, and
3) continuous slug-flow crystallization,

which are solved by three distinct simulation methods:

1) breakage matrix with integer arithmetic,
2) method of characteristics,
3) method of moments combined with the method of lines.

The population balance models are also employed for three different engineering purposes: kinetics estimation, steady-state process design, and the design of dynamic feedback control structures.

Comparisons to experimental data are made where possible to keep the simulations relevant and grounded in reality. Simulations 1 and 3 are the first to simulate their corresponding processes. Simulation 2 provides a method to substantially reduce experimental costs for the estimation of crystallization kinetics that is contrary to the current literature. All three studies employ mathematical models to advance crystallization technology.

ACKNOWLEDGMENTS

I have many people to thank for helping to make this document a reality. To my advisor, Richard Braatz, for the countless hours of discussion covering, but not limited to, all the research published here, for allowing me the time that I needed to complete my work, and for being a friend. To my wife, Kate, and the rest of my family, for your love, belief, and encouragement. To the past and current Braatz group, especially Ashlee Ford Versypt, Xiaoxiang Zhu, and Kwang-Ki Kim, for keeping me on track and moving forward. To my collaborators, especially Mo Jiang, Jose Tabora, and Brad Zieger, for sharing your expertise (and data). To my housemates, Scott Parker, James Eddy, and Ana Martinez, for helping me enjoy graduate school. To the rest of my family, friends, and co-workers for your constant support, I offer my sincerest thanks and best wishes.

Funding for my research over the years was provided by the University of Illinois, Eli Lilly, Bristol-Myers Squibb, and Novartis. Without their financial assistance, none of this would be possible.

TABLE OF CONTENTS

CHAPTER 1

INTRODUCTION

1.1 Motivation and Significance

Of current interest in the pharmaceutical industry – although not limited to that industry – is the purification of a compound by crystallization. Batch crystallizers have been extensively investigated both experimentally and computationally. The most accurate computational models solve the full population balance equation (PBE) coupled with computational fluid dynamics (CFD) and micromixing models (Woo et al., 2006; 2009) while much less computationally costly models make an assumption of well-mixedness within the crystallizer vessel to produce much faster estimates of the product crystal size distributions (CSDs) (Ma et al., 2002ab; Gunawan et al., 2004; 2008).

In recent years, the diminishing number of "blockbuster" drugs has caused pharmaceutical companies to investigate streamlining and increased yield during manufacturing in an effort to make medication more widely available and affordable as well as to maintain profit margins. Continuous crystallization can reduce costs compared to batch crystallization by using recycle streams to reuse expensive chemicals, and can increase yield and decrease production time by removing intermediate cleaning of the batch vessel. Continuous crystallization also has the possibility of greatly increased control of CSDs (Woo et al, 2011; Jiang et al., 2012).

1.2 Ultrasonic breakage

While the effects of ultrasound on crystals have been heavily investigated experimentally (Teipel et al., 2002; 2004; Devarakonda et al., 2004; Guo et al., 2007; Raman et al., 2008; Wagtervelt et al., 2011), population balance models that describe the effects of all physical parameters such as solution viscosity and applied power on the crystal size distribution have been lacking. Chapter 2 of this thesis presents some of the first population balance models for describing the crystal breakage that results from ultrasound. Dynamic models are developed for the particulate system of aspirin crystals dispersed in various solvents, dodecane, and silicon oils of known viscosity that were subjected to ultrasound to study the sonofragmentation that occurs due to cavitation when bubbles violently collapse, creating extreme conditions in the immediate vicinity of the bubbles (Doktycz & Suslick, 1990; Suslick et al., 1999). Population balance models are developed with three models for binary breakage events and cavitation rate proportional to the applied power and exponentially related to solvent viscosity. The resulting population balance models provide reasonable agreement with the experimental data (provided by Zieger & Suslick, 2011) over the ranges of applied power and solvent viscosity investigated, with nearly overlapping crystal size distributions for applied power between 10 and 40 W.

1.3 Parameter Estimation in Industrial Batch Crystallization

A crystallization model is developed for a seeded stirred-tank semi-batch crystallizer. In Chapter 3, the model is used to optimally estimate growth and nucleation kinetics from experimental values for solution concentration, solubility, and antisolvent addition as well as initial estimates of the crystal size distribution (CSD). A well-mixed crystallizer simulation code was modified to reflect the system design and operating conditions and simulate the evolution of

the CSD using the method of characteristics (McOwen, 2003) over the time that the experimental data were collected. An output function was created to quantify the goodness-of-fit for the model results with the intent of minimizing the sum squared error of the concentration calculated by the simulation compared to that obtained by experimentation at each available time over a set of kinetic parameters.

The eleven sets of experimental results (provided by Jose Tabora of Bristol Myers-Squibb) were limited because the only quantitative data were solution concentration, solubility, and antisolvent addition rate (no final or intermediate CSD were available). Usually limited data of this sort (i.e., when concentration is the only variable for comparison) results in a situation in which multiple sets of kinetic parameters fit the data equally well (Miller & Rawlings, 1994). In this case, with the quantity of data provided, optimal growth kinetic parameters were found that accurately modeled the desupersaturation of the system despite the lack of information with respect to the crystal size distribution.

1.4 Steady-State Model and Design of Slug Flow Crystallization

Inspired from recent experimental progress of continuous crystallizer designs based on air/liquid slug flow that generate crystals of target sizes at high production rates and low capital costs (Alvarez & Myerson, 2010; Lawton et al., 2009; Ferguson et al., 2010; Vacassy et al., 2000; Jiang et al., 2014; Eder et al, 2010; 2011), Chapter 4 presents the derivation of a mathematical model and the procedure for the design of slug-flow crystallizers (Jiang et al., 2014). Design variables for the cooling slug-flow crystallizer (e.g., tubing length, types and numbers of heat transfer methods) were analyzed and optimized for best product crystal quality

(e.g., minimized secondary nucleation and impurity incorporation) and experimental implementation (e.g., minimized equipment/material use).

1.5 Dynamic Modeling and Optimization of Slug-Flow Crystallization

The inclusion of a convective term in the population balance equation for a batch crystallization process (Alvarez & Myerson, 2010) leads to a model for the slug-flow crystallizer described in Chapter 4, involving multiple stages of counterflow shell-and-tube heat exchangers. The simulation uses the method of moments (Hulburt & Katz, 1964; Randolph & Larson, 1974) and the numerical method of lines to solve the resulting system of partial differential equations.

With the optimally designed system initially at steady-state conditions, design variables are perturbed to observe the dynamic effect on state variables throughout the system. From a control standpoint then, easily manipulated variables are chosen for their isolated (and ideally, large and fast) effect on measured variables indicative of the states of interest that result in the recovery of the system to the previous status of high-quality high-yield product streams.

CHAPTER 2

MODELING THE EVOLUTION OF A PARTICLE SIZE DISTRIBUTION DURING ULTRASOUND-INDUCED BREAKAGE

2.1 Introduction

The application of high-intensity ultrasound to crystallization has been an area of significant recent interest and has been developed as an effective technique for inducing nucleation and controlling particle size distributions. While the effects of ultrasound on crystals have seen some experimental investigation (Teipel et al., 2002; Devarakonda et al., 2004; Teipel et al., 2004; Guo et al., 2007; Raman et al., 2008, Wagtervelt et al., 2011), population balance models that describe the effecs of all physical parameters such as liquid viscosity and applied power on the crystal size distribution have been lacking Raman et al. (2011) demonstrated the application of Kapur function analysis to obtain grinding kinetics in a system of inorganic particles dispersed in water. Chapter 2 presents a different approach to modeling ultrasonic breakage for an organic system of a range of shorter times and lower ultrasound intensity and specifically investigates the effect of varying solvent viscosity.

Aspirin crystals dispersed in the nonsolvent dodecane were subjected to ultrasound to study this sonofragmentation, which occurs due to acoustic cavitation, which is the formation, growth, and implosive collapse of bubbles in an ultrasonic field. The final bubble collapse results in extreme local temperatures and pressures and prodecs high-pressure shockwaves that propagate through the liquid (Doktycz & Suslick, 1990; Suslick et al.,1999). The time evolution of the crystal size distribution is described be the population balance equation for breakage only with three models for binary breakage events: (A) crystals break

in half; (B) crystals break with uniform probability into each pair of sizes allowed by the discretization of the length axis; and (C) crystals break with non-uniform probability into each pair of sizes allowed by the discretization of length. Models A and B have two parameters that describe the breakage rate as a function of applied power and solvent viscosity, while Model C also includes a third parameter that is the standard deviation of the breakage about half the particle size.

This chapter presents the mathematical model and the experimental methods (Zeiger & Suslick, 2011) followed by results and discussion.

2.2 Population Balance Models

The experimental setup for the sonofragmentation experiments are shown in Figure 2.1 (Zeiger & Suslick, 2011). Nonsolvents dodecane (viscosity = 1.8 cSt) and silicone oil (viscosity = 20, 50, 100, 115, 154, 220, 244, 350, 500, and 1000 cSt) were used to disperse the crystals. Various power levels (3, 5 10, 20, 30, 40 W) were applied to the ultrasound horn for 1 minute which caused cavitation and resulted in crystal breakage.

Crystals were characterized in terms of circularity and surface area as measured via optical microscopy. The circularity, c, is defined as

$$c = \frac{4\pi a}{p^2} \tag{2.1}$$

where a is the surface area and p is the perimeter of the two-dimensional image of the crystal (Figure 2.1c). The crystal depth, d, defined as the shortest dimension, is estimated from the surface area and perimeter using a proportionality constant obtained from the scanning electron microscope (SEM) images assuming the particles have a similar shape.

$$d \approx \frac{a}{2.06p} \tag{2.2}$$

The mass, m, for each particle was calculated from

$$m = \rho a d \tag{2.3}$$

where ρ is the crystal density.

The sonofragmentation was modeled by the population balance equation (PBE) considering only breakage (Tan et al., 2004)

$$\frac{\partial}{\partial t}[n(t,m)] = \int_m^\infty S(u)b(m,u)n(t,u)du - S(m)n(t,m) \tag{2.4}$$

where S is the breakage rate, b is the breakage function, n is the number density function and m is the crystal mass. The breakage rate, S, in Equation 2.4 was assumed to follow the standard power-law function of the crystal mass (Tan et al., 2004):

$$S(m) = S_1 m^q, \quad q \geq 0 \tag{2.5}$$

where the selection rate constant, S_1, is related to the number of cavitation events by an efficiency factor, S_0 ,and the exponent, q, is expected to be non-negative as larger particles are more likely to come in contact with cavitation sites. The rate of cavitation has been reported to be proportional to the applied power over the ranges considered here (Colussi et al., 1999; Son et al., 2009). Experimentally, the cavitation rate was observed to be exponentially related to the liquid viscosity, η, (in cSt, see Figure 2.2). Combining these relationships provides an expression for S_1:

$$S_1 = S_0 \Pi \exp(-0.0069\eta) \tag{2.6}$$

where the applied power, Π , is in units of W.

2.3 Breakage Models

Here a procedure is described that greatly reduces the computational cost in simulation of the PBE for breakage (Equation 2.1). This matrix approach is similar to that developed for coal milling processes (Broadbent et al., 1956). The minimum crystal mass that can occur during the breakage experiments, $m_{\min}$, was chosen and the crystal mass data scaled so that $m_{\min} = 1$. The discretization of the crystal mass, m, was selected so that $\Delta m = m_{\min} = 1$, which results in all scaled crystal masses taking on integer values (Figure 2.3). Assuming that crystals break into two crystals of equal mass for even integer masses and nearly integer masses for odd integer masses (e.g., a crystal with a mass of 4 breaks into two crystals of mass 2; a crystal with a mass of 5 breaks into a crystal of mass 2 and a crystal of mass 3), the breakage function, b, in Equation 2.1 can be written as

$$b(m,u) = \begin{cases} 2, & u = 2m \\ 1, & u = 2m+1 \\ 1, & u = 2m-1 \\ 0, & \text{otherwise} \end{cases} \tag{2.7}$$

Discretizing the PBE (Equation 2.1) with respect to mass results in

$$\frac{\partial}{\partial t}[n(t,m_i)] = \begin{cases} 2S_1(2m_i)^q n(t,2m_i) + S_1(2m_i+1)^q n(t,2m_i+1), & i = 1 \\ 2S_1(2m_i)^q n(t,2m_i) + S_1(2m_i+1)^q n(t,2m_i+1) & \\ \quad + S_1(2m_i-1)^q n(t,2m_i-1) - S_1(m_i)^q n(t,m_i), & i = 1 < i < i_{\max}/2 \\ 2S_1(2m_i)^q n(t,2m_i) + S_1(2m_i-1)^q n(t,2m_i-1) & \\ \quad - S_1(m_i)^q n(t,m_i), & i = i_{\max}/2 \\ -S_1(m_i)^q n(t,m_i), & i_{\max}/2 < i \le i_{\max} \end{cases} \tag{2.8}$$

The time derivative is replaced with the first order forward difference approximation

$$\frac{\partial}{\partial t}[n(t,m_i)] \approx \frac{n(t_{j+1},m_i)-n(t_j,m_i)}{\Delta t} \tag{2.9}$$

with the initial condition determined by the mass distribution of unbroken crystals experimentally measured from the initial crystal size distribution (Figures 2.4–2.5). To prevent negative values for n from occurring due to discretization error for very high values of and in Equations 2.4–2.5, the timestep was set to satisfy

$$\Delta t \le \frac{1}{4S_1 m_{\max}^q} \tag{2.10}$$

Computations were carried out using MATLAB (Version 7.11.0.584). To increase computational efficiency in the implementation, the right hand side of Equation 2.4 was written as the product of a vector and a sparse matrix:

$$n(t_{j+1}) = n(t_j)A \tag{2.11}$$

where $n(t_j)$ is a row vector of length $i_{\max}$ and A is a lower diagonal square matrix of an interesting structure, with the 10×10 case being

$$A = \begin{bmatrix}
1 & 0 & 0 & 0 & 0 & 0 & 0 & 0 & 0 & 0 \\
2\beta_2 & 1-\beta_2 & 0 & 0 & 0 & 0 & 0 & 0 & 0 & 0 \\
\beta_3 & \beta_3 & 1-\beta_3 & 0 & 0 & 0 & 0 & 0 & 0 & 0 \\
0 & 2\beta_4 & 0 & 1-\beta_4 & 0 & 0 & 0 & 0 & 0 & 0 \\
0 & \beta_5 & \beta_5 & 0 & 1-\beta_5 & 0 & 0 & 0 & 0 & 0 \\
0 & 0 & 2\beta_6 & 0 & 0 & 1-\beta_6 & 0 & 0 & 0 & 0 \\
0 & 0 & \beta_7 & \beta_7 & 0 & 0 & 1-\beta_7 & 0 & 0 & 0 \\
0 & 0 & 0 & 2\beta_8 & 0 & 0 & 0 & 1-\beta_8 & 0 & 0 \\
0 & 0 & 0 & \beta_9 & \beta_9 & 0 & 0 & 0 & 1-\beta_9 & 0 \\
0 & 0 & 0 & 0 & 2\beta_{10} & 0 & 0 & 0 & 0 & 1-\beta_{10}
\end{bmatrix} \tag{2.12}$$

with the coefficients, β_i, specified by Equation 2.8. The matrix A consists of entries along the main diagonal and a band 3 entries wide centered in the lower diagonal part of A. Defining the matrix as sparse in MATLAB speeds up computations and decreases the memory requirement.

An alternative breakage model has each crystal breaking into two crystals according to a uniform distribution (by number) of each crystal mass smaller than the parent crystal. The matrix analogous to A for the 10×10 case is

$$B=\begin{bmatrix}
1 & 0 & 0 & 0 & 0 & 0 & 0 & 0 & 0 & 0 \\
2\alpha_2\beta_2 & 1-\beta_2 & 0 & 0 & 0 & 0 & 0 & 0 & 0 & 0 \\
\alpha_3\beta_3 & \alpha_3\beta_3 & 1-\beta_3 & 0 & 0 & 0 & 0 & 0 & 0 & 0 \\
\alpha_4\beta_4 & 2\alpha_4\beta_4 & \alpha_4\beta_4 & 1-\beta_4 & 0 & 0 & 0 & 0 & 0 & 0 \\
\alpha_5\beta_5 & \alpha_5\beta_5 & \alpha_5\beta_5 & \alpha_5\beta_5 & 1-\beta_5 & 0 & 0 & 0 & 0 & 0 \\
\alpha_6\beta_6 & \alpha_6\beta_6 & 2\alpha_6\beta_6 & \alpha_6\beta_6 & \alpha_6\beta_6 & 1-\beta_6 & 0 & 0 & 0 & 0 \\
\alpha_7\beta_7 & \alpha_7\beta_7 & \alpha_7\beta_7 & \alpha_7\beta_7 & \alpha_7\beta_7 & \alpha_7\beta_7 & 1-\beta_7 & 0 & 0 & 0 \\
\alpha_8\beta_8 & \alpha_8\beta_8 & \alpha_8\beta_8 & 2\alpha_8\beta_8 & \alpha_8\beta_8 & \alpha_8\beta_8 & \alpha_8\beta_8 & 1-\beta_8 & 0 & 0 \\
\alpha_9\beta_9 & \alpha_9\beta_9 & \alpha_9\beta_9 & \alpha_9\beta_9 & \alpha_9\beta_9 & \alpha_9\beta_9 & \alpha_9\beta_9 & \alpha_9\beta_9 & 1-\beta_9 & 0 \\
\alpha_{10}\beta_{10} & \alpha_{10}\beta_{10} & \alpha_{10}\beta_{10} & \alpha_{10}\beta_{10} & 2\alpha_{10}\beta_{10} & \alpha_{10}\beta_{10} & \alpha_{10}\beta_{10} & \alpha_{10}\beta_{10} & \alpha_{10}\beta_{10} & 1-\beta_{10}
\end{bmatrix} \tag{2.13}$$

with the values, β_i, being the same as defined above. Assuming each integer breakage is equally probable, the other parameter, α_i, is given by

$$\alpha_i=\begin{cases}\dfrac{2}{i-1}, & i \text{ odd} \\ \dfrac{2}{i}, & i \text{ even}\end{cases} \tag{2.14}$$

ensuring an overall conservation of mass. A third alternative model explored in this paper assumes that particles are more likely to break in half than into unequal sizes, which for the 10×10 case is described by

$$C = \begin{bmatrix} 1 & 0 & 0 & 0 & 0 & 0 & 0 & 0 & 0 & 0 \\ 2\alpha_{2,1}\beta_2 & 1-\beta_2 & 0 & 0 & 0 & 0 & 0 & 0 & 0 & 0 \\ \alpha_{3,1}\beta_3 & \alpha_{3,2}\beta_3 & 1-\beta_3 & 0 & 0 & 0 & 0 & 0 & 0 & 0 \\ \alpha_{4,1}\beta_4 & 2\alpha_{4,2}\beta_4 & \alpha_{4,3}\beta_4 & 1-\beta_4 & 0 & 0 & 0 & 0 & 0 & 0 \\ \alpha_{5,1}\beta_5 & \alpha_{5,2}\beta_5 & \alpha_{5,3}\beta_5 & \alpha_{5,4}\beta_5 & 1-\beta_5 & 0 & 0 & 0 & 0 & 0 \\ \alpha_{6,1}\beta_6 & \alpha_{6,2}\beta_6 & 2\alpha_{6,3}\beta_6 & \alpha_{6,4}\beta_6 & \alpha_{6,5}\beta_6 & 1-\beta_6 & 0 & 0 & 0 & 0 \\ \alpha_{7,1}\beta_7 & \alpha_{7,2}\beta_7 & \alpha_{7,3}\beta_7 & \alpha_{7,4}\beta_7 & \alpha_{7,5}\beta_7 & \alpha_{7,6}\beta_7 & 1-\beta_7 & 0 & 0 & 0 \\ \alpha_{8,1}\beta_8 & \alpha_{8,2}\beta_8 & \alpha_{8,3}\beta_8 & 2\alpha_{8,4}\beta_8 & \alpha_{8,5}\beta_8 & \alpha_{8,6}\beta_8 & \alpha_{8,7}\beta_8 & 1-\beta_8 & 0 & 0 \\ \alpha_{9,1}\beta_9 & \alpha_{9,2}\beta_9 & \alpha_{9,3}\beta_9 & \alpha_{9,4}\beta_9 & \alpha_{9,5}\beta_9 & \alpha_{9,6}\beta_9 & \alpha_{9,7}\beta_9 & \alpha_{9,8}\beta_9 & 1-\beta_9 & 0 \\ \alpha_{10,1}\beta_{10} & \alpha_{10,2}\beta_{10} & \alpha_{10,3}\beta_{10} & \alpha_{10,4}\beta_{10} & 2\alpha_{10,5}\beta_{10} & \alpha_{10,6}\beta_{10} & \alpha_{10,7}\beta_{10} & \alpha_{10,8}\beta_{10} & \alpha_{10,9}\beta_{10} & 1-\beta_{10} \end{bmatrix}$$

(2.15)

which assumes a normal distribution of probability centered at the halfway point. This model includes a third parameter, σ, that is the standard deviation of the normal probability curve defining the values of $\alpha'_{i.j}$.

$$\alpha'_{i,j} = \frac{1}{\sqrt{2\pi\sigma^2}} \exp\left[-\frac{(i-2j)}{4\sigma^2} \right] \tag{2.16}$$

Since the curve is symmetric, in row 10, $\alpha_{10,5}$ is the maximum value and $\alpha_{10,4} = \alpha_{10,6}$, etc. The values of $\alpha'_{i,j}$ are scaled so that $\sum_j j\alpha_{i,j} = i$ for odd i, and $\sum_j j\alpha_{i,j} + j\alpha_{i,j/2} = i$ for even i.

2.4 Parameter Estimation

Each model produces a mass distribution for specified values of the model parameters – $\underline{\theta} = [S_0 \; q]^{\mathrm{T}}$ for the first two models and $\underline{\theta} = [S_0 \; q \; \sigma]^{\mathrm{T}}$ for the third – which were compared to the experimental data by investigating the difference between the cumulative mass distributions for the model, F_{model}, and experimental data, F_{exp}. Under the assumption of additive independent measurement errors, the maximum likelihood and minimum variance parameters based on the

Riemann sum approximation of the integral form for the squared error are the solution of the optimization

$$R' = \min_{\underline{\theta}} \sum_i \sum_j \frac{1}{\sigma_{ij}^2} \left[F_{\text{model}}(t_j, m_i; \underline{\theta}) - F_{\exp}(t_j, m_i) \right]^2 \Delta t_j \Delta m_i \tag{2.17}$$

Assuming the σ_{ij} are all equal, the Δt_j are all equal and setting $\Delta m_i = 1$ weighs the cumulative mass distributions more heavily where more data points have been collected; with E equal to the difference between the model and experimental cumulative distributions, the Equation 2.17 can be simplified to

$$R = \min_{\underline{\theta}} \sum_i \sum_j E_{ij}^2 = \min_{\underline{\theta}} \sum_i \sum_j \left(E^T E \right)_{ij} \tag{2.18}$$

MATLAB is inherently slow when dealing with loops and fast when using matrix-vector arithmetic. Equation 2.18 can be computed in MATLAB as a single function call to the Frobenius norm of the matrix, E, or the elements of E can be stacked as a long vector and the objective computed using the vector 2-norm or vector-vector multiply commands.

Confidence regions for the parameters, $\underline{\theta}$, were estimated using the F distribution (Beck & Arnold, 1977),

$$\frac{S(\underline{\theta}) - R}{R/(n_d - p_\theta)} \approx F_{1-\alpha}(p_\theta, n_d - p_\theta) \tag{2.19}$$

where the sum-of-squared-deviations, $S(\underline{\theta})$, is the objective function of Equation 2.18, n_d is the number of data points, p_θ is the number of parameters, and $1-\alpha$ is the confidence level for the region.

2.5 Results and Discussion

The parameters for the model that assumes equal binary breakage were estimated from the experimental data from 1-minute trials for aspirin in dodecane for 6 different levels of ultrasonic power. The confidence regions around the maximum-likelihood estimates of $S_{0,\mathrm{opt}} = 9.8\times10^{-4}$ and $q_{\mathrm{opt}} = 0.074$ are shown in Figure 2.6. The uncertainties in the efficiency factor, S_0, are $<10\%$ but somewhat larger for the exponent, q, on a relative basis. The positive value for q again indicates that large crystals are more likely to break that small crystals. The cumulative mass distributions of the population balance model for crystal breakage in the presence of ultrasound nearly overlaps the experimental data for applied power between 10 and 40 W, with noticeable deviations for 3 and 5 W (Figure 2.7). The population balance model quantitatively described the changes in the mass distributions due to increased breakage as ultrasonic intensity increased (Figure 2.7).

A second set of experiments measured the effects of ultrasound on the cumulative mass distributions for aspirin in silicone oils of 10 different viscosities (Figure 2.8). As before, the cumulative mass distributions obtained for the best-fit model parameters were in agreement with experimental data. The model quantitatively described the effect of decreased breakage on the mass distributions as the liquid viscosity increases, due to the decreased cavitation (for increased liquid viscosity, more energy would be required to induce cavitation). The confidence regions computed for the best-fit model parameters, $S_{0,\mathrm{opt}} = 8.8\times10^{-3}$ and $q_{\mathrm{opt}} = 5.6\times10^{-6}$, are shown in Figure 2.9. For this set of experiments, the value for the exponent of $q = 0$ falls within the confidence regions indicating that the dependency of the breakage rate on mass was not statistically significant for silicone oils within this range of viscosities.

For the uniform binary breakage model (Equation 2.13), the best-fit model parameters were $S_{0,\text{opt}} = 8.3\times10^{-6}$ and $q_{\text{opt}} = 1.1$ for the experiments with varying ultrasonic power and $S_{0,\text{opt}} = 2.6\times10^{-8}$ and $q_{\text{opt}} = 2.0$ for the experiments with varying liquid viscosity. The corresponding confidence regions for the model parameters are shown in Figures 2.10-2.11. An interesting observation from Figures 2.10-2.11 for the uniform binary breakage model is that the best fit exponent, q_{opt}, has nominal values that are very close to integers with very small confidence intervals. The actual fits to the experimental cumulative mass distributions in Figures 2.12-2.13, however, are not as good as for the equal binary breakage model.

The reduction in fitting capability observed in the uniform breakage model motivated the third breakage model (Equation 2.15) that includes an additional parameter, which is a standard deviation. In comparison to the 2-parameter models, a high value for the standard deviation approximates the uniform breakage model, while a standard deviation approaching zero is asymptotic to the equal breakage model. The best-fit model parameters were $S_{0,\text{opt}} = 7.1\times10^{-4}$, $q_{\text{opt}} = 0.16$, and $\sigma_{\text{opt}} = 32$ for the experiments with varying ultrasonic power and $S_{0,\text{opt}} = 8.8\times10^{-4}$, $q_{\text{opt}} = 1.3\times10^{-13}$, and $\sigma_{\text{opt}} = 0.12$ for the experiments with varying liquid viscosity. Noting that for a system of size 3068 elements, the optimal standard deviations reported here are small, indicating that the 3-parameter model agrees with earlier analysis, that the system favors the equal breakage model. Confidence regions for the 3-parameter model (Equation 2.15) are shown in Figures 2.14-2.15 as projections onto 2D planes for power and viscosity, respectively, The 3-parameter binary weighted breakage model provides a better fit to the experimental data, but not necessarily good enough to suggest that the model describes the underlying phenomena better than the 2-parameter breakage models (Figures 2.16-2.17). The

relative uncertainties in q and σ are large for the experiments with varying viscosity (Figure 2.15).

2.6 Conclusions

Population balance models for the breakage of crystals due to ultrasonication are presented that relate breakage rate proportionally to ultrasonic intensity and exponentially to fluid viscosity for crystals dispersed in dodecane and silicone oils. Estimating kinetic parameters in breakage rates by comparing the crystal size distributions of the models with experimental data provided more support for binary breakage events, where the crystals break in half, than breakage events that produce uniformly distributed particle sizes. The best fit was a result of the optimization of a 3-parameter model with normally weighted breakage events with respect to particle size, but the less complex, 2-parameter equal breakage model provided a similar fit while requiring less computational time.

At the time of its creation, this paper described the most advanced model yet developed for describing ultrasound-induced breakage of crystals. Such models can be used to aid in understanding ultrasonic breakage mechanisms or in selecting ultrasonic conditions that best move a crystal size distribution toward a target distribution. Additional work would be useful for validating the simulation model by repeating the experiments with data outside of that used to optimize the parameters.

2.7 Figures

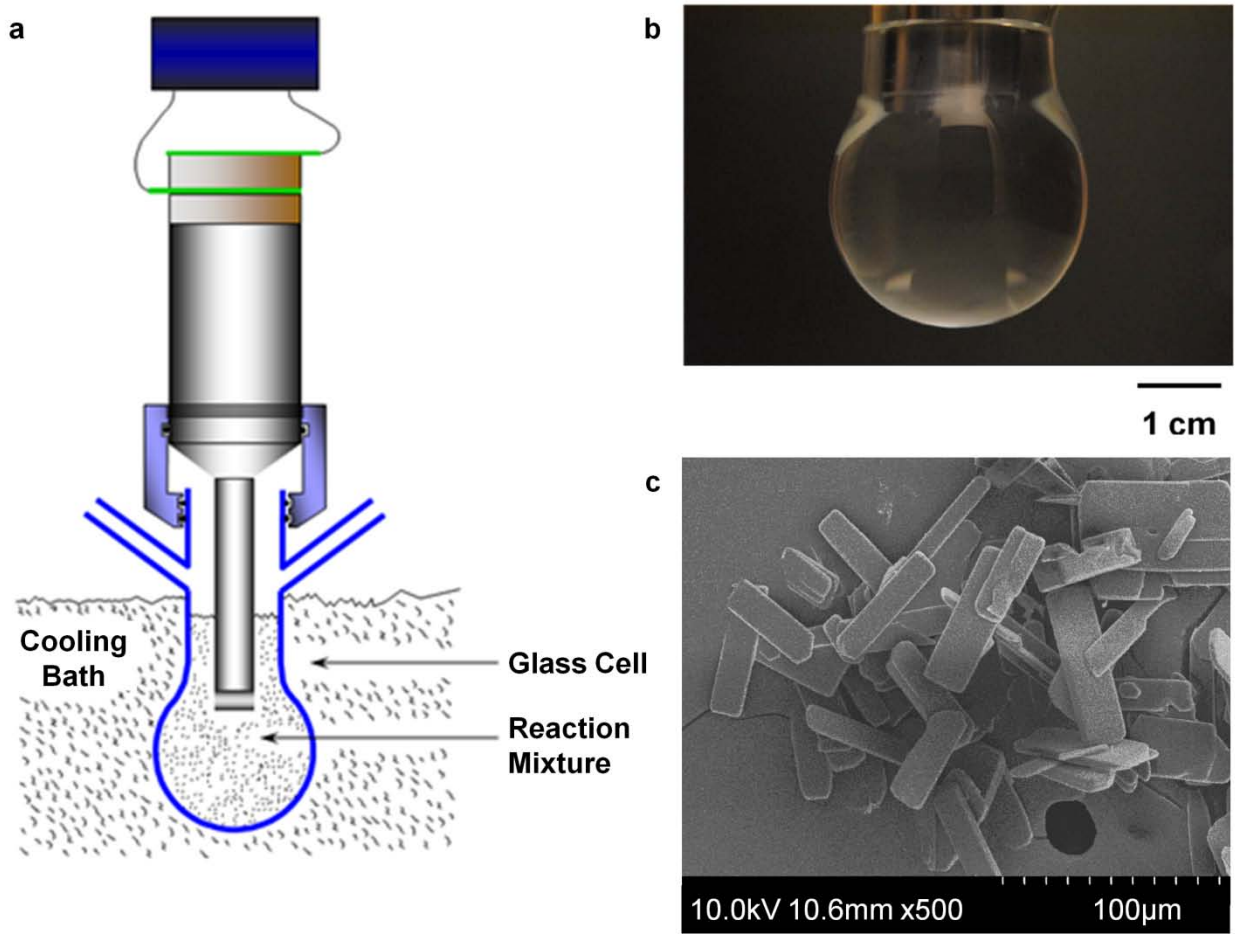

Figure 2.1: (a) Schematic of experimental setup for sonofragmentation experiments, with the 20 kHz ultrasonic horn shown in the middle with power supply at the top. (b) Photograph of glass cell within which fragmentation was induced. (c) SEM image of aspirin crystals synthesized in dodecane.

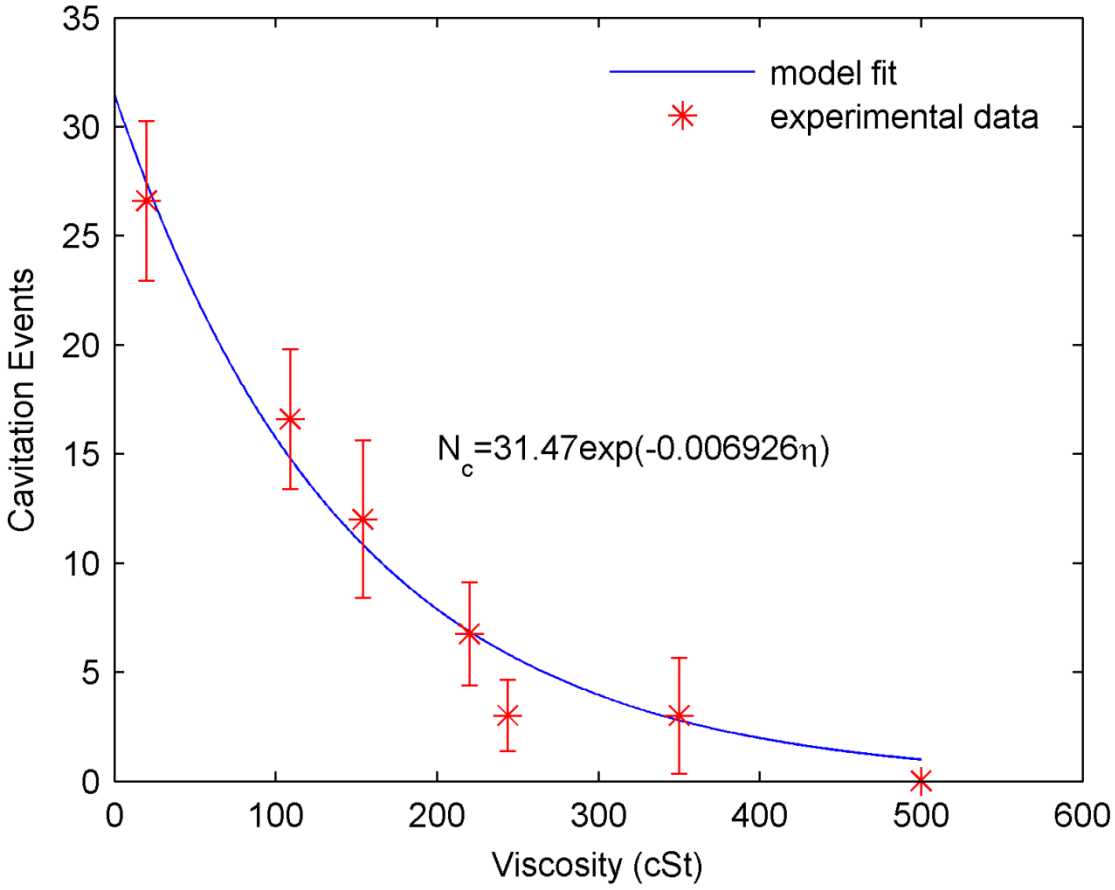

Figure 2.2: An exponential relationship was observed between the number of cavitation events and the liquid viscosity subject to ultrasound, with a detailed description of the laboratory system and experimental procedures to measure cavitation events available elsewhere (Lifshitz, et al., 1997).

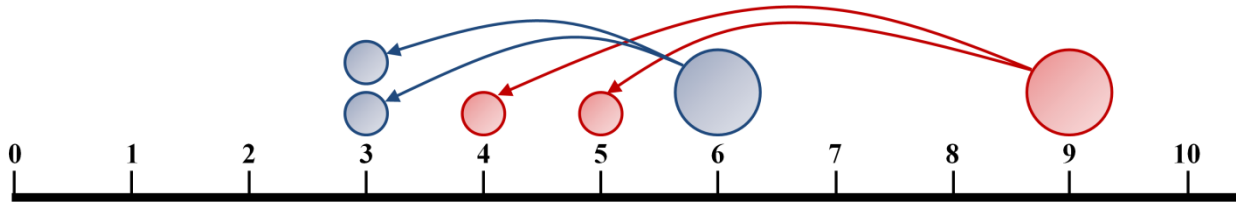

Figure 2.3: An equal binary breakage model with crystal masses restricted to integer values. Each integer, z, represents a bin of particles with mass equal to $zm'_{\min}$, where $m'_{\min}$ is the minimum particle mass ($m'_{\min} = 6.93\,\text{pg}$) calculated from SEM images of the unbroken particles, described by Figure 2.4. The maximum integer, $z_{\max} = 3853$, corresponds to the maximum particle size, $m'_{\max} = 26.7\,\text{ng}$.

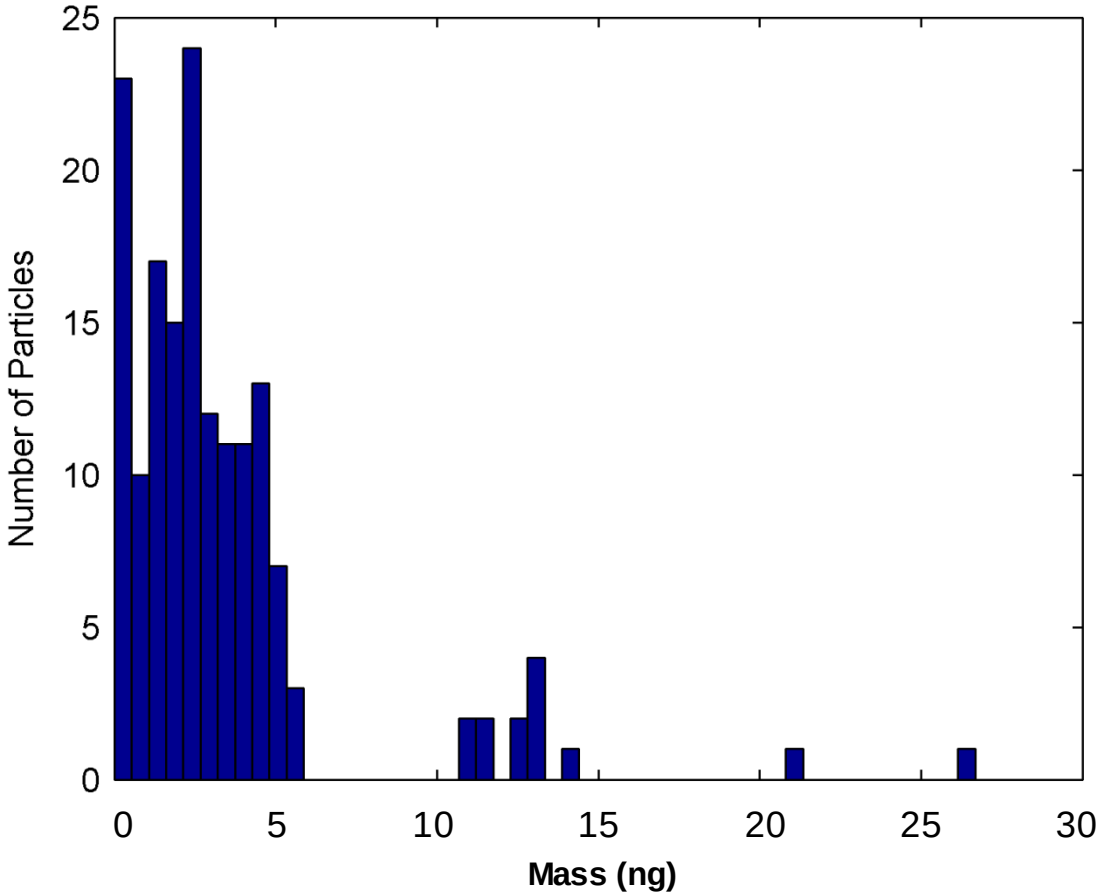

Figure 2.4: Histogram of crystal masses prior to sonication (159 representative particles shown). The difficulty in accurately approximating a curve to the number distribution motivated the use of the cumulative size distribution in Figure 2.5 for the initial condition of the population balance equation (Equation 2.4).

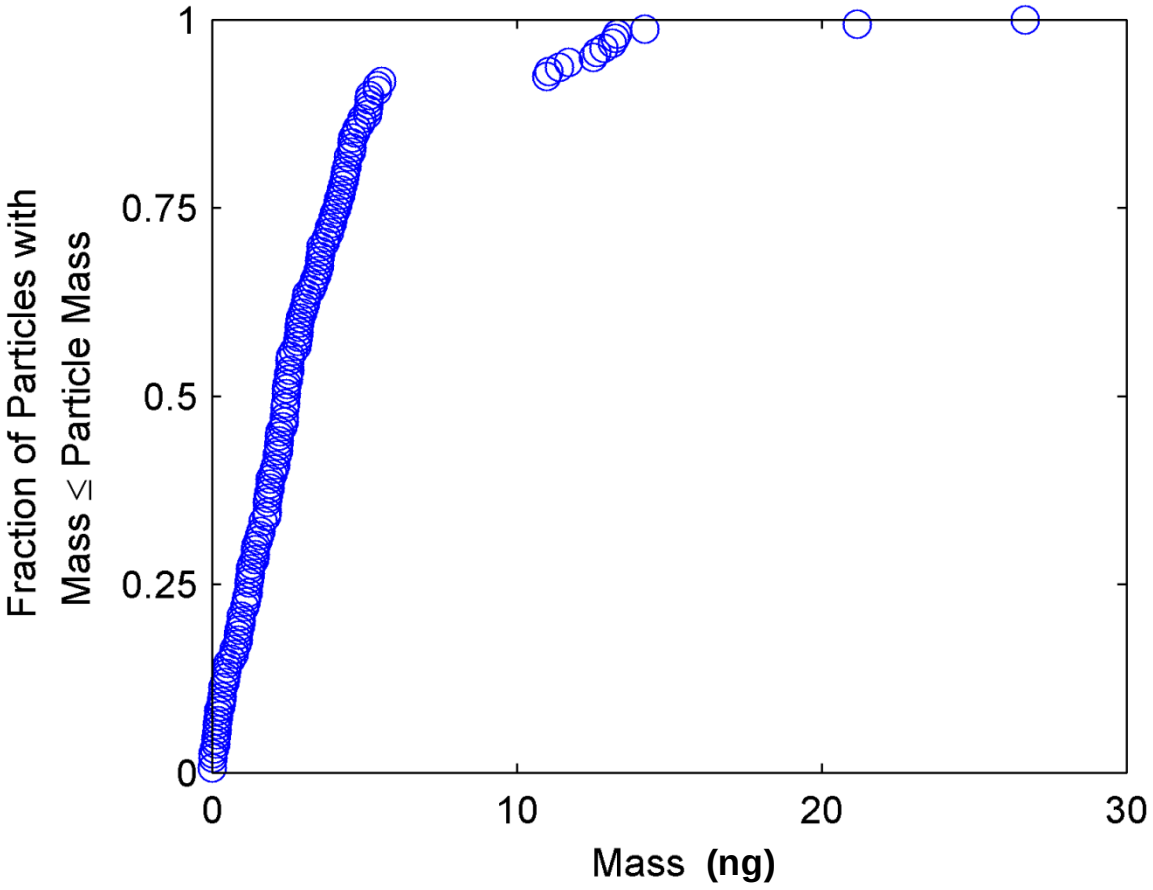

Figure 2.5: The cumulative mass distribution of unbroken particles provides improved characteristics for computation; the cumulative distribution is less sensitive to the subset of representative particles and more accurately represents the full, underlying population.

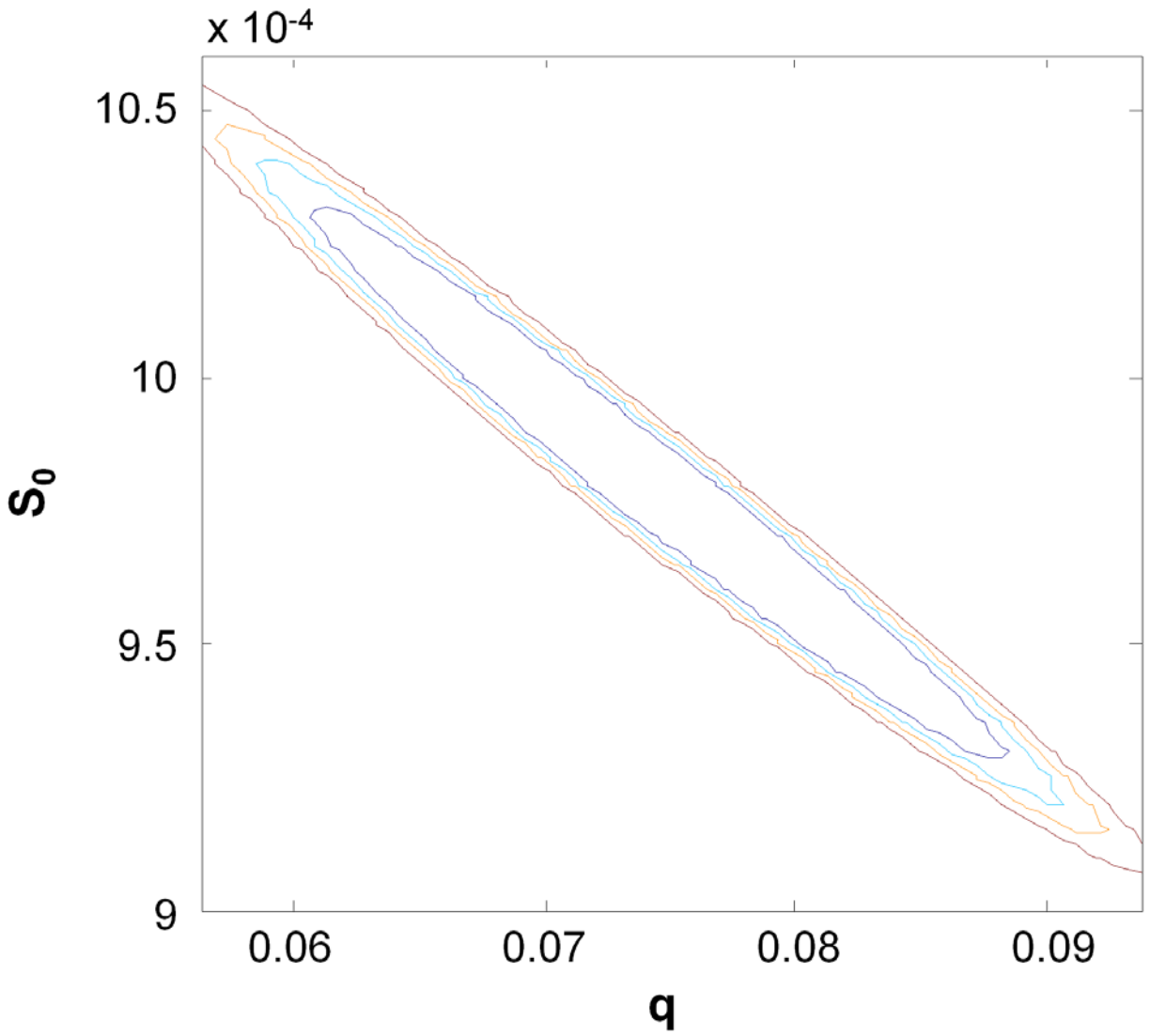

Figure 2.6: Confidence regions for the parameters in the equal binary breakage model (Equation 2.7) at 90%, 95%, 97.5%, and 99% (from inside to outside) confidence levels for experimental data collected after 1 minute at varying ultrasonic power (3, 5, 10, 20, 30, & 40 W) in the solvent dodecane (viscosity = 1.8 cSt).

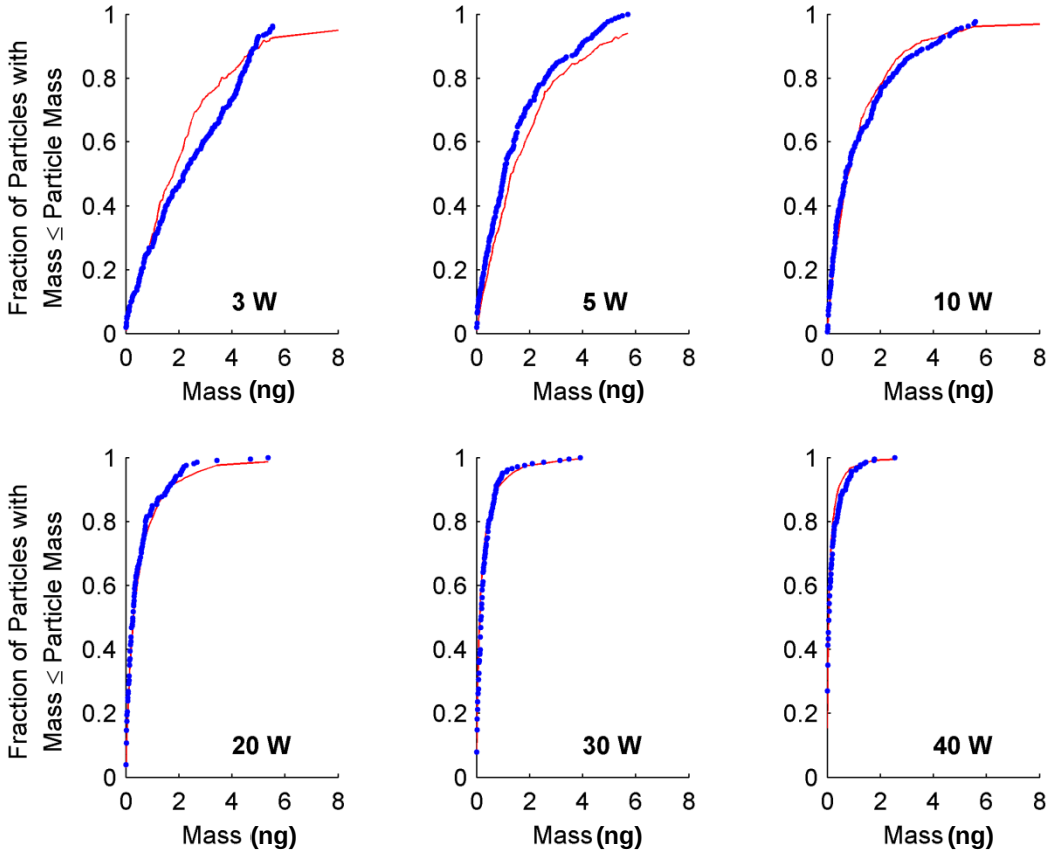

Figure 2.7: Cumulative mass distributions for the equal binary breakage model (Equation 2.7) with best-fit model parameters, $\underline{\theta}$, (—) and experiments (•) for variations in the ultrasonic power in the solvent dodecane (viscosity = 1.8 cSt).

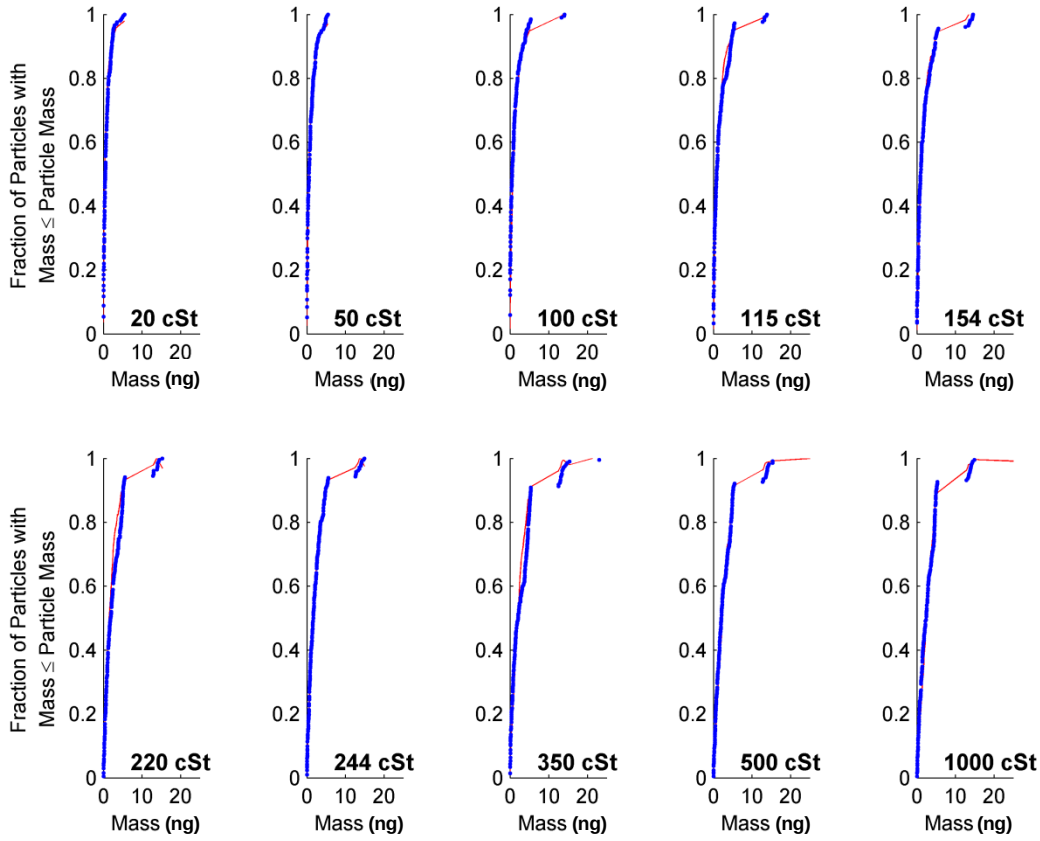

Figure 2.8: Cumulative mass distributions for the equal binary breakage model (Equation 2.7) with best-fit model parameters, $\underline{\theta}$, (—) and experiments (•) for variations in the liquid viscosity at an applied ultrasound power of 30W.

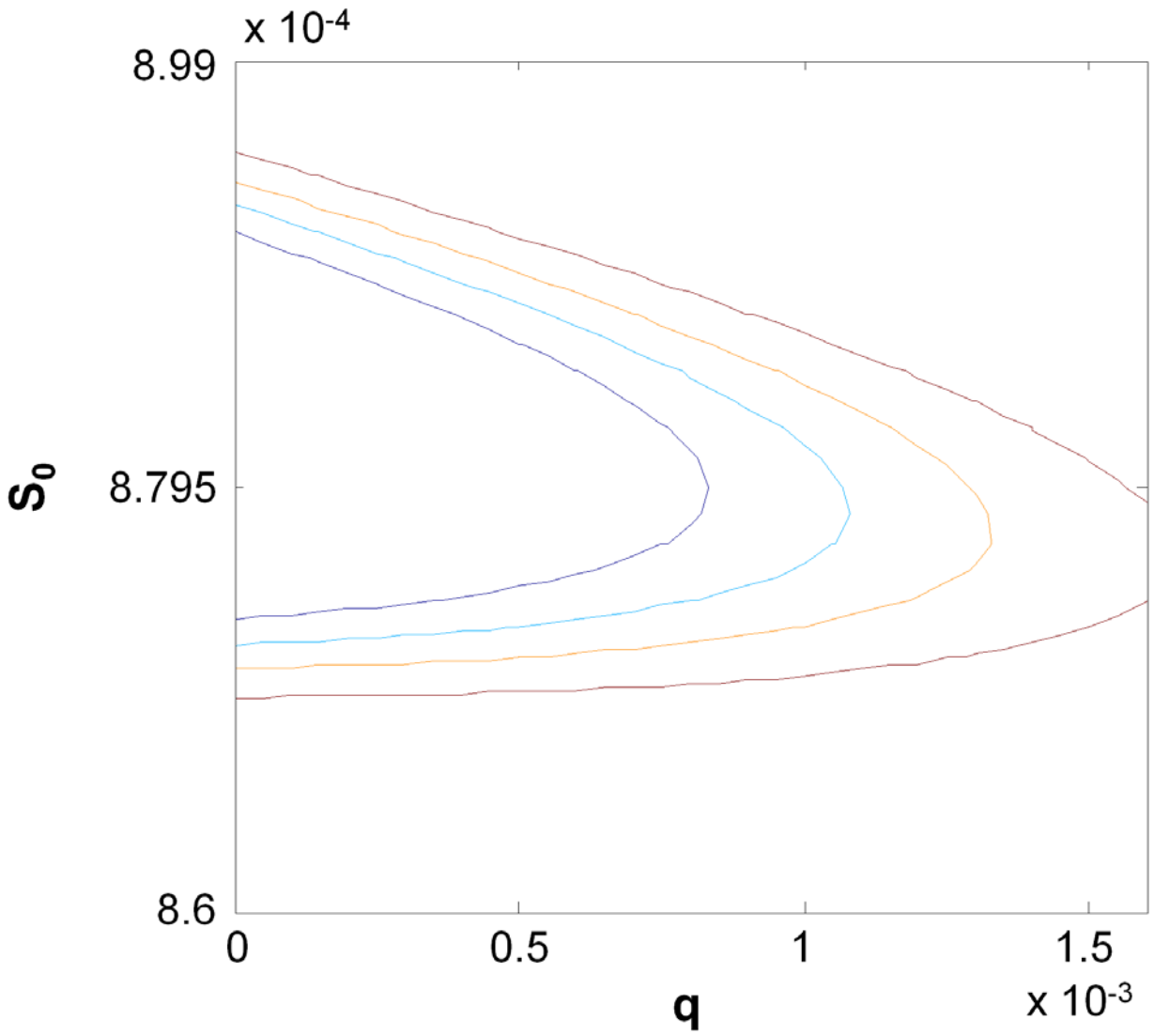

Figure 2.9: Confidence regions for the parameters in the equal binary breakage model (Equation 2.7) at 90%, 95%, 97.5%, and 99% (from inside to outside) confidence levels for experimental data collected after 1 minute at 30W ultrasound intensity at varying liquid viscosity (20, 50, 100, 115, 154, 220, 244, 350, 500, & 1000 cSt).

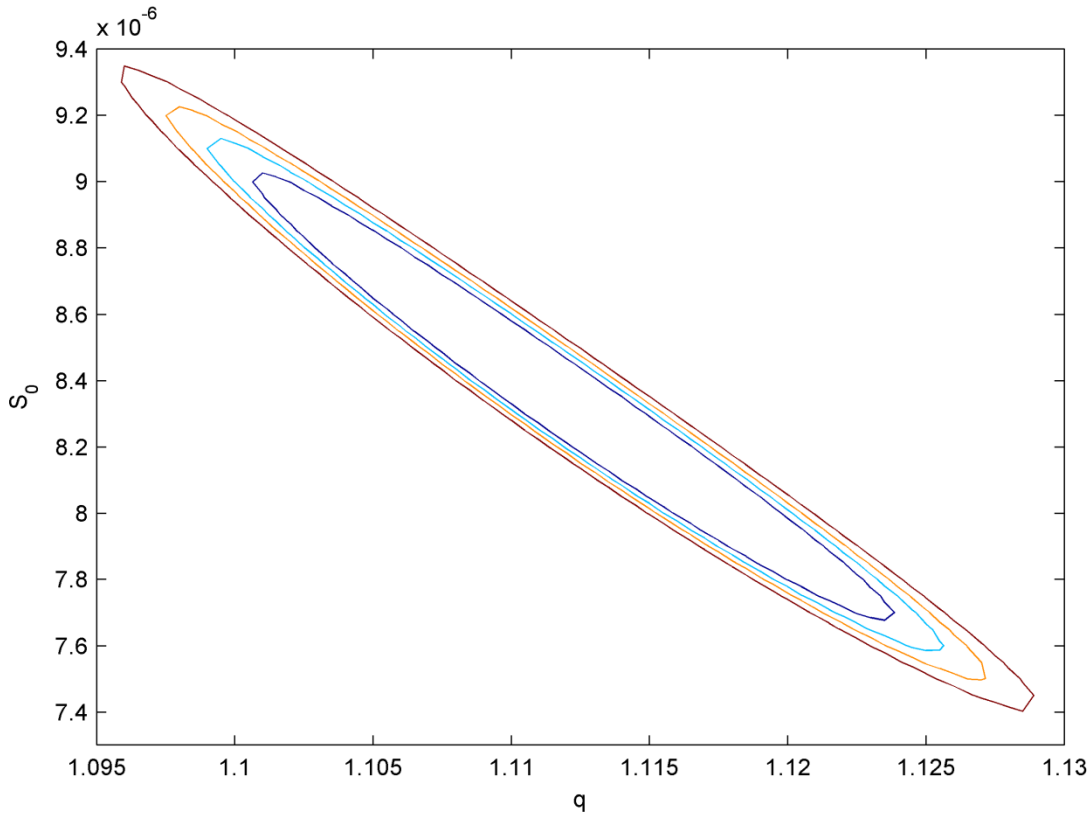

Figure 2.10: Confidence regions for the parameters in the uniform binary breakage model (Equation 2.13) at 90%, 95%, 97.5%, and 99% (from inside to outside) confidence levels for experimental data collected after 1 minute at varying ultrasonic power (3, 5, 10, 20, 30, & 40 W) in the solvent dodecane (viscosity = 1.8 cSt).

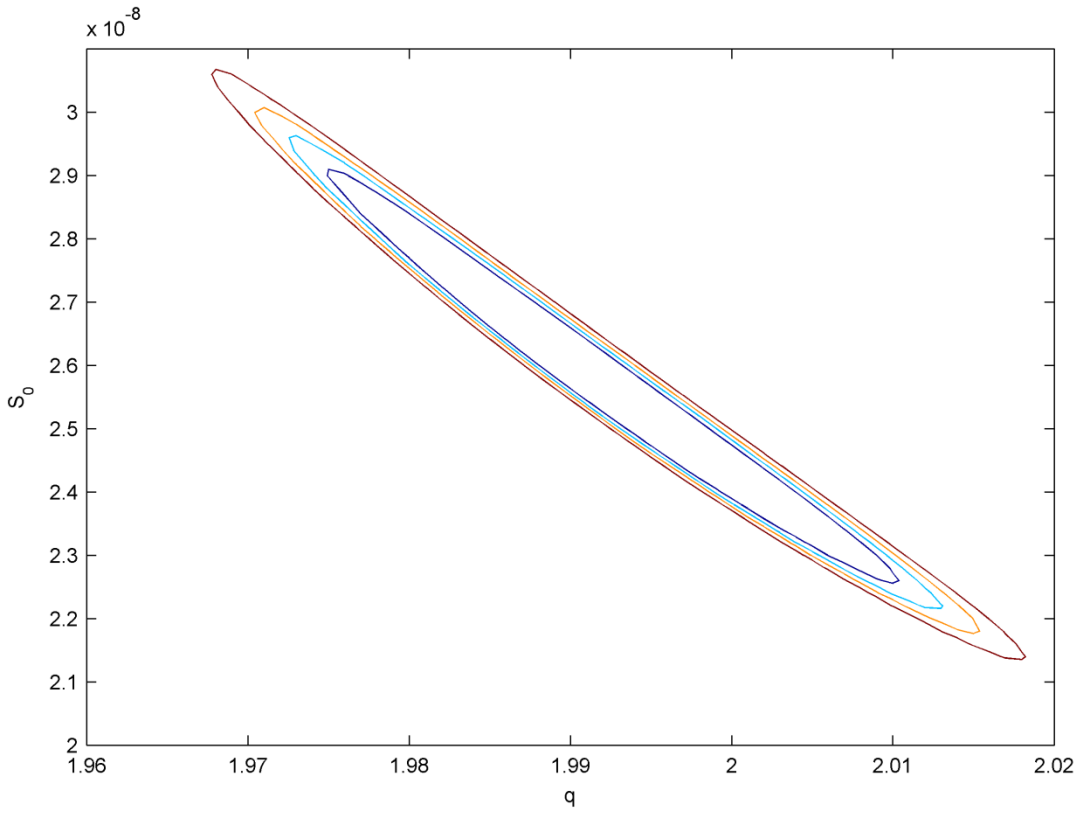

Figure 2.11: Confidence regions for the parameters in the uniform binary breakage model (Equation 2.13) at 90%, 95%, 97.5%, and 99% (from inside to outside) confidence levels for experimental data collected after 1 minute at 30W ultrasound intensity at varying liquid viscosity (20, 50, 100, 115, 154, 220, 244, 350, 500, & 1000 cSt).

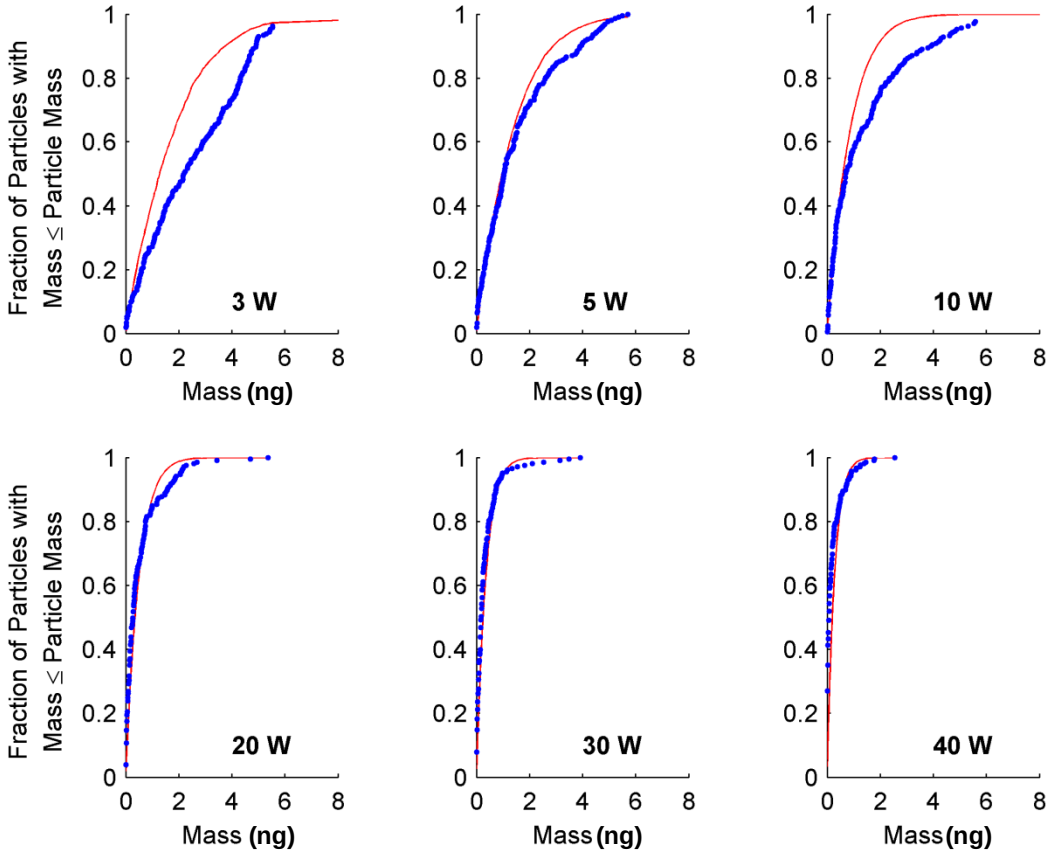

Figure 2.12: Cumulative mass distributions for the uniform binary breakage model (Equation 2.13) with best-fit model parameters, $\underline{\theta}$, (—) and experiments (•) for variations in the ultrasonic power in the solvent dodecane (viscosity = 1.8 cSt).

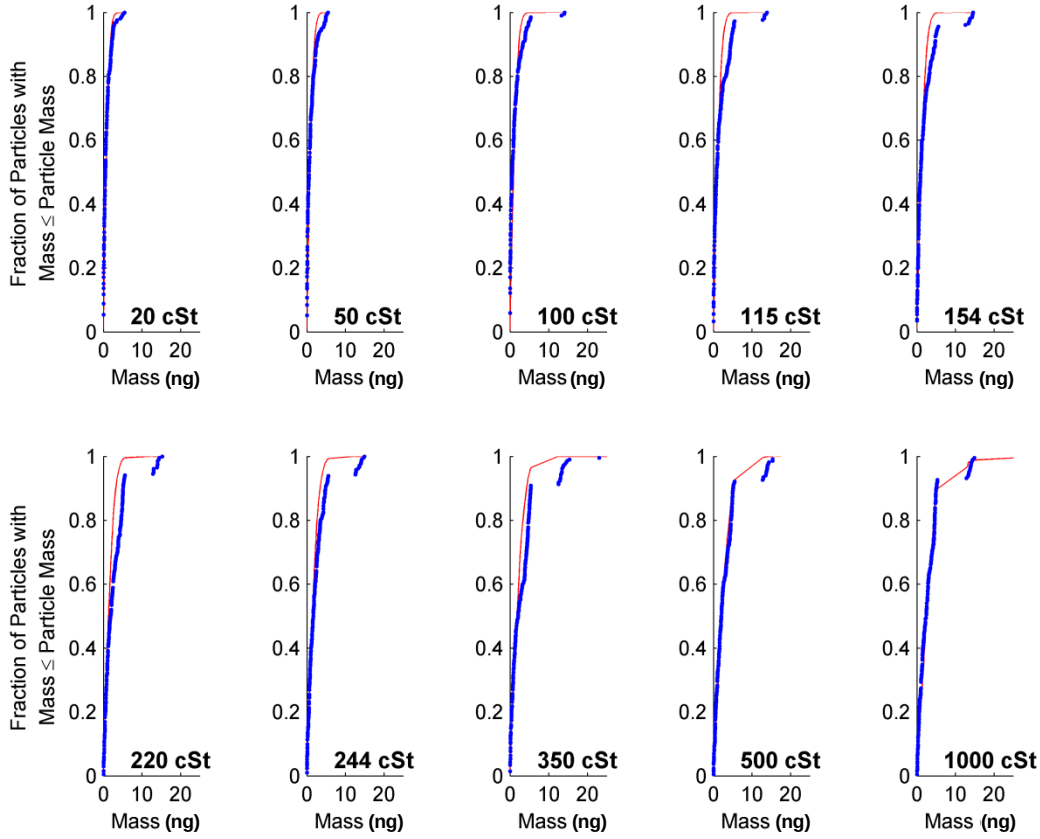

Figure 2.13: Cumulative mass distributions for the uniform binary breakage model (Equation 2.13) with best-fit model parameters, $\underline{\theta}$, (—) and experiments (•) for variations in the liquid viscosity at an applied ultrasound power of 30W.

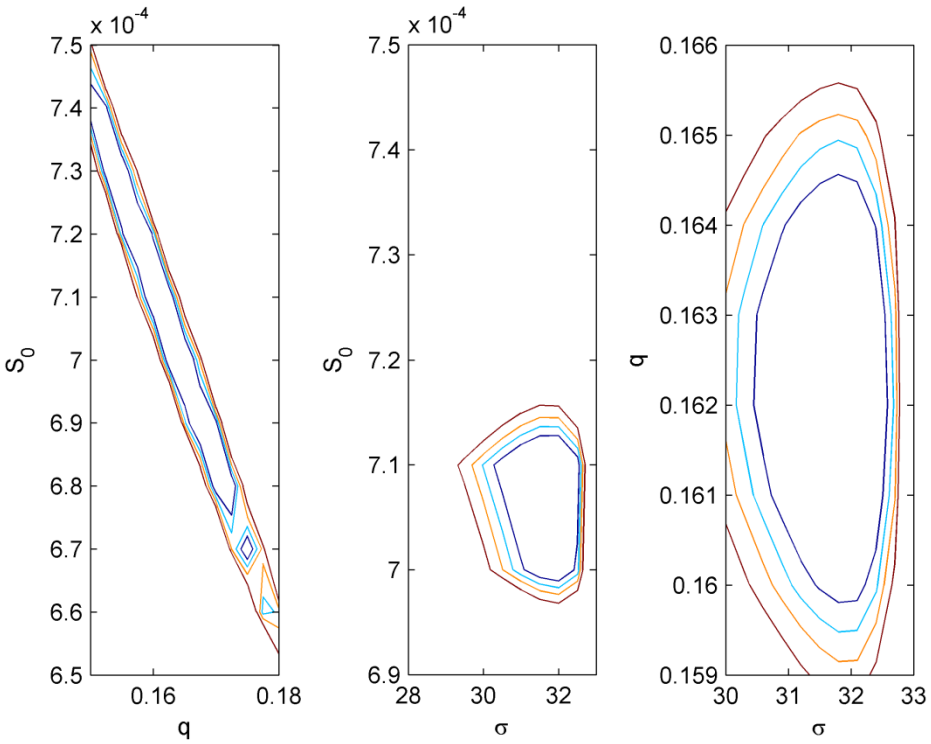

Figure 2.14: Confidence region 2-D projections for the parameters in the weighted binary breakage model (Equation 2.15) at 90%, 95%, 97.5%, and 99% (from inside to outside) confidence levels for experimental data collected after 1 minute at varying ultrasonic power (3, 5, 10, 20, 30, & 40 W) in the solvent dodecane (viscosity = 1.8 cSt). In each case, the excluded parameter is assumed to be at its nominal value.

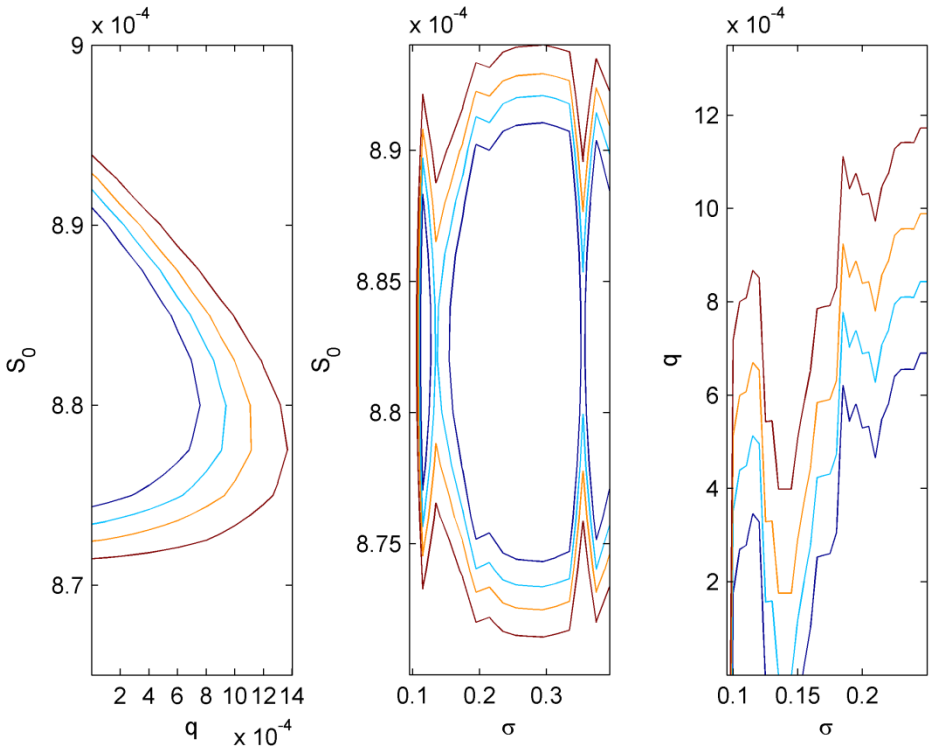

Figure 2.15: Confidence region 2-D projections for the parameters in the weighted binary breakage model (Equation 2.15) at 90%, 95%, 97.5%, and 99% (from inside to outside) confidence levels for experimental data collected after 1 minute at 30 W ultrasound intensity at varying liquid viscosity (20, 50, 100, 115, 154, 220, 244, 350, 500, & 1000 cSt). In each case, the excluded parameter is assumed to be at its nominal value.

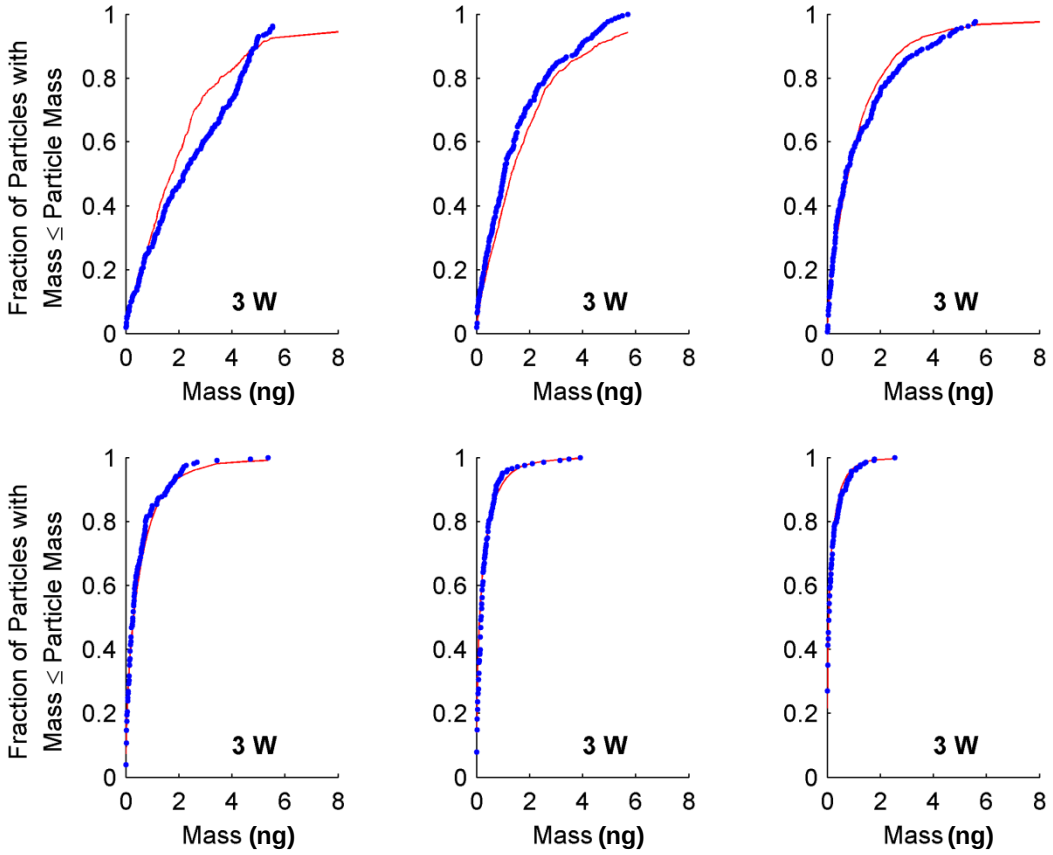

Figure 2.16: Cumulative mass distributions for the weighted binary breakage model (Equation 2.15) with best-fit model parameters, $\underline{\theta}$, (—) and experiments (•) for variations in the ultrasonic power in the solvent dodecane (viscosity = 1.8 cSt).

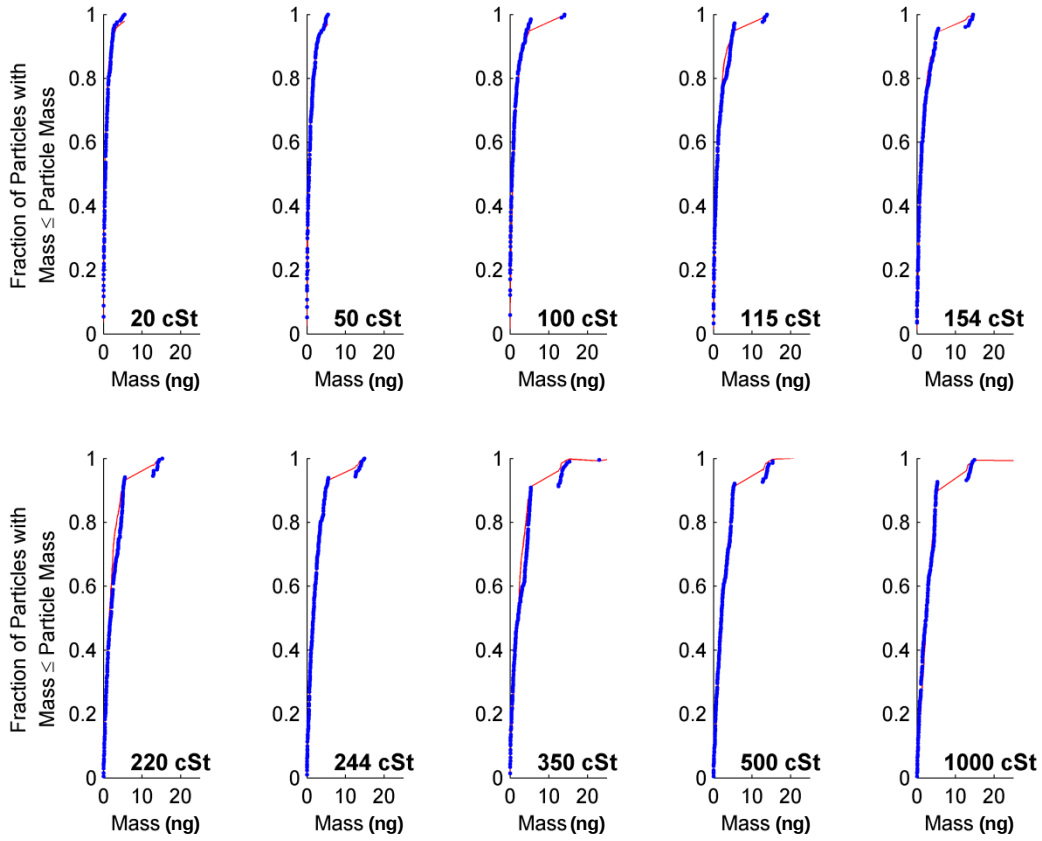

Figure 2.17: Cumulative mass distributions for the weighted binary breakage model (Equation 2.15) with best-fit model parameters, $\underline{\theta}$, (—) and experiments (•) for variations in the liquid viscosity at an applied ultrasound power of 30W.

CHAPTER 3

PARAMETER ESTIMATION OF CRYSTALLIZATION KINETICS FROM PARALLEL BATCH DESUPERSATURATION EXPERIMENTS

3.1 Introduction

Antisolvent crystallization is a semi-batch process used in the pharmaceutical industry to purify a compound, in which an antisolvent is added to a saturated solution to change the chemistry by decreasing the solubility of the active compound (Myerson, 2002). Antisolvent crystallization is preferred over simply cooling when the active compound is thermally sensitive. The state of supersaturation created in this manner promotes crystallization of the solute. The rate of crystal formation and growth and the evolution of the distribution of crystal sizes have been studied extensively in the literature (e.g. Hulburt & Katz, 1964; Randolph & Larson, 1988; Chung et al., 2000; Gunawan et al., 2004; Jiang et al., 2012) since growth and nucleation kinetics can be used to create predictive models to design and control future experiments (e.g. Nagy et al., 2008; Woo et al., 2009). Crystal size distribution data, however, is expensive to measure *in situ*, and in experimental systems where aggregation is present, accurate measurements are difficult to obtain. In this case experiments were conducted under the hypothesis that with enough data, under a variety of conditions (e.g., with respect to seed load, antisolvent addition rate, etc.), the solution concentration alone could be used to obtain accurate nucleation and growth parameters for a seeded, antisolvent crystallization where aggregation was expected, contrary to theory presented in the literature (Miller & Rawlings, 1994).

3.2 Model Equations

The desaturation of a seeded solution in a semi-batch system due to crystal growth induced by antisolvent addition can be modeled by a population balance equation and a solute balance (Hulburt & Katz, 1964; Randolph & Larson, 1988). The population balance equation for a semi-batch crystallization is

$$\frac{\partial f(L,t)}{\partial t} + \frac{\partial \big(G(L,t) f(L,t)\big)}{\partial L} = h\big(f(L,t), L, t\big), \tag{3.1}$$

where f is the particle size distribution, L is a characteristic length of a crystal, t is time, and G and h are the crystal growth and nucleation rates given by

$$G = k_g \left(\frac{C - C_{sat}}{C_{sat}} \right)^g, \tag{3.2}$$

$$h = \begin{cases} k_b \left(\dfrac{C - C_{sat}}{C_{sat}} \right)^b \mu_3 \left(-\dfrac{4}{L_0^2} \left(L - \dfrac{L_0}{2} \right)^2 + 1 \right), & 0 \le L \le L_0 \\ 0, & \text{otherwise} \end{cases}, \tag{3.3}$$

where L_0 is the maximum size of nucleated crystals, the prefactors k_g and k_b and the exponents g and b are model parameters, C is the solute concentration, C_{sat} is the solubility in units of gram solute per gram solvents, and μ_3 is the third-order moment of the crystal size distribution (Equation 3.1) where the *i*th-order moment is defined by

$$\mu_i = \int_0^\infty f(L,t) L^i dL\,. \tag{3.4}$$

The last factor in Equation 3.3 speficies the size distribution of the crystal nuclei.

The solute balance for a semibatch crystallization can be written in the form of an analytical equation,

$$C_0 + \rho_c k_v \mu_{3,0} = C(t)\frac{x_{A,0}}{x_A(t)} + \rho_c k_v \mu_3(t) \tag{3.5}$$

where x_A is the mass fraction of the solvent A in the solvent/antisolvent mixture, k_v is the volumetric shape factor, C_0 is the initial concentration, and ρ_c is the crystal density.

3.3 Simulation Method

The solution to Equation 3.1 was obtained using the method of characteristics (McOwen, 2003), which involves the numerical solution of two ordinary differential equations (ODEs) for each characteristic,

$$\frac{dL}{dt} = G(L,t), \tag{3.6}$$

$$\frac{df(L,t)}{dt} = -f(L,t)\frac{\partial G(L,t)}{\partial L} + B(f(L,t),L,t), \tag{3.7}$$

where the initial conditions for each characteristic are

$$L(t=0) = L_0, \tag{3.8}$$

$$f(L,t=0) = f_0(L). \tag{3.9}$$

The number of characteristics, N, is dictated by the desired resolution of the crystal size distribution, f, The total number of equations to solve is $2N$ ODEs (Equations 3.6-3.7 for each characteristic) and 1 algebraic equation (Equation 3.5). The system of equations can be written in the form of a system of differential-algebraic equations (DAEs) that is index 1:

$$M\frac{dY(t)}{dt} = b(Y,t), \tag{3.10}$$

where

$$Y = \begin{bmatrix} L_1(t) \\ \vdots \\ L_N(t) \\ f_1(t) \\ \vdots \\ f_N(t) \\ C(t) \end{bmatrix}, \tag{3.11}$$

$$M = \begin{bmatrix} I_{2N} & 0 \\ 0 & 0 \end{bmatrix}, \tag{3.12}$$

$$b = \begin{bmatrix} G(L_1,t) \\ \vdots \\ G(L_N,t) \\ -f_1 \dfrac{\partial G(L_1,t)}{\partial L} + B(f_1,L_1,t) \\ \vdots \\ -f_N \dfrac{\partial G(L_N,t)}{\partial L} + B(f_N,L_N,t) \\ \left(C_0 + \alpha\rho_c k_v \mu_{3,0}\right) - \left(C(t)\dfrac{x_{A,0}}{x_A(t)} + \alpha\rho_c k_v \mu_3(t)\right) \end{bmatrix}, \tag{3.13}$$

and the third order moment is approximated by

$$\mu_3(t) \approx \sum_{i=1}^{N} f_i L_i^3 \Delta L_i \,. \tag{3.14}$$

Alternative methods for solving population balance models are reviewed by Gunawan et al., (2008), including the method of moments which can be applied for the growth rate in Equation 3.2, but the presented method of characteristics approach is also applicable to general size-dependent growth kinetics.

3.4 Parameter Estimation Procedure

The model parameters are estimated by solving the constrained equation

$$S(\theta) = \min_{\theta \in \Omega} \sum_{j=1}^{N_e} \sum_{i=1}^{N_{t,j}} \left(C_{\text{sim},j}(\theta, t_i) - C_{\text{exp},j}(t_i) \right)^2, \tag{3.15}$$

where N_e is the number of semibatch experiments with index, j, and $N_{i,j}$ is the number of measurements of the solute concentration collected during semibatch experiment, j. For a system with negligible nucleation rates, the vector of model parameters, $\theta = [\ln k_g, g]^{\mathrm{T}}$, has lower and upper bounds on its elements of

$$\begin{matrix} -5 \le \ln k_g \le 1 \\ 1 \le g \le 2 \end{matrix}. \tag{3.16}$$

The bounds on the growth exponent, g, are determined by Burton-Cabrera-Frank theory (1951). There are no fundamental physical limits on the growth prefactor, k_g, so the bounds are chosen to span a large range.

If nucleation is included, then the vector of model parameters, $\theta = [\ln k_g, g, \ln k_b, b]^{\mathrm{T}}$, is constrained by

$$\begin{matrix} -5 \le \ln k_g \le 1 \\ 1 \le g \le 2 \\ -10 \le \ln k_b \le 10 \\ 1 \le b \le 3 \end{matrix}. \tag{3.17}$$

The optimization (Equation 3.15) was solved using the revised Nelder-Mead simplex algorithm, fminsearchbnd.m (Nelder & Mead, 1965; D'Errico, 2006) in MATLAB version 7.11.0.584. Confidence regions for the parameters, , were estimated using the F distribution (Beck & Arnold, 1977).

$$\frac{S(\theta) - R}{R/(n-p)} \approx F_{1-\alpha}(p, n-p), \tag{3.18}$$

where R is the objective function of the minimization (Equation 3.15) evaluated at the minimizing θ, n is the number of data points, p is the length of the vector θ, and $(1-\alpha)\times 100\%$ is the confidence level for the region.

3.5 Model Structure Evaluation

The ability of the model structure Equations 3.1-3.7 with the nucleation rate set to zero to describe the experimental data was evaluated by applying parameter estimation (Equations 3.15-3.16) for the complete set of eleven "control" desupersaturation experiments, which obtained a minimum value for the objective (Equation 3.15) of 0.0511. The mathematical model is able to fit the data assuming that the only crystallization kinetics is associated with growth, as seen in the comparisons of experimental and model solute concentrations in Figure 3.1.

The optimal value for the growth exponent, g, occurred at its upper bound in this and in all later parameter estimation calculations, so confidence intervals are reported in Table 3.1 only for $\ln k_g$. At the 99% confidence level, the uncertainty is less than $\pm 6\%$. When nucleation is included in the model, subject to the constraints in Equation 3.17, the parameters that optimize Equation 3.15 are $\ln k_g = -0.330$, $g = 2$, $\ln k_b = -7.70$, and $b = 2.90$. The best-fit growth parameters are nearly the same when nucleation kinetics are included, and the value for k_b is so small that the desaturation curves are indistinguishable from Figure 3.1. The value of the objective function in Equation 3.15 when nucleation is included and not included is the same to three significant figures, so the nucleation kinetics are not included in the further analysis.

3.6 Model Validation

To evaluate the prediction capabilities of the model and quantify prediction error, the model parameters were fit using five datasets from the "control" experiments and the parameter space given by Equation 3.15. The resulting optimal growth parameters, θ_{opt5}, were then applied to the simulation of the remaining six "control" experiments with the prediction error calculated by

$$v_{opt}\left(\theta_{opt5}\right) = \sum_{j=1}^{6}\sum_{i=1}^{N_{t,j}}\left(C_{\mathrm{sim},j}(\theta_{opt5}, t_i) - C_{\mathrm{exp},j}(t_i)\right)^2 . \tag{3.19}$$

The standard deviation, σ, of the solute concentration for this optimum set of growth parameters is

$$\sigma = \sqrt{\frac{v_{\mathrm{opt}}}{n-p}}, \tag{3.20}$$

where the number of parameters, $p = 2$, and

$$n = \sum_{j=1}^{6} N_{t,j} . \tag{3.21}$$

The parameter estimation was repeated for all $11!/\left(5!6!\right) = 462$ possible combinations of five datasets and used to construct the histogram in Figure 3.2 of the standard deviations (Equation 3.20) for the remaining six experiments for each parameter vector. The solute concentration predictions are mostly within ± 0.007 g/g of the experimental values.

3.7 Conclusions

A parameter estimation example has been presented whereby crystallization growth and nucleation kinetics parameters were fitted using only desupersaturation data from a large set of

parallel, semi-batch, industrial experiments with uncontrolled agglomeration. The method of characteristics was used in this particular simulation, but the results would not be exclusive to this method, since the full size distribution is not necessary to track the simulated concentration. When the growth exponent is restricted to physical values, the log of the growth prefactor is calculated to be within 6% of its optimal value with 99% confidence. The value of the growth kinetics parameters are virtually unaffected by inclusion/exclusion of nucleation in the model. The model was shown to predict concentration profiles for datasets excluded from the optimization within 0.007 g/g of the experimental values.

3.8 Supplementary Information

For completeness, the bound on the growth exponent, g, was relaxed

$$1 \le g \le 5 \tag{3.22}$$

to determine the mathematical (aphysical) optimum, which was 0.0342. Although this parameter estimation objective is lower by about a factor of two, both models have reasonable agreement with the experimental data (Figures 3.1 and 3.3). The confidence regions for the growth parameters for the aphysical value of g are about 3% for g and 8% for $\ln k_g$ (Figure 3.4). These parameter estimates were not used in the above analysis, since the value for the growth exponent, g, is aphysical.

3.9 Figures

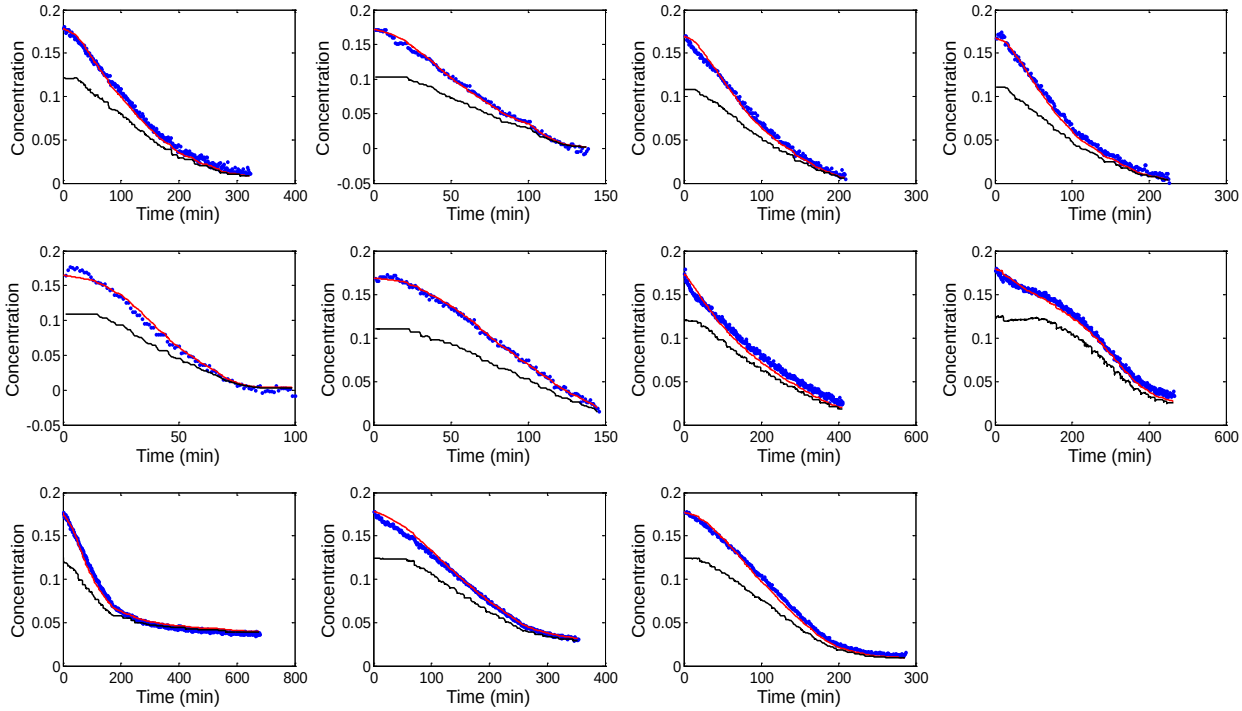

Figure 3.1 Desupersaturation curves for the eleven control experiments at the calculated optimum (Equations 3.15-3.16) for growth only, with $k_g = -0.330$ and $g = 2.00$. The lower black curve (—) is the solubility, the red curve (—) is the solution concentration from the model, and the blue dot (•) marks the experimental solute concentration measurements.

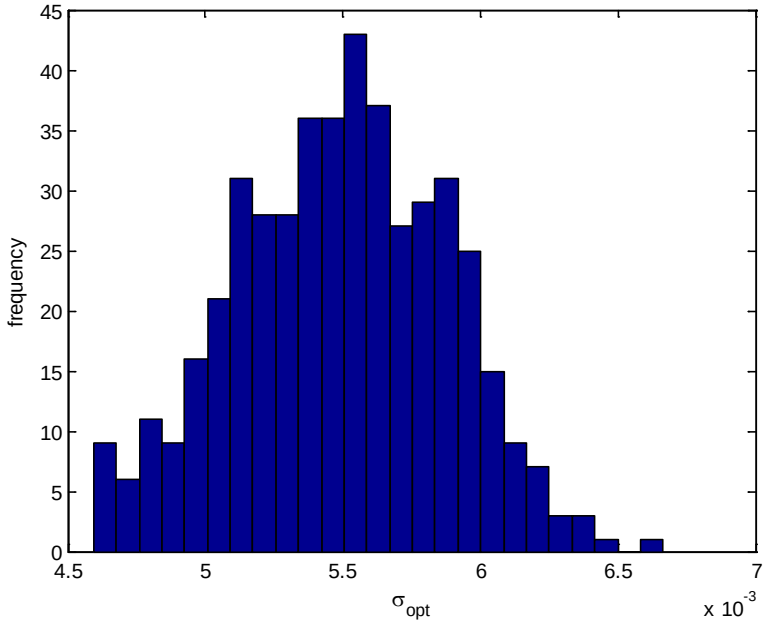

Figure 3.2: Histogram of standard deviations (Equation 3.20) of the solute concentration based on the prediction error v_{opt} in Equation 3.19. The standard deviation is less than 0.007 g/g in every scenario.

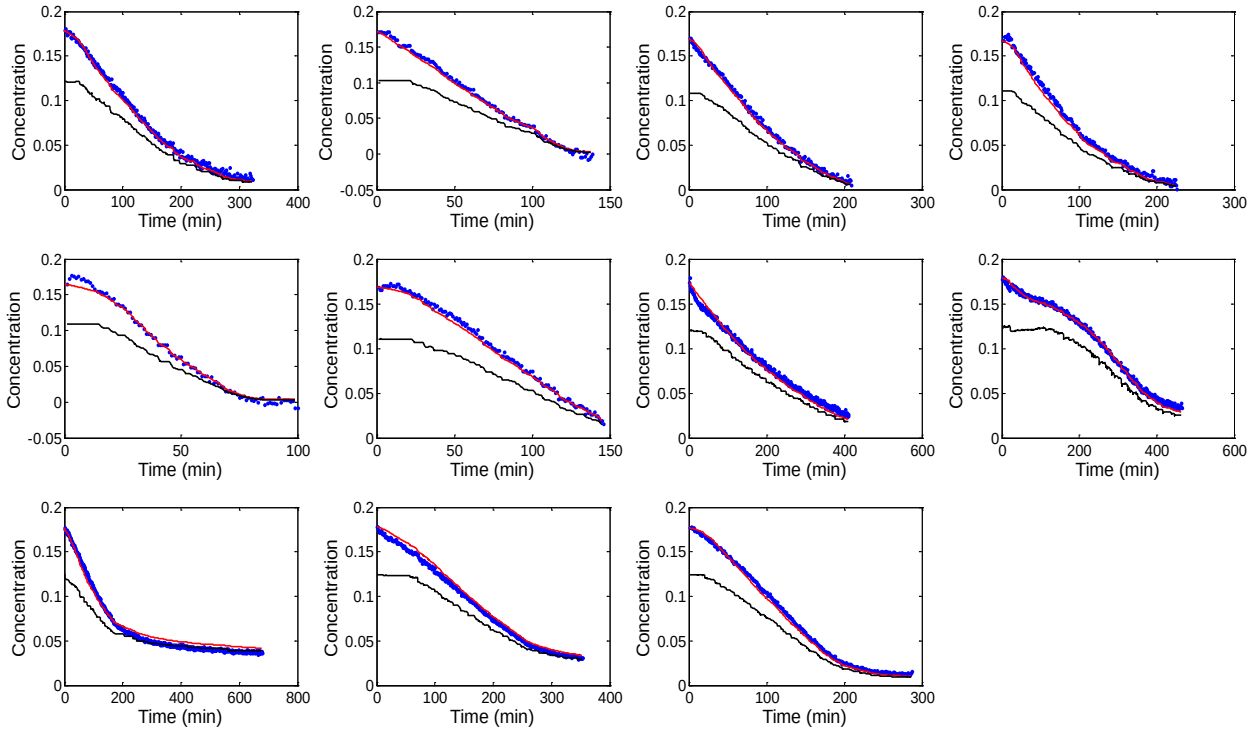

Figure 3.3: Desupersaturation curves for the control experiments at the calculated optimum (Equations 3.15) for growth only when the upper bound on the exponent, g, is relaxed (Equation 3.22), with $\ln k_g = 0.686$ and $g = 3.00$. The lower black curve (—) is the solubility, the red curve (—) is the model output, and the blue dot (•) marks the experimental solute concentration measurements.

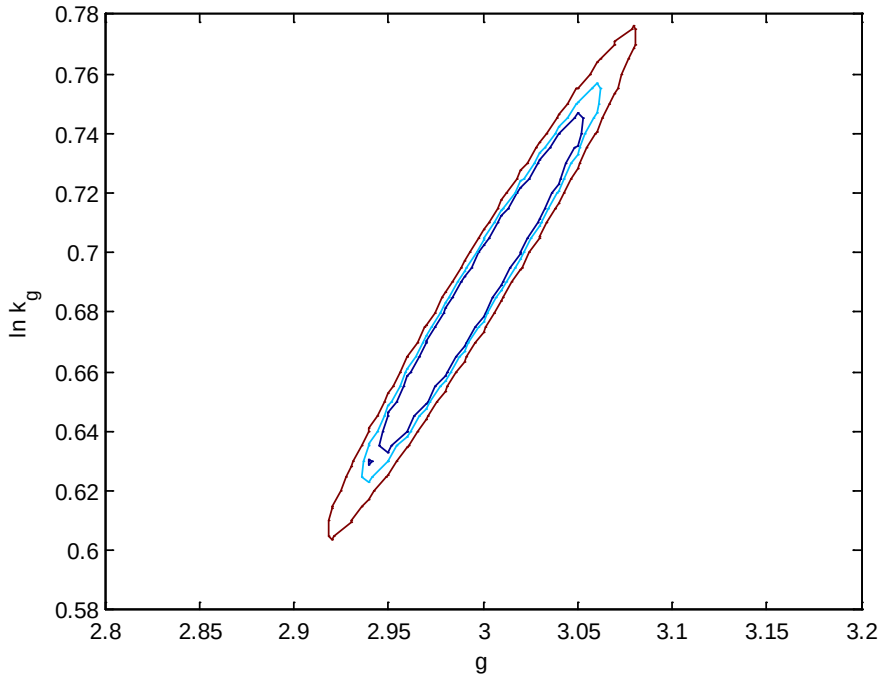

Figure 3.4: Estimated 90%, 95%, and 99% confidence regions for the growth parameters, $\ln k_g$ and g, when the data from all eleven sets of "control" experiments are used in the parameter estimation (Equation 3.15), for the case where the upper bound on the growth exponent, g, is relaxed (Equation 3.22). The nominal values of the growth parameters are reported in the caption of Figure 3.3.

3.10 Tables

Table 3.1: Confidence intervals for the log growth prefactor, $\ln k_g$, for $g = 2$ about an optimal value of $\ln k_g = -0.331$ (Equations 3.15-3.16). At 99% confidence, $\ln k_g$ is within 6% of the calculated optimum.

Confidence level	Lower bound	Upper bound
90%	−0.343	−0.319
95%	−0.345	−0.317
99%	−0.350	−0.312

CHAPTER 4

STEADY-STATE MODEL AND DESIGN OF MULTI-STAGE SLUG-FLOW CRYSTALLIZATION

4.1 Introduction

In the pharmaceutical industry, consistent in-spec products from a well-defined robust crystallization process design are crucial for both FDA regulation and operational practice (Yu et al., 2004; Nagy et al., 2008). Continuous-flow tubular crystallizers have shown potential for high reproducibility and process efficiency at low capital and production cost (Alvarez & Myerson, 2010; Lawton et al., 2009; Fergusen et al., 2012; Vacassy et al., 2000; Jiang et al., 2014; Eder et al., 2010; Eder et al., 2011). A recent advancement that combines the advantages of continuous and batch crystallizers is the air/liquid slug flow crystallizer (Jiang et al., 2014; Eder et al., 2010; Eder et al., 2011; Eder et al., 2012) which has unique advantages including narrow residence time distribution, no stirrer necessary, and easy postcrystallization separation. The potential application of slug flow crystallization in the final stage of pharmaceutical manufacturing makes this design study necessary.

Similar to the batch crystallizer, a robust slug flow crystallization process comes from a good understanding of how the supersaturation profile is affected by design variables (e.g., method and speed of suprersaturation generation) and corresponding implementation (Fujiwara et al., 2002; Zhou et al., 2006; Togkalidou et al., 2001). For example, supersaturation shall be minimized so as to avoid impurity incorporation and secondary nucleation (Jiang et al., 2012; Jiang et al., 2014), which is important for slug flow crystallization with possibly short residence

time (as short as on the order of minutes) (Jiang et al., 2014, Eder et al., 2012) and with fast heat transfer (from large surface area to volume of tubular crystallizers).

In this chapter, cooling crystallization is used to demonstrate the design of a slug flow continuous crystallization process with bounds for supersaturation. Two common methods of cooling are compared: heat baths and shell and tube heat exchangers (Levenspiel, 1962). The effect of design variables on the supersaturation profile is analyzed (e.g., temperatures and locations of heat baths/exchangers, length of tubing). A population balance model for the batch crystallizer (Gunawan et al., 2004; Hulburt & Katz, 1964; Randolph & Larson, 1974; Chung et al., 1999) was applied to individual slugs, with the batch residence time replaced by continuous residence time (running time). Unlike past studies that involve modeling or mathematical analysis of similar continuous crystallizers (all for different crystallization processes (Eder et al., 2010; Kubo et al., 1998), we not only analyzed our experimental proof-of-concept demonstration (Jiang et al., 2014), but also checked the effect of the design variables and applied optimization techniques (e.g. number of heat exchangers, length of tubing in each heat bath/exchanger) while minimizing the total equipment/material use in the design.

4.2 Methodology

A well-mixed batch crystallizer can be modeled using the population balance equation (Hulbert & Katz, 1964; Randolph & Larson, 1974, Gunawan et al., 2004)

$$\frac{\partial f}{\partial \tau} + \frac{\partial (Gf)}{\partial L} = B\delta(L), \tag{4.1}$$

$$f(\tau = 0, L) = f_0(L), \tag{4.2}$$

where G and B are growth and nucleation rates, respectively, f is the distribution of particle sizes at residence time, τ, L is an internal dimension of particle size, and δ is the Dirac delta.

A schematic for one of the slug-flow crystallizers investigated in this chapter is in Figure 4.1. For the first system, a liquid solution containing solute and solvent(s) enters a tube and then undergoes ultrasonication under supersaturated conditions to generate seed crystals. The slurry containing seed crystals is then combined with a stream of air under flow conditions in which slugs spontaneously form. The inlet concentration in the slugs is denoted by C_0, and the inlet temperature by T_0. The tube passes first into a temperature bath of temperature, T_1. The bath is agitated to provide spatially uniform temperature and to promote heat transfer between the liquid in the bath and outer surface of the tube. The length of tubing inside the first bath is denoted by ℓ_1. The tube then passes into a second bath at a different temperature, T_2. The length of tubing in the second bath is denoted by ℓ_2, and the length of tubing in the interval between (and outside of) adjacent baths in denoted by ℓ_{int}. A total of four temperature baths are included in the experimental configuration.

The alternative system investigated here replaces the constant temperature baths with counterflow, single pass, shell and tube heat exchangers (Figure 4.2). While the inlet shell-side temperature is equal for each heat exchanger, i, the length, ℓ_i, and cooling water flowrate, $\dot{m}_{c,i}$, can differ.

4.3 Mathematical modeling of slugs as batch crystallizers

Each slug is considered well-mixed (Kashid et al., 2005; Jiang et al., 2014), so each slug operates as an individual batch crystallizer that is physically transported down the tube. For batch systems under low supersaturation, where nucleation can be considered negligible, the term on the right hand side of Equation 4.1 can be neglected for the batch step. The population balance model describing the evolution of the crystal size distribution in each slug is reduced to

$$\frac{\partial f}{\partial \tau} + G\frac{\partial f}{\partial L} = 0 \tag{4.3}$$

where τ is the time from when a slug enters the first bath. Growth rate can be defined for this system as

$$G = k_g[C - C_{sat}(T)]^g \tag{4.4}$$

where $k_g = 6.353$ and $g = 1.0$ are fitting parameters (Jiang et al., 2012), C_{sat} is the saturation concentration which is a function of temperature, and C and T are the bulk concentration and temperature, respectively. A typical slug in the first bath starts at the concentration, $C_0 = 0.16\,\text{g}$ LAM/g solution, and temperature, $T_0 = 64.6^\circ\text{C}$, at supersaturated or saturated conditions ($C_0 = C_{sat}(T_0)$), and the inlet seed mass is $m_{seed} = 2.86\times10^{-9}\,\text{g}$. The inlet crystal size distribution (CSD), f_0, in the simulation study is given by (Chung et al., 2000; Togkalidou et al., 2004)

$$f_0(L) = \begin{cases} aL^2 + bL + c, & \text{for } L_{\min} \le L \le L_{\max} \\ 0, & \text{otherwise} \end{cases}. \tag{4.5}$$

The CSD is assumed symmetrical with the peak at $\bar{L} = 5\mu\text{m}$ and distribution width, $w = 2\mu\text{m}$, which are estimated based on optical microscopy measurement. Equation 4.5 is equal to zero at $L = \bar{L} \pm w/2$, so that,

$$L_{\min} = \bar{L} - \frac{w}{2} \tag{4.6}$$

$$L_{\max} = \bar{L} + \frac{w}{2} \tag{4.7}$$

The parameters a, b, and c in Equation 4.5 can be determined by analytically solving the system of linear equations:

$$(L_{\max}^6 - L_{\min}^6)\frac{a}{6} + (L_{\max}^5 - L_{\min}^5)\frac{b}{5} + (L_{\max}^4 - L_{\min}^4)\frac{c}{4} = \frac{m_{seed}}{m_{solvent}\rho_{seed}}, \tag{4.8}$$

$$aL_{\max}^2 + bL_{\max} + c = 0, \tag{4.9}$$

$$aL_{\min}^2 + bL_{\min} + c = 0. \tag{4.10}$$

Attrition, aggregation, agglomeration, breakage, and nucleation within each slug are considered to be negligible as has been shown in experiments (Jiang et al., 2014). The low levels of these phenomena are associated with the lack of any mixing blade, static mixers, or other internals to induce such phenomena for the levels of supersaturation that occur in the experiments. The population balance model can be solved by the method of characteristics and the moments can be computed either from the derived crystal size distribution or by solving the ordinary differential equations derived by applying the method of moments to the population balance model (Hulburt & Katz, 1964; Randolph & Larson, 1974; Chung et al., 1999; Togkalidou et al., 2001; Gunawan et al., 2004),

$$\begin{aligned} \frac{d\mu_0}{d\tau} &= B \\ \frac{d\mu_1}{d\tau} &= G\mu_0 + Br_0 \\ \frac{d\mu_2}{d\tau} &= 2G\mu_1 + Br_0^2 \\ &\vdots \end{aligned}, \tag{4.11}$$

where the kth order moment, μ_k, is given by

$$\mu_k(\tau) = \int_0^\infty f(\tau, L) L^k dL. \tag{4.12}$$

A solute balance for the system is given by

$$\frac{dC}{d\tau} = -\alpha\left(3G\frac{d\mu_2}{d\tau} + Br_0^3\right). \tag{4.13}$$

Assuming that the slug is thermally well-mixed and its heat capacity, $\hat{C}_p$, is spatially uniform, and that the temperature in the bath is spatially uniform, the total mass and energy balances for a slug are,

$$\frac{dm}{d\tau} = 0, \tag{4.14}$$

$$m\hat{C}_p \frac{dT}{d\tau} = UA(T_i - T) + \frac{m\Delta\tilde{H}_c}{M_c}\frac{dC}{d\tau}, \tag{4.15}$$

$$T(\tau = 0) = T_0 \tag{4.16}$$

where m is the mass of a slug and T is the steady-state temperature as a function of residence time, τ. U is the overall heat transfer coefficient, A is the surface area for heat transfer, and T_i is the temperature of bath i. $\Delta\tilde{H}_c$ and M_c are the heat of crystallization and molecular weight of the solute molecule, LAM.

The analytical solution for the energy balance (Equation 4.15-4.16) in the first bath is

$$T = T_1 + \exp\left(\frac{-UA\tau}{m\hat{C}_p}\right)\left[\int_0^\tau \exp\left(\frac{UA\tau'}{m\hat{C}_p}\right)\frac{\Delta\tilde{H}_c}{\hat{C}_p M_c}\frac{dC}{d\tau}d\tau' + T_0 - T_1\right]. \tag{4.17}$$

Similarly for baths 2–4, assuming temperature does not drop at intervals between adjacent baths (the connection tube between baths in well-insulated and the length is minimized), the temperature can be calculated as

$$T = T_i + \exp\left(\frac{-UA(\tau - \tau_i)}{m\hat{C}_p}\right)\left[\int_{\tau_i}^\tau \exp\left(\frac{UA(\tau' - \tau_i)}{m\hat{C}_p}\right)\frac{\Delta\tilde{H}_c}{\hat{C}_p M_c}\frac{dC}{d\tau}d\tau' + T_{i-1} - T_i\right]. \tag{4.18}$$

The time at which the slug enters bath i, τ_i, is calculated by assuming a constant velocity, v:

$$\tau_i = \frac{1}{v}\left[\left(\sum_{j=1}^{i}\ell_{i-1}\right) + \ell_{\text{int}}(i-1)\right]. \tag{4.19}$$

The overall heat transfer coefficient, U, is composed of three parts: convective heat transfer within the slug surface, conduction through the tube wall, and convective transfer in the bulk cooling water (bath), that is,

$$\frac{1}{U} = \frac{1}{h_{\text{slug}}} + \frac{d_1 \ln \frac{d_2}{d_1}}{2k_w} + \frac{1}{h_{\text{bath}}}. \tag{4.20}$$

The inside and outside diameters of the tubing are $d_1 = 3.1$ mm and $d_2 = 6$ mm, respectively, and the thermal conductivity, k_w, of silicone rubber is 0.14 W/m-K (Incropera & DeWitt, 2002). The surface area, A, for heat transfer is assumed to be the contact area between the slug and the tube wall, which is an open cylinder of length 3 mm and diameter 3.1 mm. The term, h_{slug}, was obtained using the Sieder-Tate correlation for the Nusselt Number, Nu (Sieder & Tate, 1936),

$$\text{Nu} = \frac{h_{\text{slug}} d_1}{k_s} = 0.023 \,\text{Re}^{0.8} \,\text{Pr}^{1/3} \left(\frac{\mu_{c,s}}{\mu_{w,s}} \right), \tag{4.21}$$

where Re and Pr are the Reynolds and Prandtl numbers, respectively, and k_s is the thermal conductivity of the slug solution. The ratio of dynamic viscosities, μ_s, for the slug solution at the center and wall is assumed to be unity. The following relationship is used to calculate the term h_{bath} (Chilton et al., 1944).

$$\text{Nu} = \frac{h_{bath} D}{k_b} = 0.87 \,\text{Re}_N^{2/3} \,\text{Pr}^{1/3} \left(\frac{\mu_{c,b}}{\mu_{w,b}} \right)^{0.14}, \tag{4.22}$$

where *D* is the inside diameter of the agitated vessel and kb is the thermal conductivity of the bath fluid (in this case, water). Again the ratio of dynamic viscosities for the bath fluid is assumed to be unity. The Reynolds number in equation 4.22 for an agitated vessel, Re_N, is given by

$$\mathrm{Re}_N = \frac{N \rho_b L_a^2}{\mu_{c,b}}, \tag{4.23}$$

where N is the agitator speed, L_a is the agitator diameter, and ρ_b and $\mu_{c,b}$ are the density and dynamic viscosity of the bath fluid. The values of the terms in Equation 4.15 are compared in Table 4.1.

For the multi-bath system, an optimal choice for the bath temperatures and tube lengths is based on the objective of low maximum supersaturation level within the metastable zone to maintain purity and avoid secondary nucleation within the liquid slugs passing through the tube. In the case of the four-bath system, the optimization is given by

$$\min_{\substack{T_1,T_2,T_3 \\ \ell_1,\ell_2,\ell_3,\ell_4}} w_1 \max\left\{0,[C_f - C_{sat}(T_4)]\right\} + w_2 S_{\max} + w_3 \sum_i \ell_i \,. \tag{4.24}$$

In the first term, C_f, the final concentration in the system, is compared to $C_{sat}(T_4)$, the saturation concentration at the final temperature, to force high yield. In the second term, $S_{\max}$ is simply the maximum supersaturation within the system. The third term is the total length of tubing.

If instead the temperature baths are replaced with two concentric tubes in the form of a single-pass, counterflow, shell-and-tube heat exchanger, the energy balance takes the form

$$d\dot{q} = \dot{m}_c \hat{C}_{p,c} dT_c = \dot{m}_h \hat{C}_{p,h} dT_h, \tag{4.25}$$

where $\dot{m}_c$ is the mass flowrate, $\hat{C}_{p,c}$ is the constant pressure heat capacity, and T_c is the temperature of cooling water in the shell. $\dot{m}_h$, $\hat{C}_{p,h}$, and T_h represent the same properties for the slug stream in the tube. The differential heat transfer, $d\dot{q}$, can also be written as

$$d\dot{q} = U \Delta T dA. \tag{4.26}$$

The integrated from of Equation 4.26 is

$$\dot{q} = UA\frac{\Delta T_2 - \Delta T_1}{\ln(\Delta T_2 / \Delta T_1)}, \tag{4.27}$$

where

$$\Delta T_1 = T_{h,in} - T_{c,out}, \tag{4.28}$$

$$\Delta T_2 = T_{h,out} - T_{c,in}. \tag{4.29}$$

As before, we define $T_{h,in} = 64.6^{\circ}\mathrm{C}$ and $T_{h,out} = 30.0^{\circ}\mathrm{C}$. The heat transfer coefficient is similar to the value given above. The heat capacity of the hot stream is again approximated as the heat capacity of water alone; i.e. $C_{p,c} = C_{p,h} = 4.187\frac{\mathrm{J}}{\mathrm{g}\cdot\mathrm{K}}$. The inlet temperature of the cooling stream of water is approximated as room temperature, $T_{c,in} = 25^{\circ}\mathrm{C}$. The mass flowrate of the hot stream is calculated by multiplying the mass of a slug, $2.12\times10^{-2}\,\mathrm{g}$, by the slug flowrate, 2 slugs/s. The surface area for heat transfer is given by

$$A = \beta\pi\ell_{hx}d_1, \tag{4.30}$$

where ℓ_{hx} is the length of the heat exchange, $d_1 = 3.1\,\mathrm{mm}$ is the inner tube diameter, and β is the average fraction of the tube estimated to be in contact with slugs.

At this point, we are still left with three undefined variables, $T_{c,out}$, $\dot{m}_c$, and ℓ_{hx}. For a first pass on the calculation, if we keep the temperature differences constant; i.e., $\Delta T_1 = \Delta T_2 = \Delta T$, then the Equation 4.21 becomes $\dot{q} = UA\Delta T$, and we have defined $T_{c,out} = 59.6^{\circ}\mathrm{C}$. Using Equations 4.25 and 4.27, we can then calculate the two remaining variables, since the hot stream is completely defined. The temperature profile, using the method described above (and neglecting heat of crystallization) is given by Figure 4.3.

The outlet temperatures of a shell and tube heat exchanger can be calculated using the effectiveness, η, defined as (Kays & London, 1984)

$$\eta = \frac{1 - e^{-\alpha}}{1 - \frac{W_c}{W_s} e^{-\alpha}}, \tag{4.31}$$

where W_s and W_c are the heat capacity rates of slugs and cooling water –and the exponent, α, is defined by

$$\alpha = U \pi D \ell \beta \left(\frac{1}{W_c} - \frac{1}{W_s} \right) \tag{4.32}$$

where U is the overall heat transfer coefficient, D is the tube diameter, ℓ is the length of the tube and β is the scale factor to account for the surface area in contact with slugs (as defined above). The outlet temperature of the slug stream is then

$$T_{s,out} = T_{s,in} + \frac{W_c}{W_s} \eta \left(T_{c,in} - T_{s,in} \right) \tag{4.33}$$

where the inlet temperatures $T_{c,in}$ and $T_{s,in}$ of the cooling water and slug stream, respectively, are known. For the indeterminate case where $W_c = W_s$, L'Hopital's rule gives

$$\lim_{W_c \to W_s} \eta = \frac{U \pi D \ell \beta}{U \pi D \ell \beta + W_s} \tag{4.34}$$

If we ignore the curvature caused by the non-constant ΔT_{LM}, we can apply a linear approximation to the temperature in the tube as a function of distance from the heat exchanger entrance, x,

$$T_s(x) = T_{s,in} - \frac{T_{s,out} - T_{s,in}}{\ell} x \tag{4.35}$$

For a given inlet temperature of cooling water and total length of tubing, the lengths of tubing in each heat exchanger can be chosen to minimize the supersaturation over the total length of tube while also maximizing the total yield. The objective function is given by

$$\begin{aligned} &\min\left[S_{\max} + \varepsilon_1 \max\left\{ C_f - C_{sat}(T_{c,in}), 0 \right\} \right] \\ &0 < \ell_i \le \ell_{total}, \; i = 1 \ldots n \\ &\ell_n = \ell_{total} - \sum_{i}^{n-1} \ell_i \\ &0 < \dot{m}_{c,i} \le \dot{m}_{c,\max}, \; i = 1 \ldots n \end{aligned} \tag{4.36}$$

The value of ε_1 in Equation 4.36 determines the tradeoff between maximum supersaturation and yield in a system with fixed tube length.

4.4 Results and Discussion I: Constant Temperature Baths

For the multi-bath system described above, the optimal solution provided by Equation 4.24 is shown in Figure 4.4. Parameter values for Figure 4.4 are shown in the first row of Table 4.2. Table 4.2 provides the optimal parameters for the literature values of the growth kinetics as well as optimal values corresponding to 20% relative error in growth kinetics parameters. Figures 4.5-4.7 show the simulation output for the parameters in subsequent rows of Table 4.2.

In each case the optimum results in four peaks of supersaturation with roughly equal height, as determined by the bath temperature. The optimal lengths allow the supersaturation to approach zero before entering a new bath. Increasing g and decreasing k_g both increase the length of tubing and, therefore, amount of time necessary to achieve the desired results. Increasing k_g decreases the time necessary. In other words, the length of tubing necessary to achieve the maximum yield increases with a decrease in growth rate. Especially at low supersaturation, the value of the exponent, g, has a large effect on the growth rate, and

correspondingly, the length of tubing required. The growth rate has a comparatively small effect on the values of the optimal bath temperatures.

Alternatively, Table 4.3 shows the effect on two terms of interest when a 20% error in actual growth kinetics parameters are not taken into account. To construct this table, the length and temperature values given by the first row of Table 4.2 are used in each case, but the values of the growth kinetics parameters are altered as shown to demonstrate the simulation results if the actual growth kinetics parameters for the system are 20% different than those reported in literature. Figures 4.8–4.10 provide the simulation results corresponding to the rows of Table 4.3.

The same effect is seen. When the true growth rate is more than that predicted by literature, the lengths corresponding to the original growth rate are more than sufficient, so a slight improvement is seen in the yield, and the maximum supersaturation remains unaffected. When the true growth rate is slightly less, there is a decrease in yield and an increase in the maximum supersaturation. When the true growth rate is much lower than predicted, the system does not act as desired. If the increase in maximum supersaturation is not overly detrimental, a precautionary increase in the final tube length can still guarantee that the maximum yield is attained for the given final temperature.

4.5 Results and Discussion II: Shell and Tube Heat Exchangers

For the system of shell and tube heat exchangers in series, for each heat exchanger, the optimum occurs when the length of the tube approaches infinity, and the cooling water flowrate is high enough to remove all of the excess heat from the system (Figure 4.11). If the cooling water flowrate is given a maximum value of 50 mg/s and the total length of tubing is restricted to

300 m, Figure 4.12 can be constructed from the data in Table 4.4 for n heat exchangers in series. Figure 4.12 demonstrates the trade-off between the two objectives as well as the diminishing returns of adding heat exchangers beyond $n = 3$. The simulation results around the trade-off point (the left-most non-trivial solution) are shown below (Figures 4.13–4.16) for each value of n.

Figures 4.13–4.16 show an increase in the number of supersaturation peaks as the number of heat exchangers increase, but the values of supersaturation in this system are lower than those predicted by the multi-bath system by a factor of three, due to the nature of counterflow heat exchange. The yield in either system of heat exchangers is theoretically restricted by the minimum system temperature given a sufficient length of tubing is available.

4.6 Conclusions

Two systems involving continuous, slug-flow crystallization have been investigated using computer simulation. By combining constant temperature cooling baths in series, the temperature of the slugs can be stepped down gradually to maintain low supersaturation, to promote growth over nucleation, yet allowing high yield and purity. The advantage of simplicity is offset by the concern caused by relatively high spikes in supersaturation at the inlet to each bath. An alternative system is suggested which uses counterflow shell and tube heat exchangers in series to lower the temperature more gradually. The shell and tube system provides similar yield, but reduces the maximum supersaturation by a factor of three. For both systems, optimal design parameters are suggested based on predictions provided by the simulations.

4.7 Supplementary Material

The assumption is made that the temperature profile in the shell and tube heat exchanges is linear with respect to length, x (Equation 4.35). The following derivation provides justification in a scenario where this assumption holds true:

For crystallization experiments carried out in a tube, the tube is the shortest and least expensive at slow slug mass flow rates. Under these conditions, the mass flow of the heat transfer fluid will also be low at steady-state conditions, since the change in enthalpy between inlet and outlet for the heat transfer fluid must approximately equal the corresponding change in enthalpy between inlet and outlet for the slugs. Also, fouling is minimized if the tube wall is thermally insulating, so that the temperature gradient is low in the slug near the tube wall. Collectively under these conditions, the overall heat transfer coefficient U given by

$$\frac{1}{U} = \frac{1}{h_c} + \frac{d_1 \ln\left|d_2/d_1\right|}{2k_w} + \frac{1}{h_h} \tag{4.37}$$

will be small, where d_1 is the tube inner diameter, d_2 is the tube outer diameter, k_w is the thermal heat capacity of the tube wall, and h_c and h_h are the cold- and hot-side convective heat transfer coefficients.[1] Below is a proof that the steady-state temperature profile $T_h(z, t=\infty)$ will be approximately linear for low enough overall heat transfer coefficient, U.

The energy balance for a counterflow heat exchanger is a pair of coupled partial differential equations

$$\begin{aligned} m_h C_{p,h} \frac{\partial T_h(z,t)}{\partial t} + \dot{m}_h C_{p,h} \ell \frac{\partial T_h(z,t)}{\partial z} + UA_{LM}\left(T_h(z,t) - T_c(z,t)\right) = 0 \\ m_c C_{p,c} \frac{\partial T_c(z,t)}{\partial t} - \dot{m}_c(t) C_{p,c} \ell \frac{\partial T_c(z,t)}{\partial z} - UA_{LM}\left(T_h(z,t) - T_c(z,t)\right) = 0 \end{aligned} \tag{4.38}$$

[1] Actually, the overall heat transfer coefficient is small if *any* of the individual heat transfer resistances in (2) is high, so that it is only needed to assume that the tube wall is thermally insulating *or* the slug mass flow rate is low.

where T is the radial-averaged temperature, z is the distance from the hot stream (tube side) inlet to a position along the heat exchanger, m is the mass of material in the system, C_p is the constant pressure heat capacity, $\dot{m}$ is the mass flow rate of material, ℓ is the length of the heat exchanger, A_{LM} is the log mean area for heat transfer between the hot and cold streams, denoted by subscripts h and c, respectively.

If the system is considered to be at a steady state, equations (2) can be written as

$$\begin{aligned} \dot{m}_h C_{p,h} \ell \frac{dT_h(z)}{dz} + UA_{LM}\left(T_h(z) - T_c(z)\right) = 0 \\ \dot{m}_c C_{p,c} \ell \frac{dT_c(z)}{dz} + UA_{LM}\left(T_h(z) - T_c(z)\right) = 0 \end{aligned} \tag{4.39}$$

which can be rearranged further to

$$\begin{aligned} \frac{dT_h(z)}{dz} = -K_h\left(T_h(z) - T_c(z)\right) \\ \frac{dT_c(z)}{dz} = -K_c\left(T_h(z) - T_c(z)\right) \end{aligned} \tag{4.40}$$

where

$$\begin{aligned} K_h = \frac{UA_{LM}}{\dot{m}_h C_{p,h} \ell} \\ K_c = \frac{UA_{LM}}{\dot{m}_c C_{p,c} \ell} \end{aligned} \tag{4.41}$$

Subtracting the equations in Equation 4.40 gives

$$\frac{d\left(T_h(z) - T_c(z)\right)}{dz} = K\left(T_h(z) - T_c(z)\right) \tag{4.42}$$

where $K = K_c - K_h$. For low enough overall heat transfer coefficient, U, the value of K is small and[2]

$$T_h(z) - T_c(z) = T_h(0) - T_c(0) \tag{4.43}$$

Insertion into Equations 4.40 gives

$$\begin{aligned} \frac{dT_h(z)}{dz} &= -K_h\left(T_h(0) - T_c(0)\right) \\ \frac{dT_c(z)}{dz} &= -K_c\left(T_h(0) - T_c(0)\right) \end{aligned} \tag{4.44}$$

which gives linear profiles

$$\begin{aligned} T_h(z) &= T_h(0) - K_h\left(T_h(0) - T_c(0)\right)z \\ T_c(z) &= T_c(0) - K_c\left(T_h(0) - T_c(0)\right)z \end{aligned} \tag{4.45}$$

Q.E.D.

[2] The value of K is also small under conditions where $\dot{m}_h C_{p,h} = \dot{m}_c C_{p,c}$, which approximately holds for mass flow rates of comparable value, $\dot{m}_h \approx \dot{m}_c$, when the crystallization solvent and heat transfer fluids are the same.

4.8 Figures

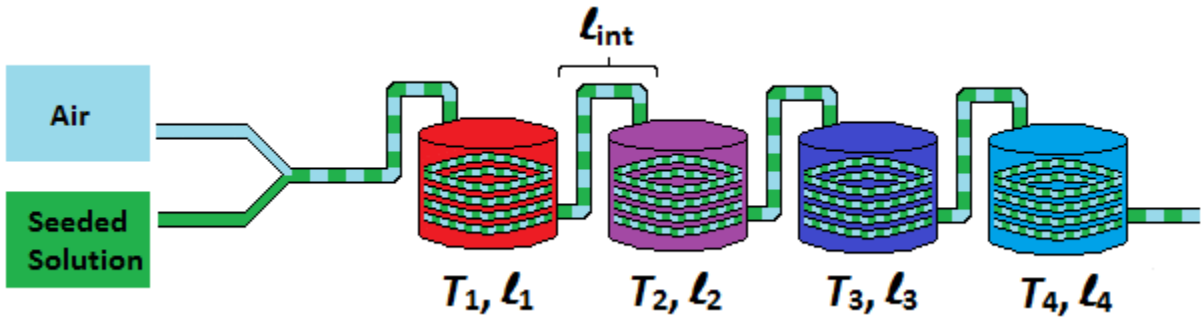

Figure 4.1: Schematic for a multiple bath SFC fed with L-asparagine monohydrate (LAM) in aqueous solution. A typical tube is made of silicone of Teflon with an inner diameter of 3.1 mm. During cooling, the tank temperatures range from 60 to 20 degrees Celsius.

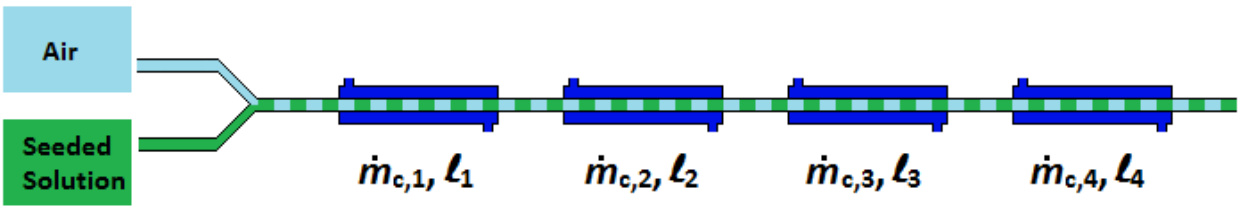

Figure 4.2: Schematic for a multiple shell-and-tube heat exchanger SFC. The temperature of the inlet cooling water in the shell is constant, typically around 25°C. The tube investigated is similar in size to the previous system.

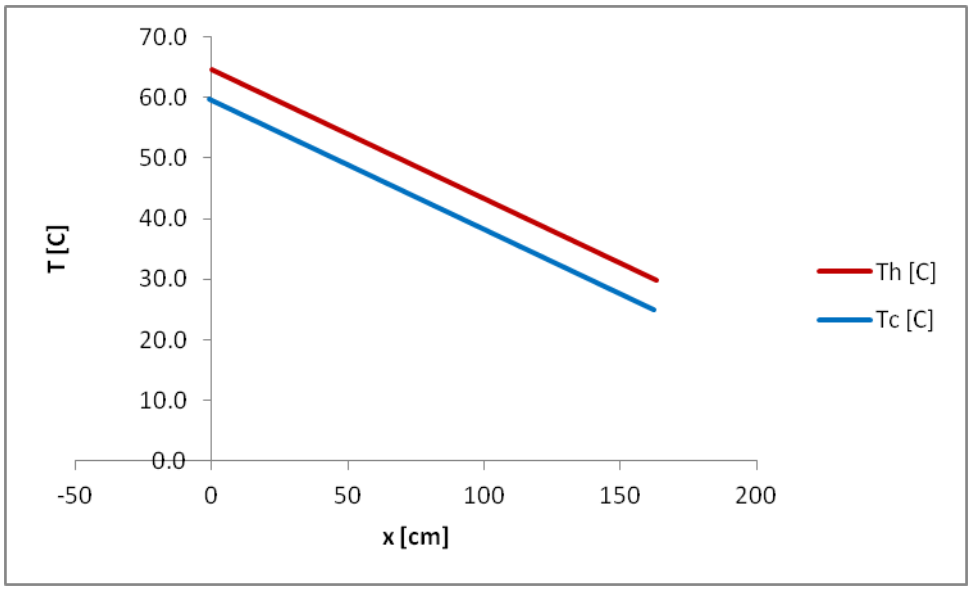

Figure 4.3: Estimated temperature profile of a shell-and-tube heat exchanger designed with constant log mean temperature difference. The red line marks the temperature of slugs in the tube and the blue line marks the temperature of cooling water in the shell.

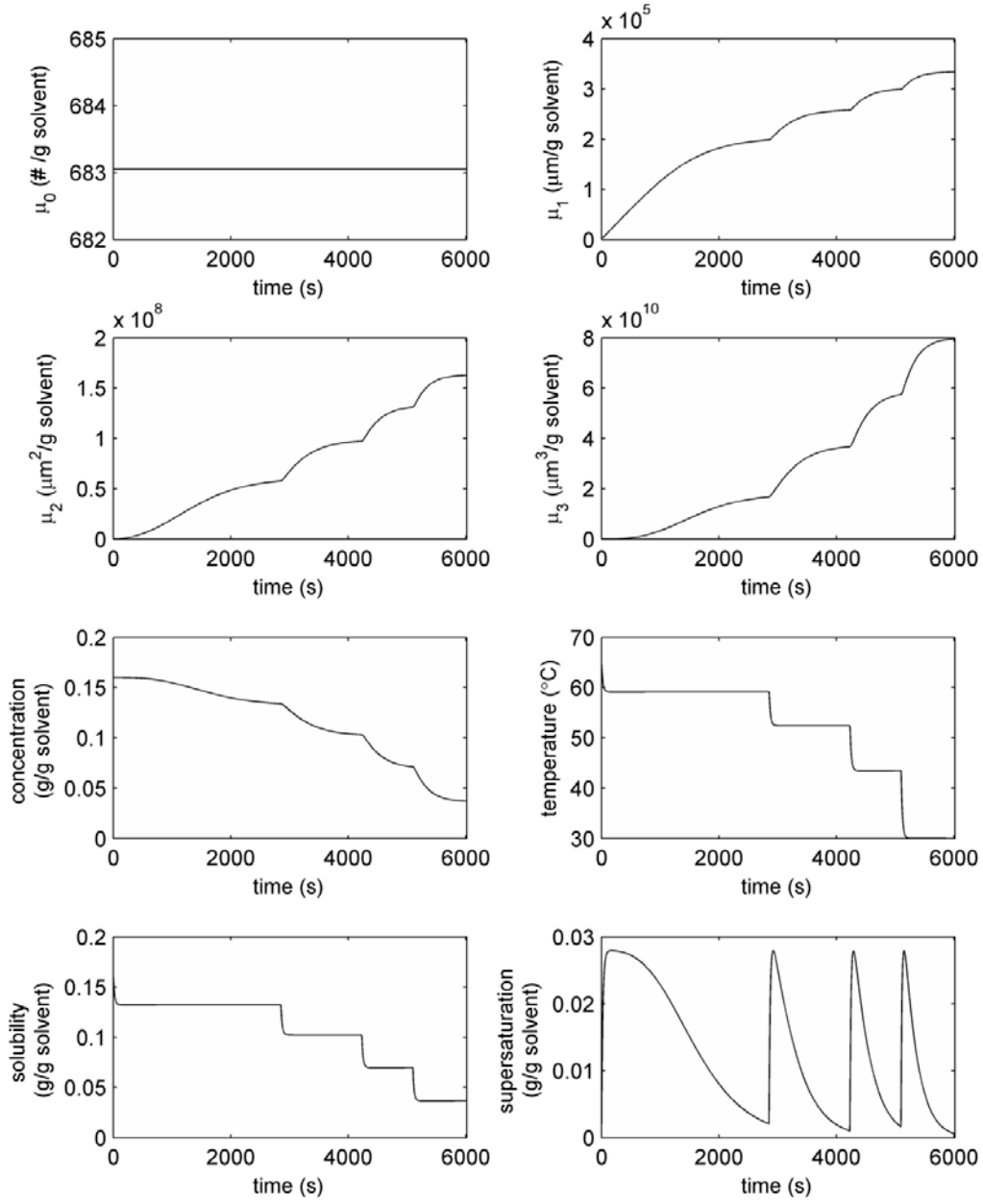

Figure 4.4: Simulation output for the four bath SFC at the calculated optimum. The zeroth-third order moments, concentration, temperature, solubility, and supersaturation curves are shown with respect to time. Sharp supersaturation peaks of equal height at the tank entrance decay toward zero over the residence time in each heat exchanger.

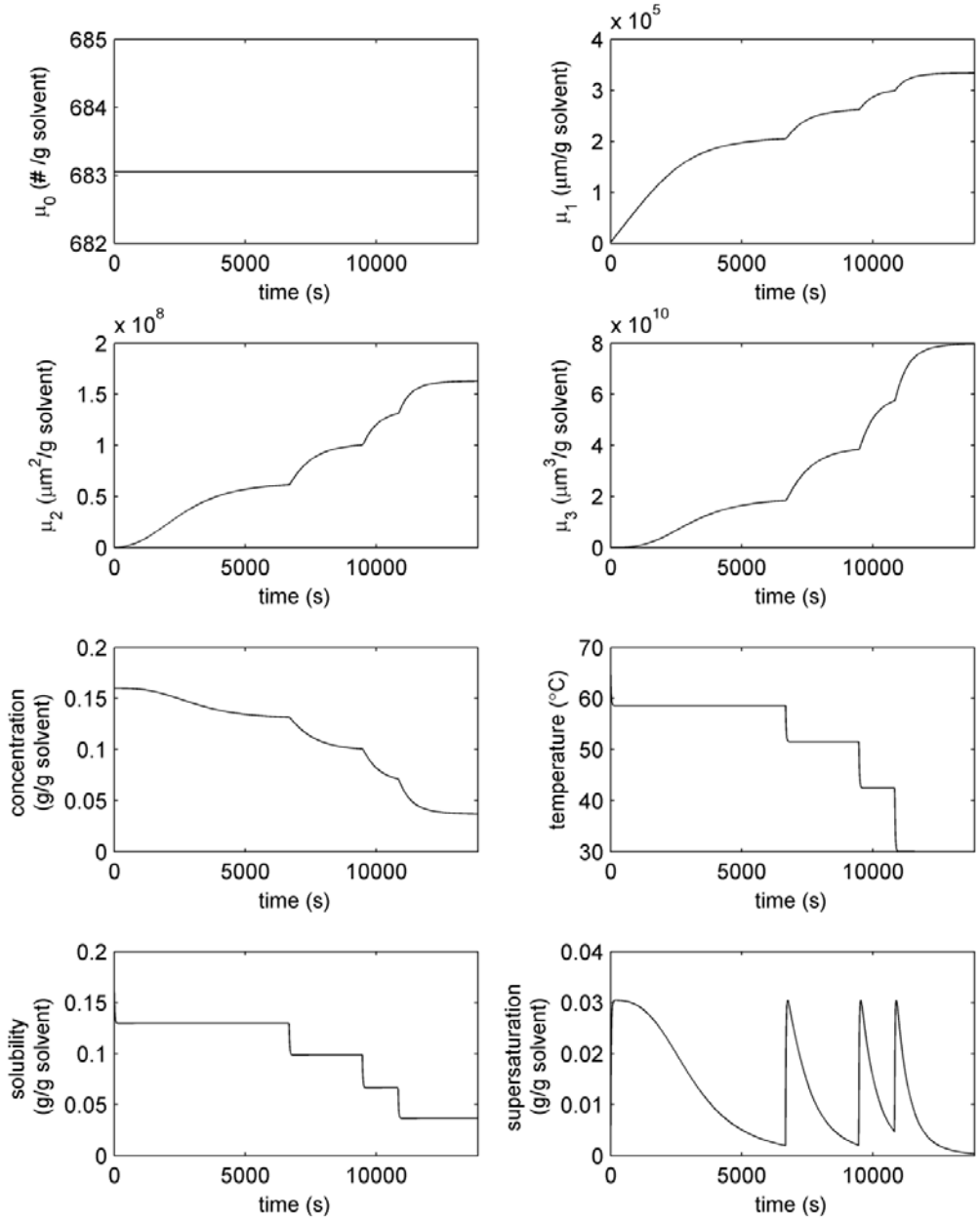

Figure 4.5: Simulation output for the four bath SFC at the new optimum when the actual value of the exponent, g, of Equation 4.4 is increased by 20%. The relatively large decrease in growth rate results in higher supersaturation peaks and a longer overall residence time.

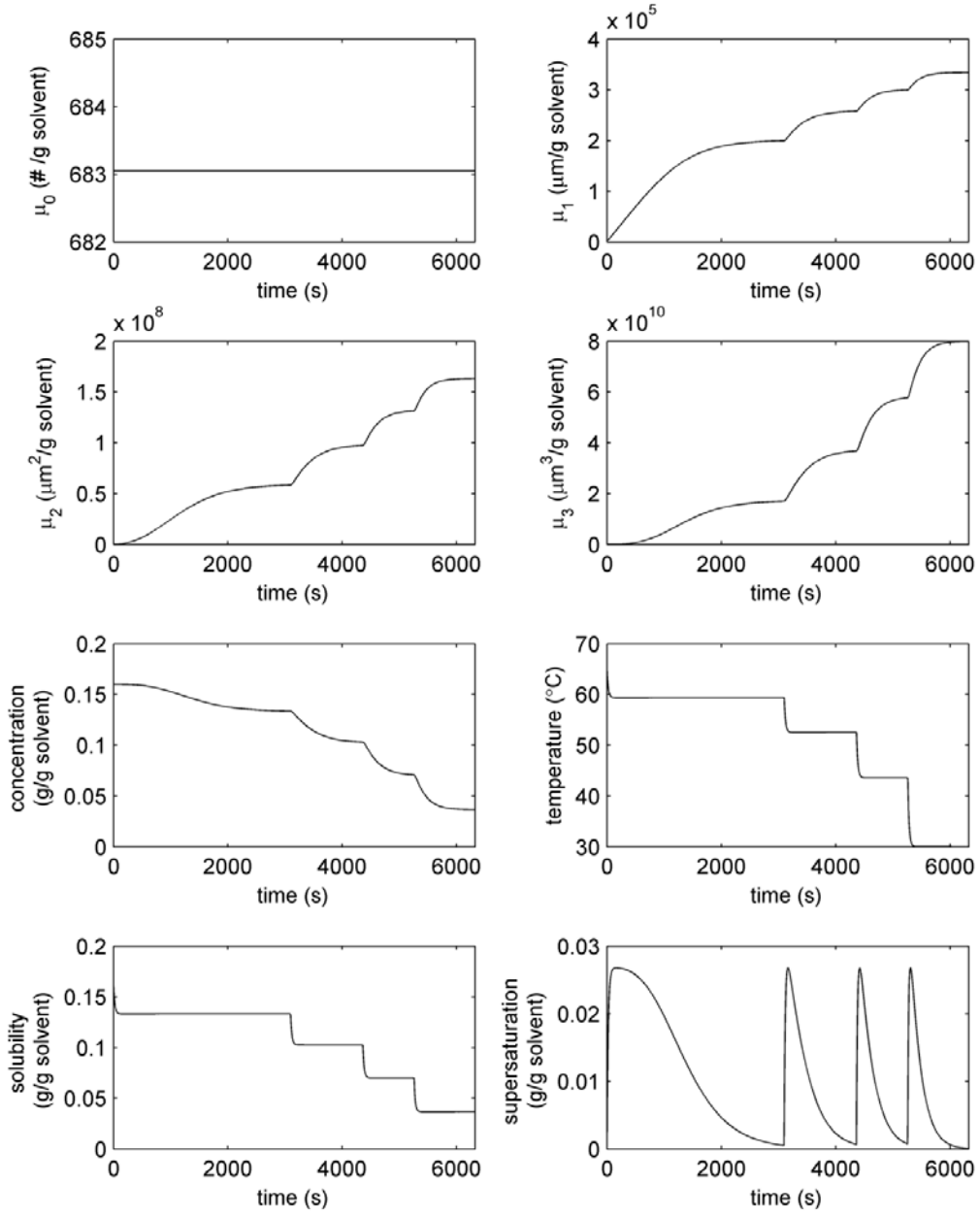

Figure 4.6: Simulation output for the four bath SFC at the new optimum when the actual value of the coefficient, k_g, of Equation 4.4 is increased by 20%. The relatively small increase in growth rate slightly reduces the supersaturation peak height.

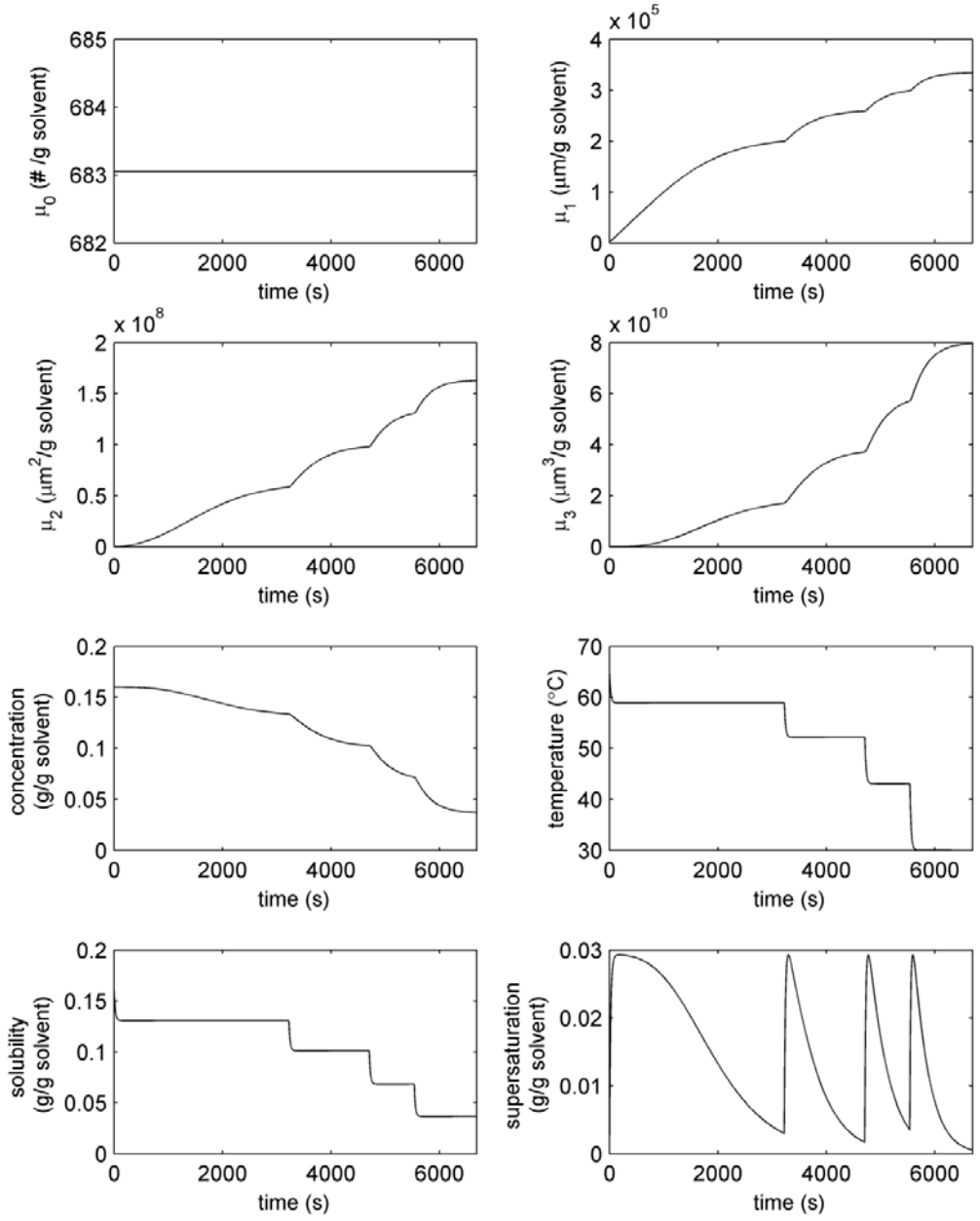

Figure 4.7: Simulation output for the four bath SFC at the new optimum when the actual value of the coefficient, k_g, of Equation 4.4 is decreased by 20%. The relatively small decrease in growth rate results in a slight increase in supersaturation peak height.

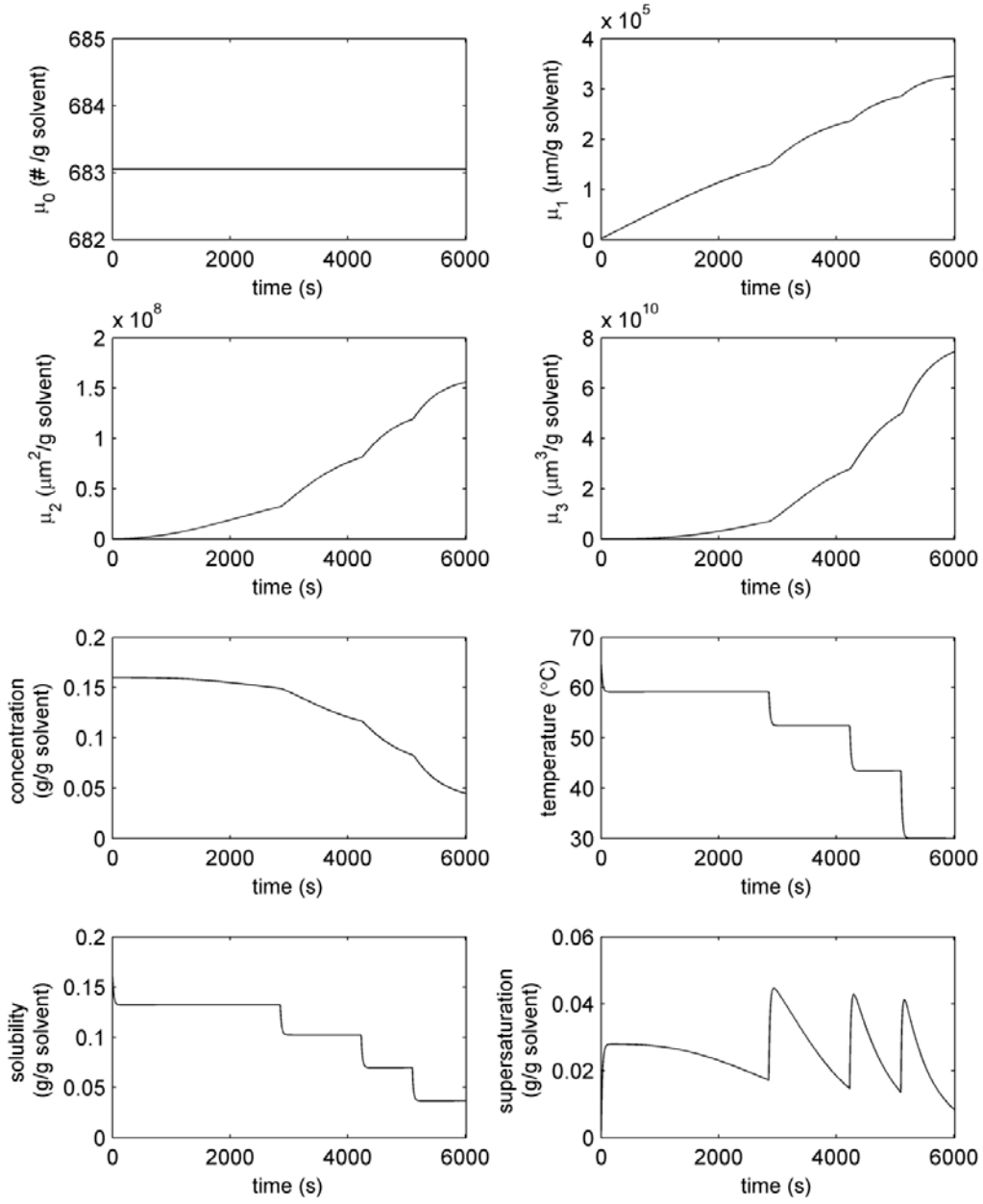

Figure 4.8: Simulation output for the four bath SFC when the value of g is increased by 20% while maintaining the optimal temperatures and lengths predicted by literature values. The relatively large decrease in growth rate results in much higher peaks in the supersaturation and a higher final supersaturation (indicating a lower yield).

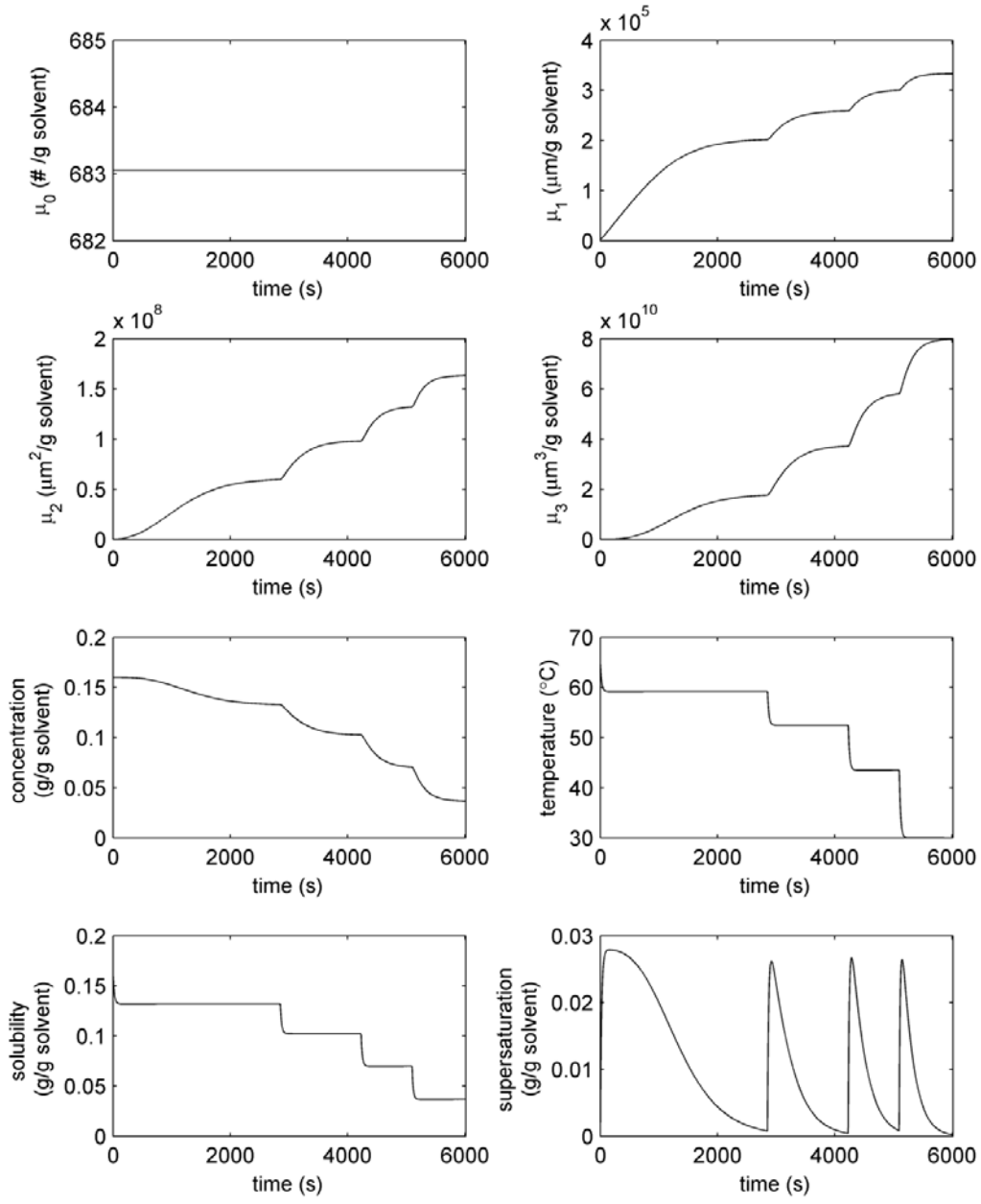

Figure 4.9: Simulation output for the four bath SFC when the value of k_g is increased by 20% while maintaining the optimal temperatures and lengths predicted by literature values. The increase in growth rate results in a slight improvement in yield while having a small effect on supersaturation peak height.

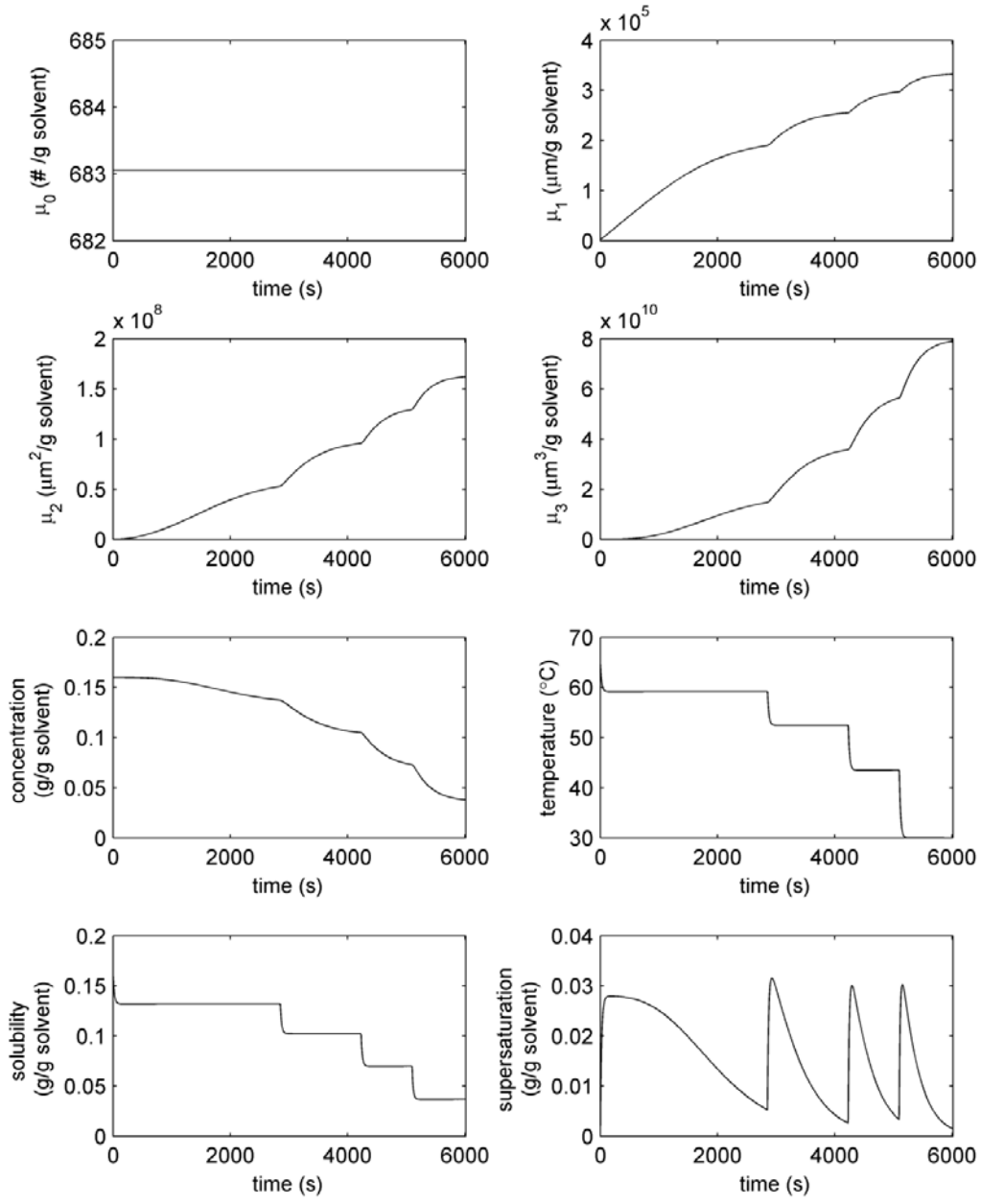

Figure 4.10: Simulation output for the four bath SFC when the value of k_g is decreased by 20% while maintaining the optimal temperatures and lengths predicted by literature values. As seen before, the decrease in growth rate results in higher supersaturation peaks and lower yield.

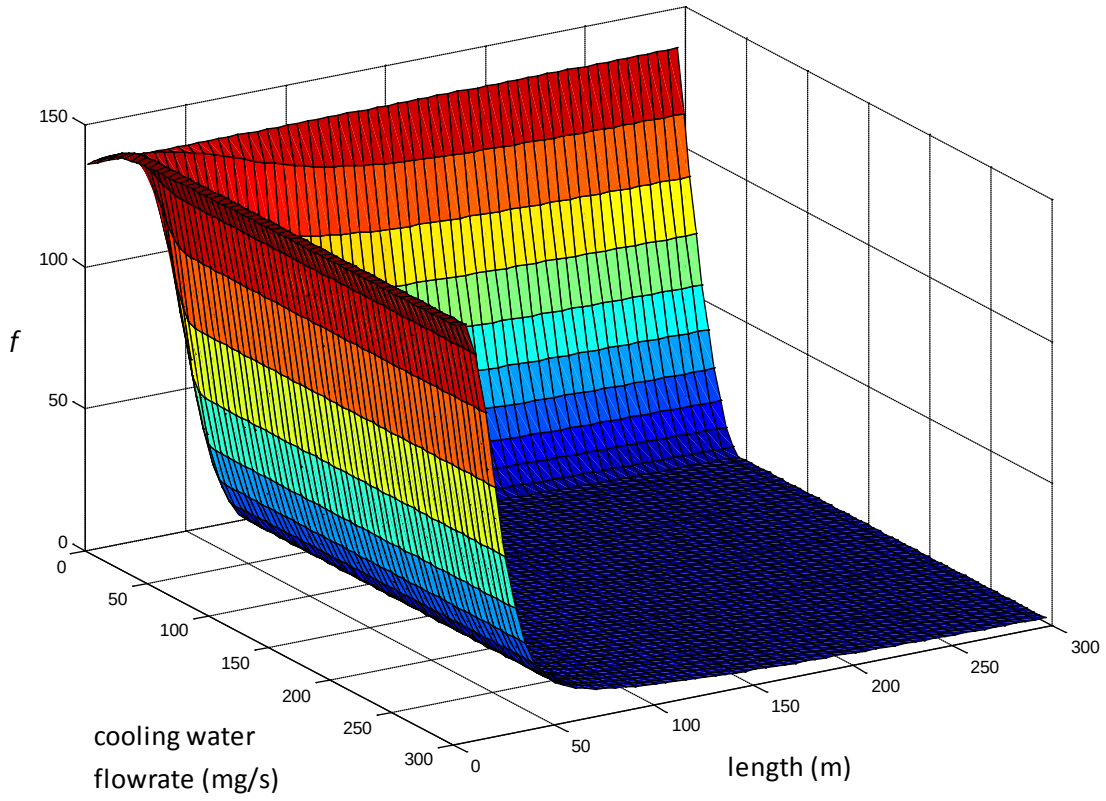

Figure 4.11: The objective function for the shell-and-tube SFC (Equation 4.36) is plotted for a single heat exchanger ($n = 1$), when total length and cooling water flowrate take on a large range of values. The flat surface caused by cooling water flowrate greater than

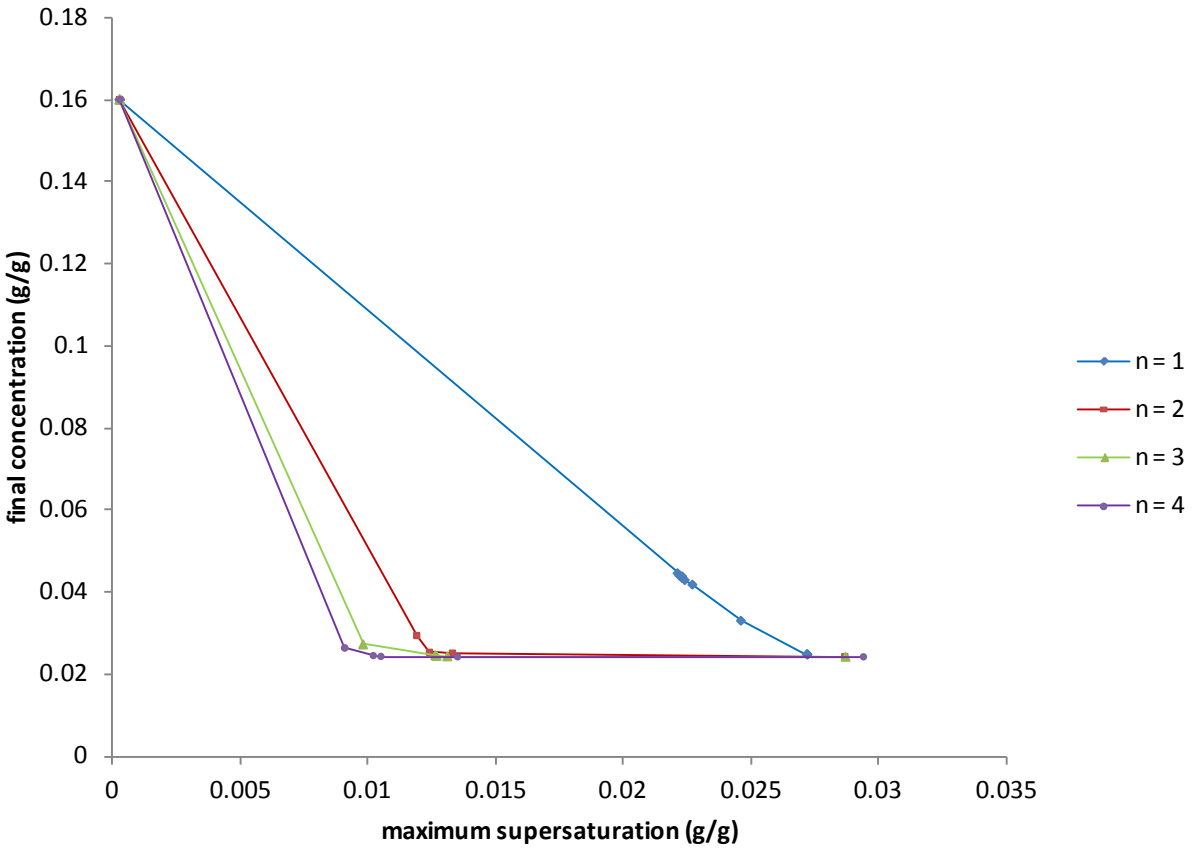

Figure 4.12: Pareto optimality curves for the shell-and-tube SFC with different total number of heat exchangers at a constant total tube length of 300 m. A trade-off point between the remaining two competing objectives provides the optimal values.

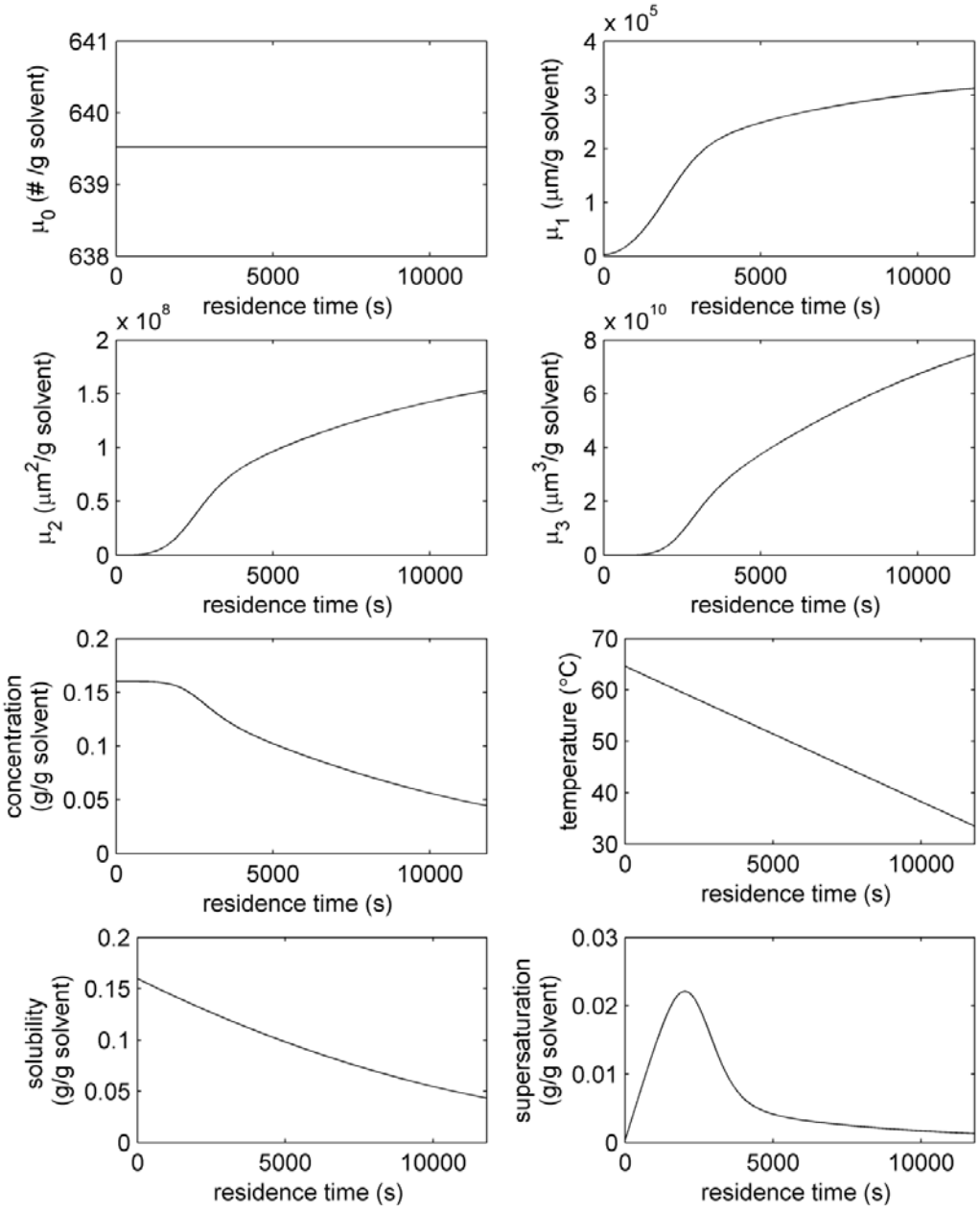

Figure 4.13: Simulation results for the shell-and-tube heat SFC near the trade-off point for $n=1$. A single, rounded peak is observed in the supersaturation profile.

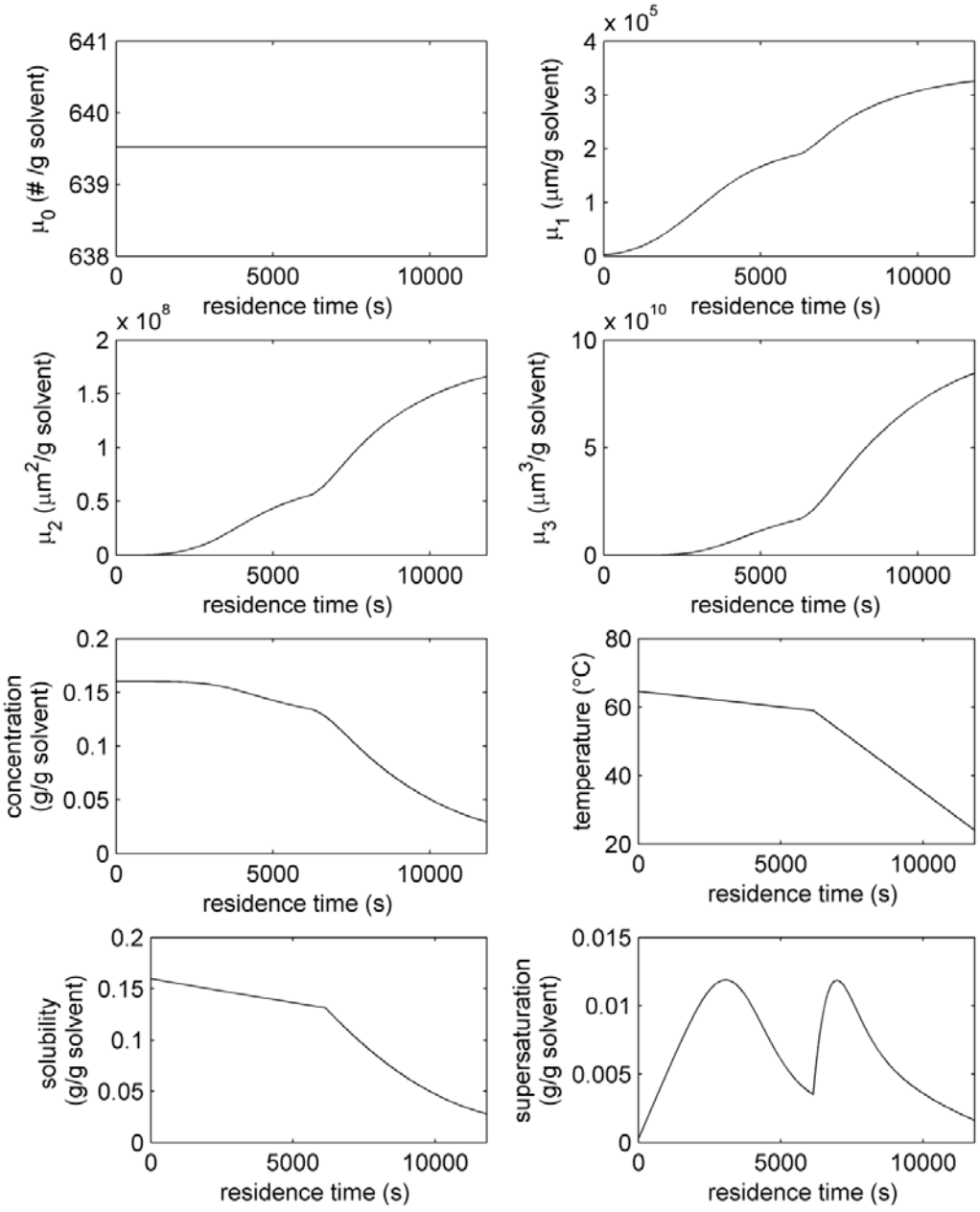

Figure 4.14: Simulation results for the shell-and-tube SFC near the tradeoff point for $n = 2$. Two rounded peaks in supersaturation with a maximum value almost 50% lower than the maximum supersaturation for $n = 1$.

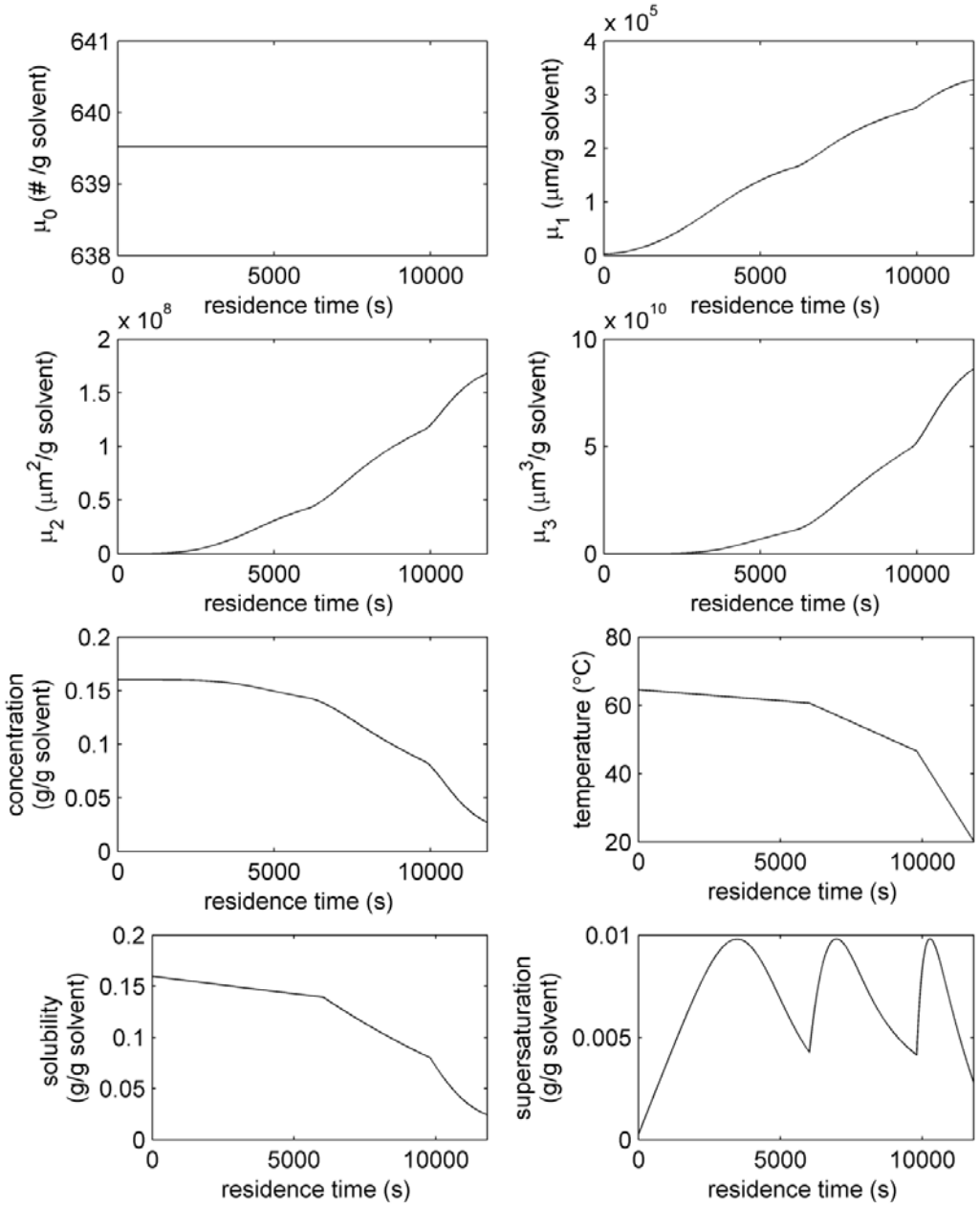

Figure 4.15: Simulation results for the shell-and-tube SFC near the tradeoff point for $n = 3$. Three rounded peaks in supersaturation are observed with a further decrease in the maximum supersaturation when compared to the system when $n = 2$.

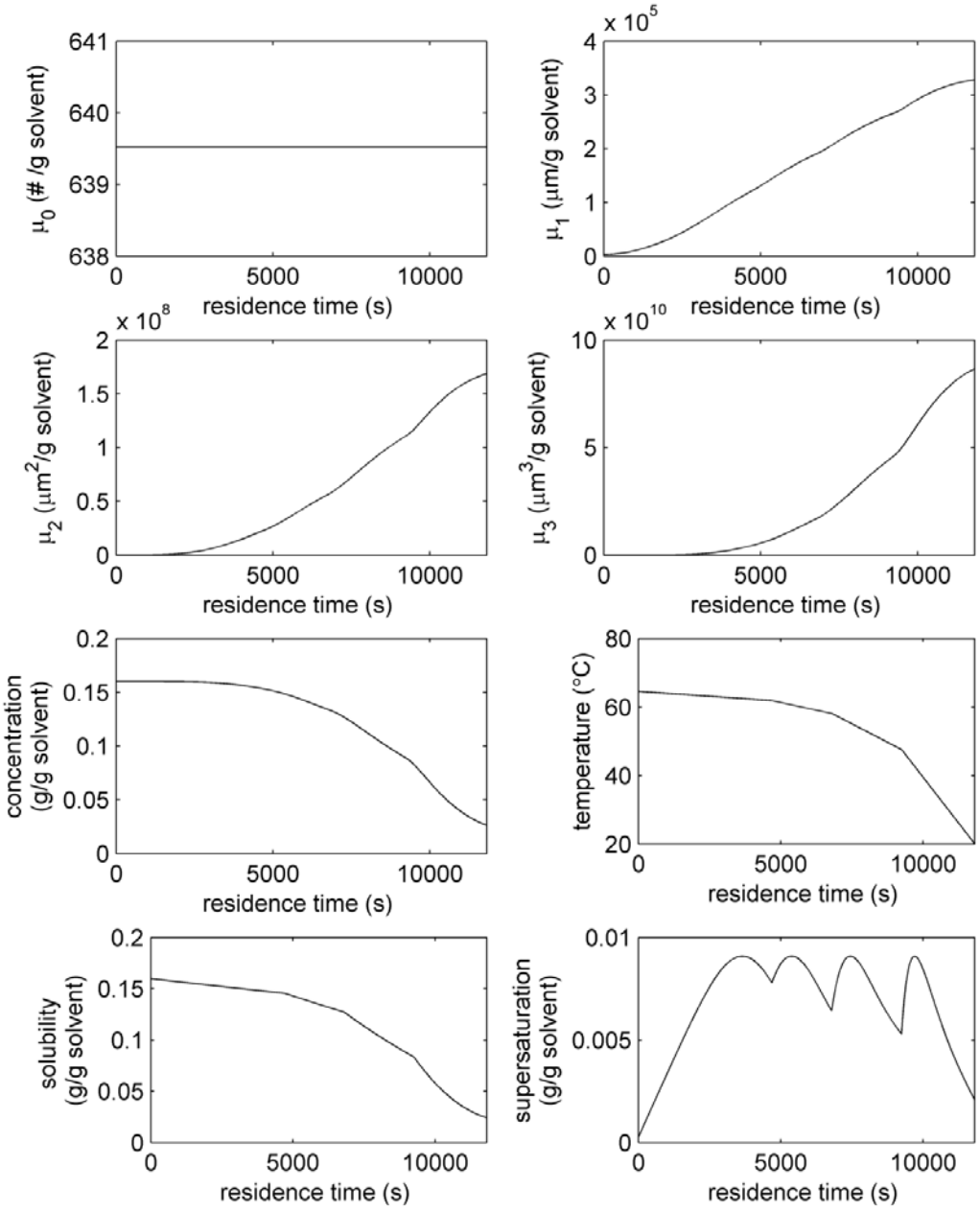

Figure 4.16: Simulation results for the shell-and-tube SFC near the tradeoff point for $n = 4$. Four rounded supersaturation peaks are observed with only a slight decrease in maximum supersaturation over the entire length of the SFC.

4.9 Tables

Table 4.1: Comparison of contributions to the overall heat transfer coefficient for the four tank SFC.[a] The tube wall provides the largest resistance to heat transfer.

h_{slug}	h_{wall} [b]	h_{bath}	U
327	137	1560	96.4

[a] numerical values given in SI units: $\frac{\mathrm{W}}{\mathrm{m}^2\mathrm{K}}$

[b] thermal condunctance of the wall: $h_{wall} = 2k_w\left(d_1 \ln\frac{d_2}{d_1}\right)^{-1}$

Table 4.2: Optimal parameters for the four tank SFC calculated for approximate maximum and minimum values of growth kinetic parameters.[a]

	T_1	T_2	T_3	ℓ_1	ℓ_2	ℓ_3	ℓ_4	ℓ_{tot}	$S_{\max}$	C_f
Literature[b]	59.1	52.5	43.5	71.8	34.4	21.5	23.2	151	0.0279	0.0372
$g + 20\%$	58.6	51.5	42.5	169	70.4	34.1	77.4	351	0.0305	0.0370
$k_g + 20\%$	59.4	52.5	43.6	78.1	31.5	22.2	27.1	159	0.0268	0.0367
$k_g - 20\%$	58.9	52.1	43.0	81.3	37.0	20.5	29.3	166	0.0293	0.0371

[a] Parameter values are shown in °C for temperature, m for length, and g/g solvent for concentration.

[b] $g \approx 1.0$ (Jiang et al., 2012), so $g - 20\%$ is infeasible.

Table 4.3: Effect of using optimum calculated from literature values of growth parameters when the true system values are off by 20%.[a]

	$S_{\max}$	C_f
Literature[b]	0.0279	0.0372
$g + 20\%$	0.0446	0.0449
$k_g + 20\%$	0.0279	0.0368
$k_g - 20\%$	0.0316	0.0380

[a]Parameter values are shown in g/g solvent for concentration.

[b] $g \approx 1.0$ (Jiang et al.,2012), so $g - 20\%$ is infeasible.

Table 4.4: Optimal parameters for the shell-and-tube SFC for different values of ε_1 in Equation 4.36 and different numbers of heat exchangers, n. The range of values (in meters) for the lengths is [0, 300] and the range for the cooling water flowrate (in mg/s) is [0.001,50]. The data below are used to construct the Pareto optimality curve (Figure 4.12).

n	ε_1	ℓ_1	ℓ_2	ℓ_3	ℓ_4	$\dot{m}_{c,1}$	$\dot{m}_{c,2}$	$\dot{m}_{c,3}$	$\dot{m}_{c,4}$
1	0.01	300				0.001			
	0.1	300				0.001			
	0.18	300				0.001			
	0.19	300				34			
	0.2	300				35			
	0.25	300				40			
	0.5	300				50			
	1	300				50			
2	0.01	170	130			0.001	0.001		
	0.1	156	144			6	43		
	1	146	154			6	50		
	10	110	190			5	49		
	100	273	27			50	27		
3	0.01	300	0			0.001	0.001	0.001	
	0.1	153	96	51		4.3	17	49	
	0.5	161	130	9		6.9	49	1.4	
	1	154	136	10		6.6	50	3.9	
	10	144	134	22		7	50	48	
	100	273	12	15		50	48	46	
4	0.001	300	0	0	0	0.001	0.001	0.001	0.001
	0.01	119	53.4	62.4	65.2	2.91	4.28	13.3	50
	0.1	119	58.4	57.6	65.0	2.91	4.71	13.2	50
	1	139	73	75	13	12	49	15	50
	10	138	75	62	25	4	14	50	49

CHAPTER 5

DYNAMIC MODELING AND CONTROL OF MULTI-STAGE SLUG FLOW CRYSTALLIZATION

5.1 Introduction

For purification and separation of a high-value compound, continuous tubular crystallization shows great promise as a method that is both high-yield and easily scaled (Eder, et al., 2010; 2011; 2012; Alvarez & Myerson, 2010; Alvarez et al., 2011; Jiang et al., 2014). Additional motivation and a description of recent advances in continuous, tubular crystallization are introduced in Chapter 4 of this thesis. This chapter presents the first dynamic simulation of slug-flow crystallization for a series of counterflow, concentric shell-and-tube heat exchangers. Optimal design parameters for the simulation are investigated and model-based control strategies are developed and discussed.

5.2 Model and Solution Method

The development of a model for crystallization in slugs flowing in a series of counterflow, concentric, shell-and-tube heat exchangers begins with the population balance equation (PBE) (Hulburt & Katz, 1964; Randolph & Larson, 1988; Alvarez & Myerson, 2010),

$$\frac{\partial f(L,z,t)}{\partial t} + v_z \frac{\partial f(L,z,t)}{\partial z} + G(z,t)\frac{\partial f(L,z,t)}{\partial L} = 0 \tag{5.1}$$

$$f(L,0,t) = f_{in}(L,t) \tag{5.2}$$

$$f(0,z,t) = 0 \tag{5.3}$$

$$f(L,z,0) = f_0(L,z) \tag{5.4}$$

where L is the crystal size, z is the position along the tube, t is time, f is the crystal size distribution (CSD) in number of crystals per mass of solvent, v_z is the slug velocity, f_0 is the initial distribution, f_{in} is the distribution at the tube inlet, and G is the growth rate, which is commonly expressed as a function of supersaturation, S, (Jiang et al., 2012)

$$G(z,t) = k_g \left[S(z,t)\right]^g = k_g \left[C(z,t) - C_{sat}\left(T_h(z,t)\right)\right]^g \tag{5.5}$$

where k_g and g are fitting parameters that are determined from experimental data. The concentration of solute in the slug is C, and C_{sat} is the saturation curve which can be expressed as a polynomial function of tube-side temperature, T_h:

$$C_{sat} = a + b\left[T_h(z,t)\right] + c\left[T_h(z,t)\right]^2 \tag{5.6}$$

with parameters a, b, and c also determined from experimental data. A solute balance for this system is given by

$$\frac{\partial C(z,t)}{\partial t} = -v_z \frac{\partial C(z,t)}{\partial z} - \rho_c k_v \left(3G(z,t)\mu_2(z,t)\right) \tag{5.7}$$

$$C(0,t) = C_{in}(t) \tag{5.8}$$

$$C(z,0) = C_0(z) \tag{5.9}$$

where ρ_c is the crystal density, k_v is the volumetric shape factor, and μ_2 is the second order moment of the CSD where the *k*th order moment of a distribution is defined by

$$\mu_k(z,t) = \int_0^\infty f(L,z,t)L^k dL. \tag{5.10}$$

The energy balance for a single counterflow heat exchanger is given by (Bunce, 1995)

$$m_h C_{p,h} \frac{\partial T_h(z,t)}{\partial t} + \dot{m}_h C_{p,h} \ell \frac{\partial T_h(z,t)}{\partial z} + UA_{LM}\left(T_h(z,t) - T_c(z,t)\right) = 0 \tag{5.11}$$

$$m_c C_{p,c} \frac{\partial T_c(z,t)}{\partial t} - \dot{m}_c(t) C_{p,c} \ell \frac{\partial T_c(z,t)}{\partial z} - U A_{LM} \left(T_h(z,t) - T_c(z,t) \right) = 0 \tag{5.12}$$

$$T_h(0,t) = T_{h,in}(t) \tag{5.13}$$

$$T_h(z,0) = T_{h,0}(z) \tag{5.14}$$

$$T_c(\ell,t) = T_{c,in}(t) \tag{5.15}$$

$$T_c(z,0) = T_{c,0}(z) \tag{5.16}$$

where the subscripts h and c denote the hot stream of slugs in the tube and the cold stream of water in the shell respectively, m is the total mass, C_p is the constant pressure heat capacity, $\dot{m}$ is the mass flowrate, T is the average temperature, ℓ is the length of the heat exchanger, U is the overall heat transfer coefficient, and A_{LM} is the log-mean area for heat transfer given by

$$A_{LM} = \frac{A_h - A_c}{\ln\left(\frac{A_h}{A_c} \right)}. \tag{5.17}$$

The heat transfer coefficient, U, is defined as

$$\frac{1}{U} = \frac{1}{h_c} + \frac{d_1 \ln\left| d_2/d_1 \right|}{2k_w} + \frac{1}{h_h} \tag{5.18}$$

where d_1 is the inner pipe diameter, d_2 is the outer pipe diameter (and the inner shell diameter), and k_w is the thermal conductivity of the pipe material. The heat transfer coefficients for the hot and cold streams, h_h and h_c, respectively, are calculated from correlations for the Nusselt number, Nu. For heat transfer from the hot stream in the tube (Sieder & Tate, 1936),

$$\mathrm{Nu}_h = \frac{h_h d_1}{k_h} = 0.027\, \mathrm{Re}_h^{0.8}\, \mathrm{Pr}_h^{1/3} \left(\frac{\mu_h}{\mu_{h,d_1}} \right)^{0.14} \tag{5.19}$$

where k_h is the thermal conductivity of the fluid in the hot stream, μ_h is the dynamic viscosity in the bulk fluid of the slug, μ_{h,d_1} is the dynamic viscosity evaluated at the inner wall, Pr_h is the Prandtl number, and the Reynolds number for the hot stream, Re_h, is given by

$$\mathrm{Re}_h = \frac{\rho_h v_z d_1}{\mu_h} \tag{5.20}$$

where ρ_h is the density of the fluid forming the slugs. For heat transfer to the cold stream in the annulus (Dirker & Meyer, 2005),

$$\mathrm{Nu}_c = \frac{h_c D_H}{k_c} = K\,\mathrm{Re}_c^P\,\mathrm{Pr}_c^{1/3}\left(\frac{\mu_{c,d_2}}{\mu_{c,d_3}}\right)^{0.14} \tag{5.21}$$

where k_c is the thermal conductivity of the cold stream fluid, μ_{c,d_2} and μ_{c,d_3} are the dynamic viscosity of the cold stream fluid evaluated at the inner wall and outer wall of the annular region. D_H is the hydraulic diameter given by

$$D_H = d_3 - d_2. \tag{5.22}$$

The parameters K and P are given by the correlations

$$K = \frac{0.003 a_H^{1.86}}{0.063 a_H^3 - 0.674 a_H^2 + 2.225 a_H - 1.157} \tag{5.23}$$

$$P = 1.013 \exp\left(0.067 a_H\right) \tag{5.24}$$

where the annular diameter ratio, a_H, is

$$a_H = \frac{d_3}{d_2}. \tag{5.25}$$

The energy balance (5.11–5.12) can be applied to heat exchangers in series through the application of appropriate boundary conditions

$$T_{h,1}(0,t) = T_{h,in}(t) \tag{5.26}$$

$$T_{h,i}(0,t) = T_{h,i-1}(\ell_{i-1},t), \quad i = 2,\ldots,N_{HEX} \tag{5.27}$$

$$T_{c,i}(\ell_i,t) = T_{c,i,in}(t), \quad i = 1,\ldots,N_{HEX} \tag{5.28}$$

where N_{HEX} is the number of heat exchangers.

The method of moments is used to reduce the dimensionality of the PBE by converting Equations 5.1–5.4 to the system:

$$\frac{\partial \mu_k}{\partial t} = -v_z \frac{\partial \mu_k}{\partial z} + kG\mu_{k-1}, \quad k = 1,\ldots,\infty \tag{5.29}$$

$$\mu_k(0,t) = \mu_{k,in}(t), \quad k = 1,\ldots,\infty \tag{5.30}$$

$$\mu_k(z,0) = \mu_k^{ss}(z), \quad k = 1,\ldots,\infty \tag{5.31}$$

The method of lines with a finite difference approximation can then be used to convert equations 5.7, 5.11–5.12, and 5.29 to a system of $N(M+3)$ ordinary differential equations (ODEs), where M is the number of moments desired for calculation ($M \geq 2$) and

$$N = \sum_{i=1}^{N_{HEX}} N_i \tag{5.32}$$

where N_i is the number of discretization cells along the z-axis of heat exchanger i. The resulting system of ODEs is

$$
\begin{aligned}
&\frac{dC_{i,j}}{dt} = -v_z\left[\frac{C_{i,j}-C_{i,j-1}}{\Delta z}\right] - 3\rho_c k_v k_g\left[C_{i,j}-C_{\text{sat}}(T_{h,i,j})\right]^g \mu_{2,i,j}, && \begin{cases} j=1\ldots N_i \\ i=1\ldots N_{HEX} \end{cases} \\
&\frac{dT_{h,i,j}}{dt} = -\frac{\dot{m}_{h,i}\ell_i}{m_{h,i}}\left[\frac{T_{h,i,j}-T_{h,i,j-1}}{\Delta z}\right] - \frac{U_i A_{LM,i}}{m_{h,i}C_{p,h,i}}\left(T_{h,i,j}-T_{c,i,j}\right), && \begin{cases} j=1\ldots N_i \\ i=1\ldots N_{HEX} \end{cases} \\
&\frac{dT_{c,i,j}}{dt} = \frac{\dot{m}_{c,i}\ell_i}{m_{c,i}}\left[\frac{T_{c,i,j+1}-T_{c,i,j}}{\Delta z}\right] + \frac{U_i A_{LM,i}}{m_{c,i}C_{p,c,i}}\left(T_{h,i,j}-T_{c,i,j}\right), && \begin{cases} j=1\ldots N_i \\ i=1\ldots N_{HEX} \end{cases} \\
&\frac{d\mu_{k,j,i}}{dt} = -v_z\left[\frac{\mu_{k,i,j}-\mu_{k,i,j-1}}{\Delta z}\right] + kk_g\left[C_{i,j}-C_{\text{sat}}(T_{h,i,j})\right]^g \mu_{k-1,i,j}, && \begin{cases} j=1\ldots N_i \\ i=1\ldots N_{HEX} \\ k=1\ldots M \end{cases}
\end{aligned}
\tag{5.33}
$$

The system (5.33) is of the form

$$
\frac{d\boldsymbol{x}}{dt} = \boldsymbol{F}(\boldsymbol{x},\boldsymbol{u},\boldsymbol{d}) \tag{5.34}
$$

where the vectors $\boldsymbol{x}$, $\boldsymbol{u}$, and $\boldsymbol{d}$ are states, inputs, and disturbances, respectively, where

$$
\boldsymbol{x} = \begin{bmatrix} \boldsymbol{C} \\ \boldsymbol{T_h} \\ \boldsymbol{T_c} \\ \boldsymbol{\mu_0} \\ \vdots \\ \boldsymbol{\mu_M} \end{bmatrix} \in \mathbb{R}^{[N(M+3)]\times 1} \tag{5.35}
$$

$$
\boldsymbol{u} = \dot{\boldsymbol{m}}_{\boldsymbol{c}} \in \mathbb{R}^{N_{HEX}\times 1} \tag{5.36}
$$

$$
\boldsymbol{d} = \begin{bmatrix} C_0 \\ T_{h,0} \\ T_{c,\ell_1} \\ \vdots \\ T_{c,\ell_N} \\ \mu_{0,0} \\ \vdots \\ \mu_{M,0} \end{bmatrix} \in \mathbb{R}^{(M+6)\times 1} \tag{5.37}
$$

The initial condition for the model can be written

$$\boldsymbol{x}(0) = \boldsymbol{x}_0 . \tag{5.38}$$

Measured output variables are the temperature and concentration at the exits,

$$\boldsymbol{y}_m = \begin{bmatrix} C_1 \\ \vdots \\ C_N \\ T_{h,1} \\ \vdots \\ T_{h,N} \end{bmatrix} \in \mathbb{R}^{8\times 1}. \tag{5.39}$$

The system is to be designed so that, under normal operating conditions, the temperature drop in each heat exchanger produces an environment to minimize the maximum supersaturation, to promote molecular purity; i.e.,

$$\begin{aligned} &\min_{\theta}\left[\varepsilon_1 S_{\max} + \varepsilon_2 \max\left\{ C_f - [C_{sat}(T_{c,in}) + \varepsilon_3], 0 \right\} \right] \\ &0 < \ell_i \le \ell_{total}, \; i = 1 \ldots n \\ &\ell_n = \ell_{total} - \sum_{i}^{n-1} \ell_i \\ &0 < \dot{m}_{c,i} \le \dot{m}_{c,\max}, \; i = 1 \ldots n \\ &T_{c,in,n} = T_{\min} \\ &T_{c,in,i-1} \ge T_{c,in,i} \ge T_{c,in,i+1}, \; i = 1 \ldots n-1 \end{aligned} \quad , \tag{5.40}$$

where ε_1 and ε_2 are chosen to obtain the desired tradeoff between yield and maximum allowable supersaturation, and ε_3 is a small added value to reflect the diminishing returns on approach to the solubility limit. The parameters, θ, are given by

$$\theta = \begin{bmatrix} \ell_1 & \ell_2 & \ell_3 & \dot{m}_{c,1} & \dot{m}_{c,2} & \dot{m}_{c,3} & \dot{m}_{c,4} & T_{c,in,1} & T_{c,in,2} & T_{c,in,3} \end{bmatrix}^{\mathrm{T}}. \tag{5.41}$$

The optimization (Equation 5.40) was solved using the revised Nelder-Mead simplex algorithm, fminsearchbnd.m (Nelder & Mead, 1965; D'Errico, 2006) in MATLAB version 7.11.0.584.

Operating so that the exit concentration, C_N, is near the minimum concentration, $C_{sat}(T_{c,in})$, provides the desired yield. The optimal crystal size is specified by the upstream nucleation rate. Excessive length of the tubes should be avoided, as that would introduce an undesirable time delay in the process dynamics. The control objective is to minimize the maximum supersaturation in the system by manipulating the flowrate of cooling water in each heat exchanger to reject nonidealities caused by disturbances.

5.3 Results and Discussion

Profiles for the optimized steady-state four-stage slug-flow crystallizer are shown in Figures 5.1–5.3. The optimal design parameters are given in Table 5.1. As expected, the supersaturation quickly reaches the minimized maximum value, and returns to that maximum once in each heat exchanger. The drop in supersaturation near the outlet is also quick.

Investigating the response of the process, initially at steady state, to disturbances, manipulations, and uncertainties provides a great deal of information and insight not available from steady-state models. Figures 5.4–5.31 provide insight into the dynamics of the slug-flow crystallizer, by showing how various process outputs (both measured and calculated) are affected by a step change in manipulated, disturbance, and parameter variables. The output described in Figures 5.4-5.31 is normalized according to

$$\frac{2y-(y_{\max}+y_{\min})}{y_{\max}-y_{\min}} \tag{5.42}$$

Figures 5.4–5.7 illustrate the outlet concentration of the slug stream for heat exchangers 1–4, respectively, when subjected to the step inputs described in Table 5.2; step inputs are also normalized in the way described by Equation 5.42. The downstream process inputs show no

effect on upstream concentrations. The outlet concentrations are seen to be highly sensitive to cooling water temperatures and growth kinetics parameters. The cooling water flowrate displays moderate utility. Increasing the cooling water flowrate or decreasing the cooling water temperature decrease the exit concentration and vice versa. Figure 5.7 shows that the effect of most input disturbances on concentration are dampened by the process design automatically.

Figures 5.8–5.11 display the average particle size at the exit of each heat exchanger under the same step inputs as in Figures 5.4–5.7. The largest responses in particle size are caused by disturbances in inlet concentration or inlet cooling water temperature and uncertainty in growth kinetics parameters. Moderate effects are caused by cooling water flowrate and inlet slug stream temperature. Downstream process inputs do not affect upstream average particle size. Figure 5.11 shows that the effects of most disturbances are dampened by the process automatically (aside from a step in inlet concentration which would add more material (solute) for removal).

The response of the coefficient of variance at the exit of each heat exchanger is included in Figures 5.12–5.15 for completeness, but is not observed to respond cleanly and is believed by many to not be a useful variable for process design or control (see Bronk, 1979 and included references).

Figures 5.16–5.19 and 5.20–5.23 show the responses of the maximum supersaturation and average supersaturation, respectively, within each heat exchanger. Supersaturation is of vital importance as the driving force for growth as well as nucleation. While this system is designed to minimize secondary nucleation due to attrition, supersaturation levels must be kept under control to avoid the incorporation of impurities into the crystalline matrix. Cooling water temperature and flowrate are seen to have a large effect locally. Inlet conditions for the slug stream have a

decreasing effect with each subsequent heat exchanger. Persistent sources of relatively large deviation are again the growth kinetics parameters.

Figures 5.24–5.27 illustrate the response of yield at the exit of each heat exchanger. All effects of disturbances and process inputs on yield are dampened by the process design, except for the cooling water temperature of the fourth heat exchanger and large uncertainty in the growth kinetics parameters. Values of yield greater than 100% are a result of calculating the yield (for comparison purposes) by (Skogestad & Postlethwaite, 2005).

$$y_i = \frac{C_i - C_{sat}(T_{c0,4,nom})}{C_{in,nom} - C_{sat}(T_{c0,4,nom})} 100\% \tag{5.43}$$

Figures 5.28–5.31 display the effect of input step changes on the slug stream temperatures at the exit of each heat exchanger. Temperature comparisons are valuable due to the relative ease and accuracy at which temperature can be measured. Not surprisingly, the greatest effect by far on the outlet slug stream temperature is the temperature of the cooling water.

5.4 Conclusions

Manipulating only the cooling water flowrates will be insufficient to reject process disturbances that result from the departure of growth kinetics parameters from nominal values. Additionally, without a tight control of the inlet temperature of cooling water, manipulation of the cooling water flowrates will be insufficient to suppress that resulting deviation as well. Changes in the inlet temperature and concentration for the slug stream are less problematic; the system design is inherently robust to disturbances which occur far upstream. The robustness allows the on-line measurement of particle size, a relatively expensive and inaccurate endeavor,

to be eliminated from the design of a control algorithm; particle size is not observed to be affected greatly by upstream disturbances.

In an effort to increase the output response to changes in manipulated variables, the cooling water inlet temperature should be converted from a disturbance to a manipulated variable. The extra degrees of freedom from controlling not only the cooling water flowrates, but also the cooling water temperature, possibly over a larger range than that shown in Table 5.2, will boost the controllability of the process. From a design standpoint, the addition of extra tubing length will also serve as a buffer to disturbances.

Figures 5.32-5.34 describe potential control diagrams for the multi-variable control of the slug flow crystallizer. Neglecting particle size measurements for the reasons mentioned above, there are two measurements of interest that can be taken at the outlet of each heat exchanger: temperature and solute concentration. There are also two manipulated variables for each heat exchanger: cooling water flowrate and cooling water temperature (Figure 5.32). A variety of factors must be considered in selecting the best control algorithm in terms of the number of measurements, number of controllers, and which controllers receive which measurements (and control which manipulated variables). Of the eight possible measurements, the four temperature measurements are cheap and accurate while four measurements of solute concentration would be relatively expensive and difficult. The design of this process does not provide evidence that intermediate solute concentration measurements would be useful elements of process control, and it is unlikely that the final algorithm or real-world design would contain those measurements. With respect to the eight manipulated variables, the inlet temperature of cooling water could be altered by applying energy to a thermal bath or, perhaps more likely, combining multiple feeds from multiple baths at Y-mixers. The cooling water temperature displays a greater

effect on process dynamics than the cooling water flowrate, but incompressible fluid flowrates have the advantage of being easily and quickly controlled.

The simplest design would just involve temperature measurements and temperature manipulations (Figure 5.33) to maintain the desired supersaturation within the four heat exchangers, and trust in the process design to attain the desired yield, but a final solute concentration measurement—in addition to temperature—would probably be unavoidable for the sake of assurances with respect to the target yield. Flowrate manipulations will also likely play a part in an effort to speed up dynamic response and add to the magnitude of the controlling action (Figure 5.34). Controllability may be increased even further by providing downstream controllers with upstream measurements. Further computational analysis will help to determine the optimal design.

5.5 Figures

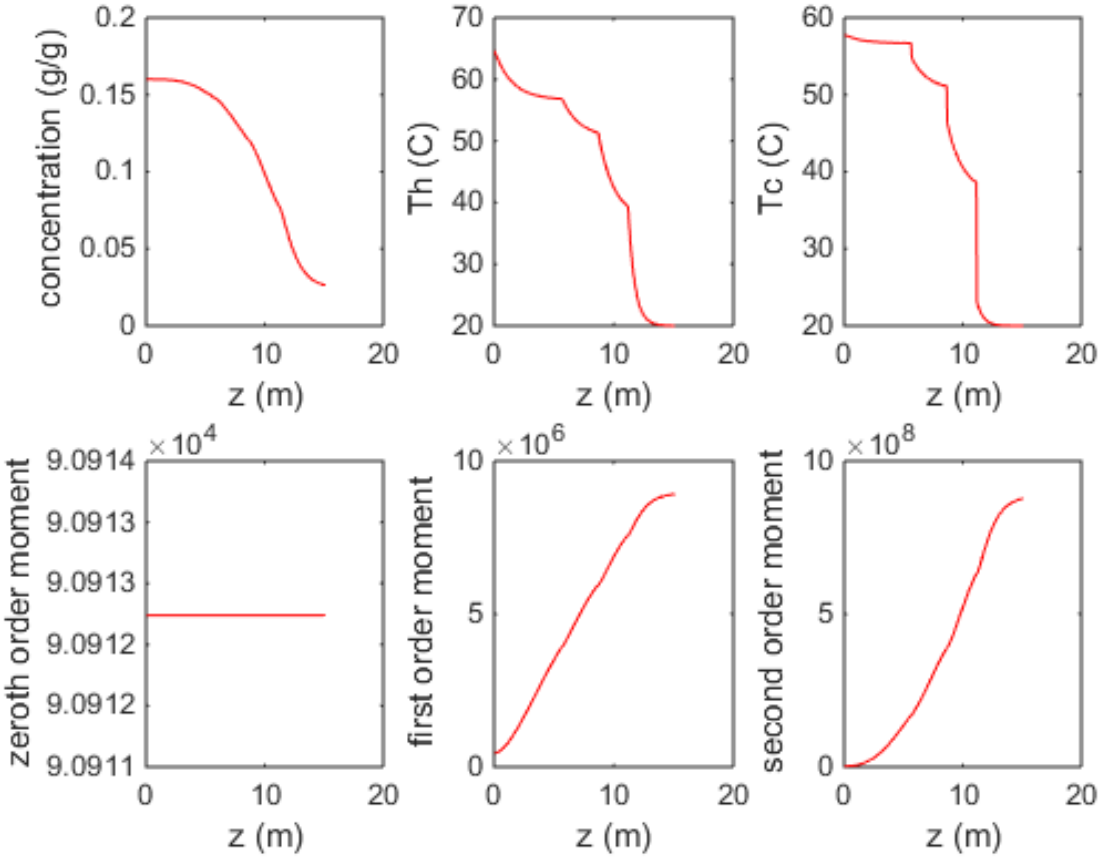

Figure 5.1: Steady-state operating profiles for the slug-flow crystallizer with the design variables given by Table 5.1. The trends in concentration and temperature across the system are a gradual decline that becomes more drastic as crystal size increases. The temperature of the hot stream (top-center plot) also drops sharply immediately to create the driving force for growth.

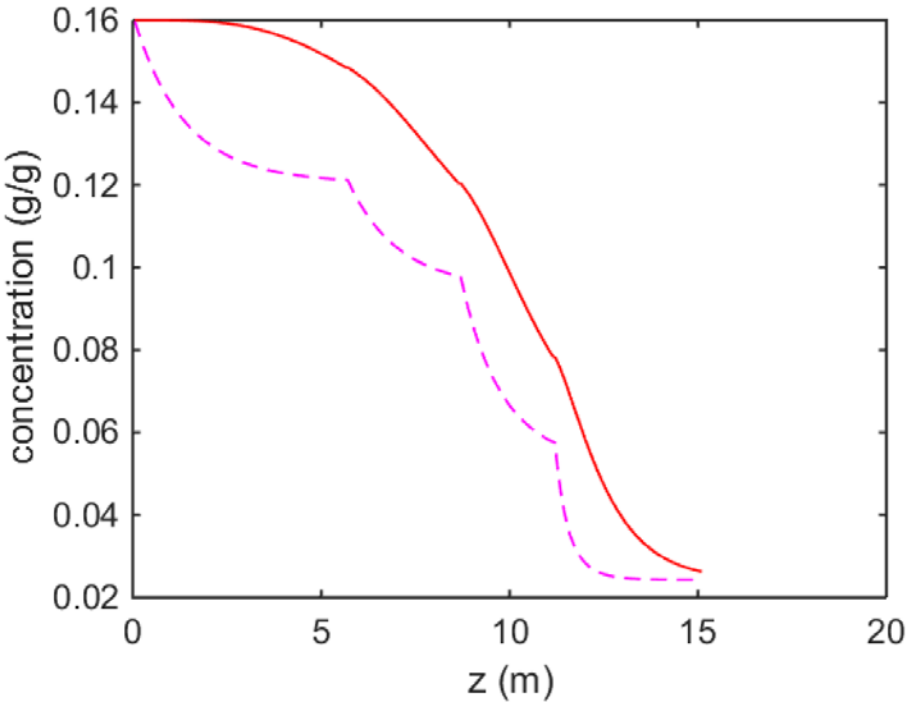

Figure 5.2: Solute concentration (—) and saturated concentration (- -) profiles are shown together for comparison. The driving force for crystal growth in this system, i.e., $G = k_g \left[C(z) - C_{sat}(z) \right]^g$, $g = 1.0$, is given by the difference of these two plots. At steady-state, the yield and average particle size are specified by the area between these two curves.

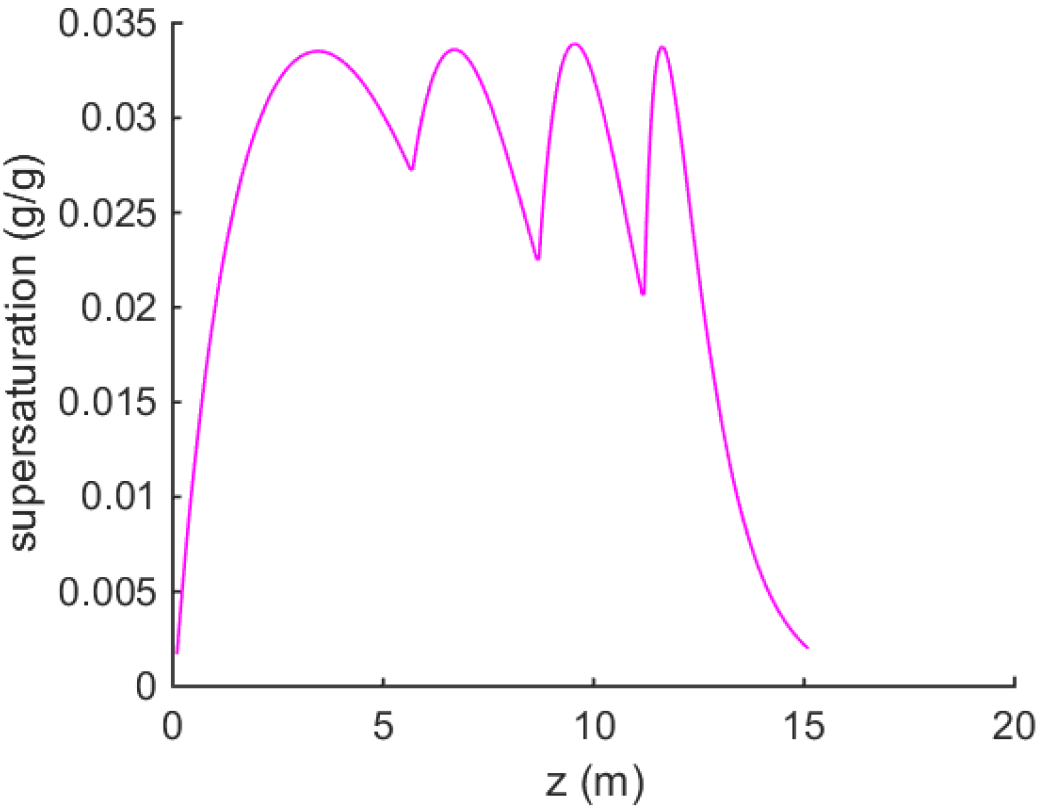

Figure 5.3: Optimal supersaturation profile under steady conditions in the slug-flow crystallizer, specified by Table 5.1. Four rounded peaks – one per heat exchanger – can be observed to have equal height. The final peak decays to nearly zero, as the yield is maximized given the system constraints.

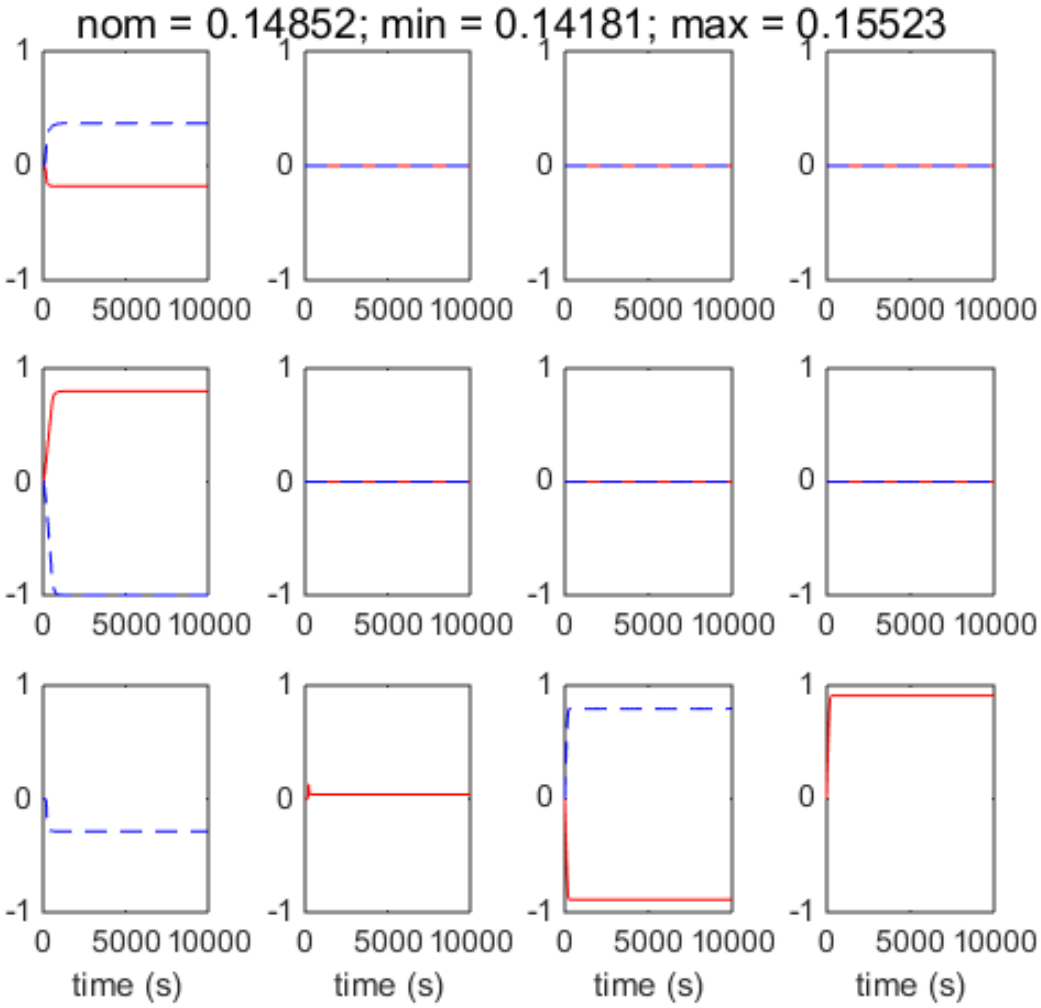

Figure 5.4: The normalized response of the solute concentration at the exit of the first heat exchanger to step changes up (—) and down (- -) in the mass flow rate of cooling water for heat exchangers 1–4 (row 1), the inlet temperature of the cooling water for heat exchangers 1–4 (row 2), and the inlet slug stream temperature, inlet solute concentration, growth prefactor, and growth exponent (row 3, left to right). See Table 5.2 for input ranges.

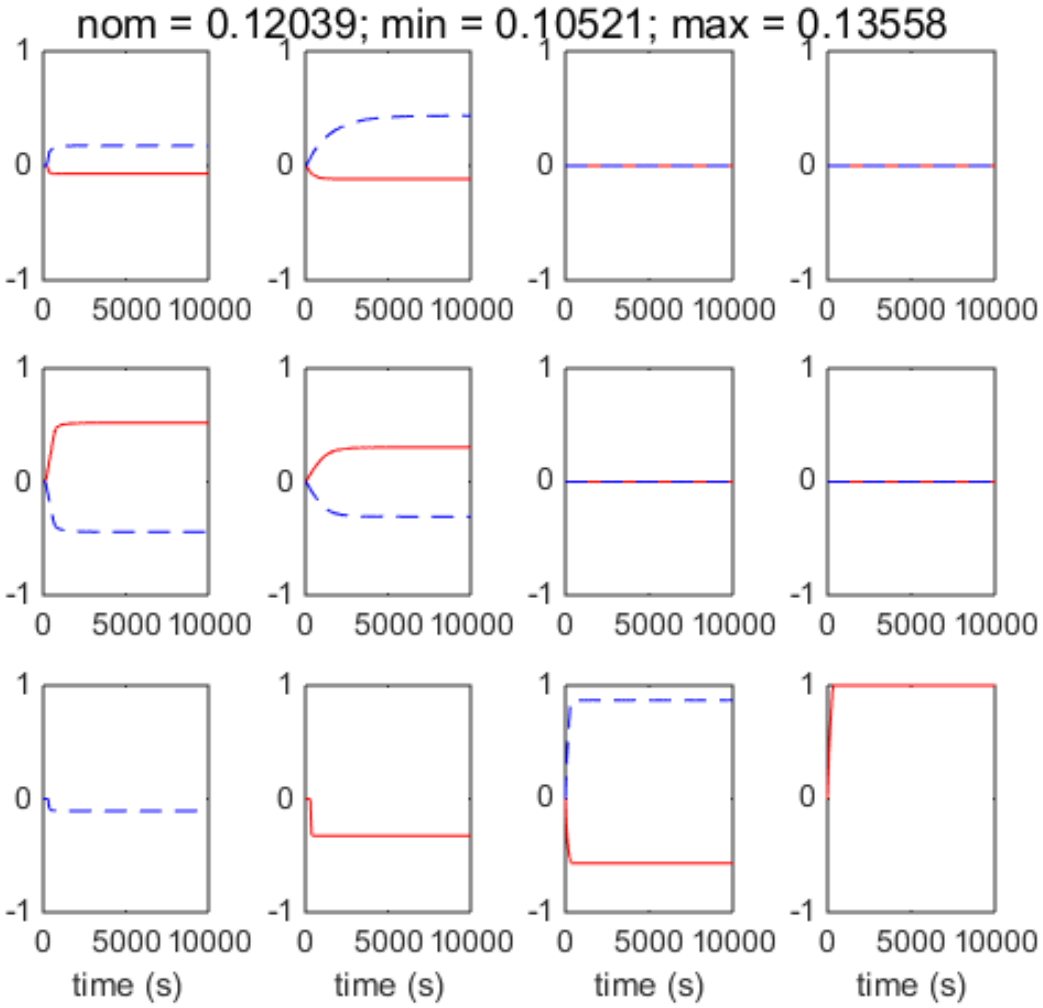

Figure 5.5: The normalized response of the solute concentration at the exit of the second heat exchanger to step changes up (—) and down (- -) in the mass flow rate of cooling water for heat exchangers 1–4 (row 1), the inlet temperature of cooling water for heat exchangers 1–4 (row 2), and the slug stream temperature, concentration, growth prefactor, and growth exponent (row 3, left to right). See Table 5.2 for input ranges.

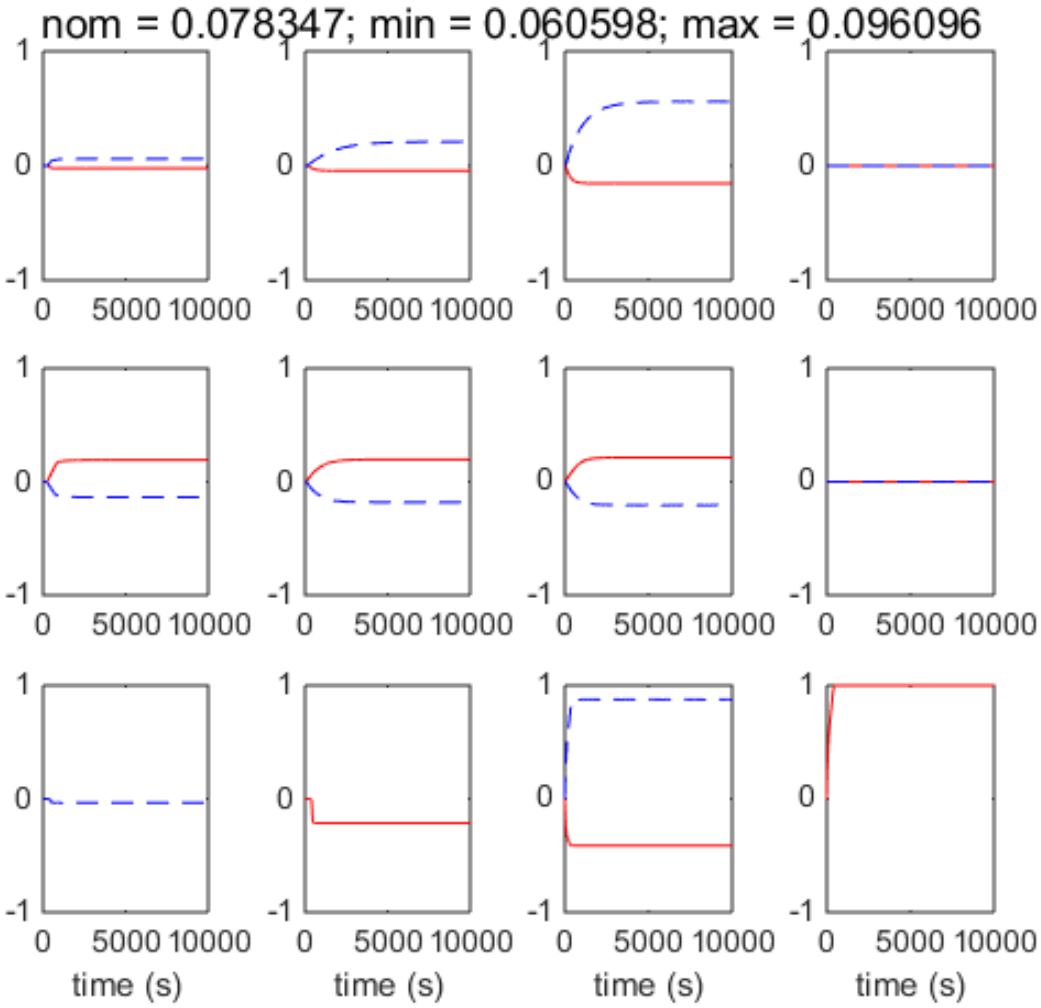

Figure 5.6: The normalized response of the solute concentration at the exit of the third heat exchanger to step changes up (—) and down (- -) in the mass flow rate of cooling water for heat exchangers 1–4 (row 1), the inlet temperature of cooling water for heat exchangers 1–4 (row 2), and the slug stream temperature, concentration, growth prefactor, and growth exponent (row 3, left to right). See Table 5.2 for input ranges.

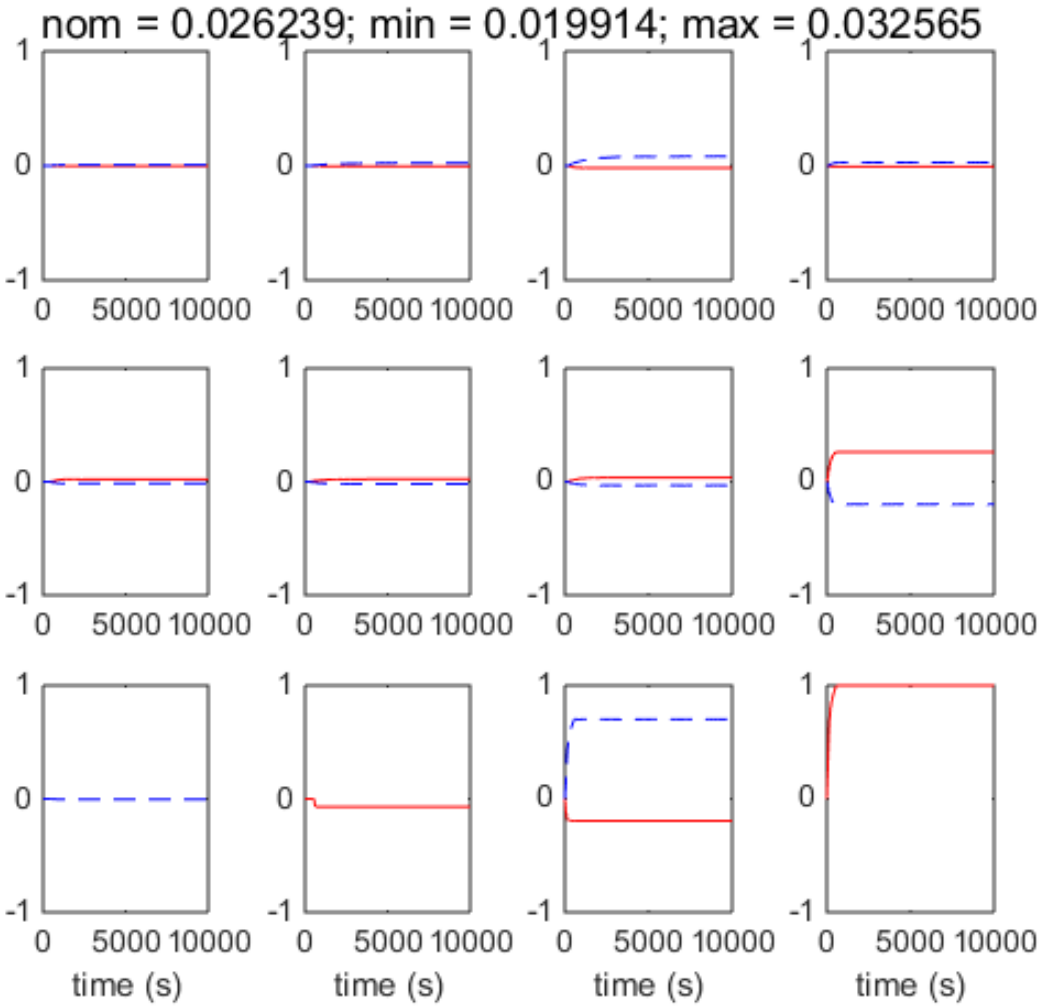

Figure 5.7: The normalized response of the solute concentration at the exit of the fourth heat exchanger to step changes up (—) and down (- -) in the mass flow rate of cooling water for heat exchangers 1–4 (row 1), the inlet temperature of cooling water for heat exchangers 1–4 (row 2), and the slug stream temperature, concentration, growth prefactor, and growth exponent (row 3, left to right). See Table 5.2 for input ranges.

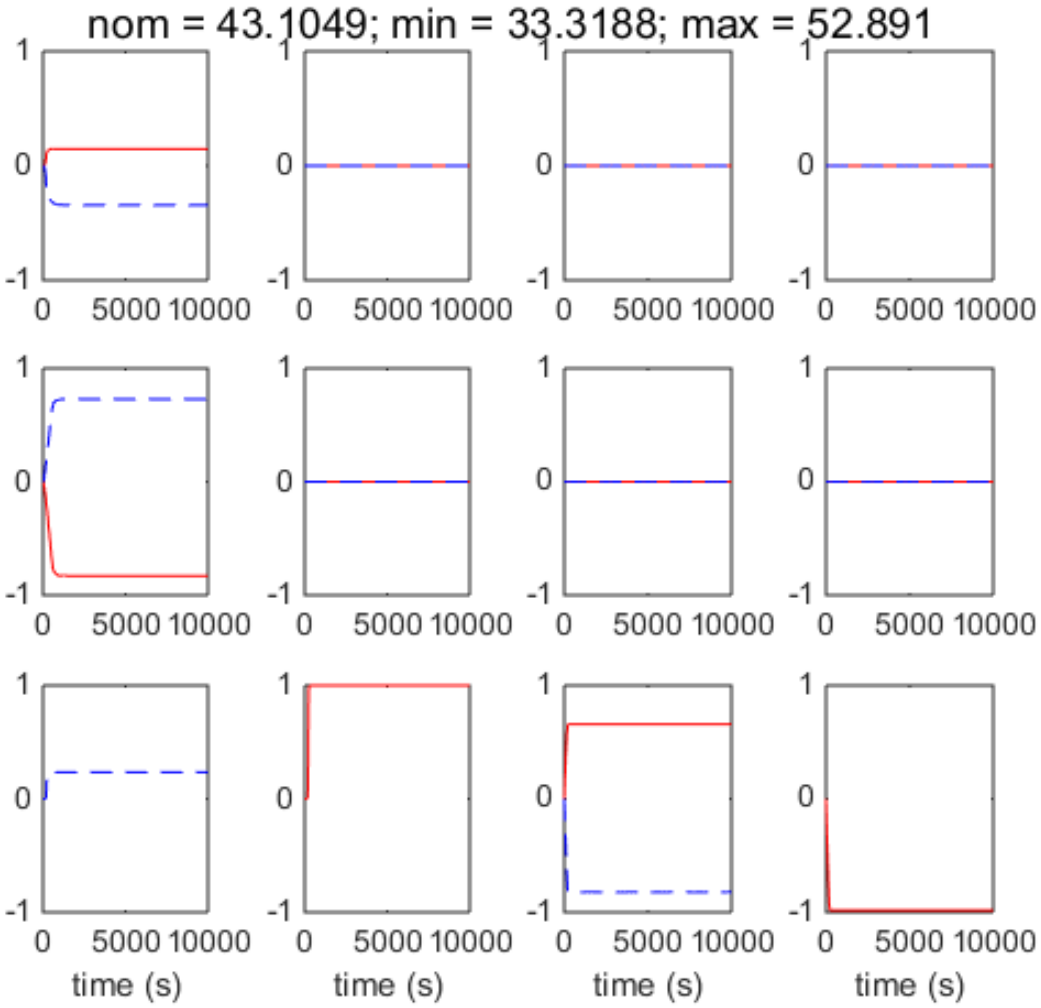

Figure 5.8: The normalized response of the average particle size at the exit of the first heat exchanger to step changes up (—) and down (- -) in the mass flow rate of cooling water for heat exchangers 1–4 (row 1), the inlet temperature of cooling water for heat exchangers 1–4 (row 2), and the slug stream temperature, concentration, growth prefactor, and growth exponent (row 3, left to right). See Table 5.2 for input ranges.

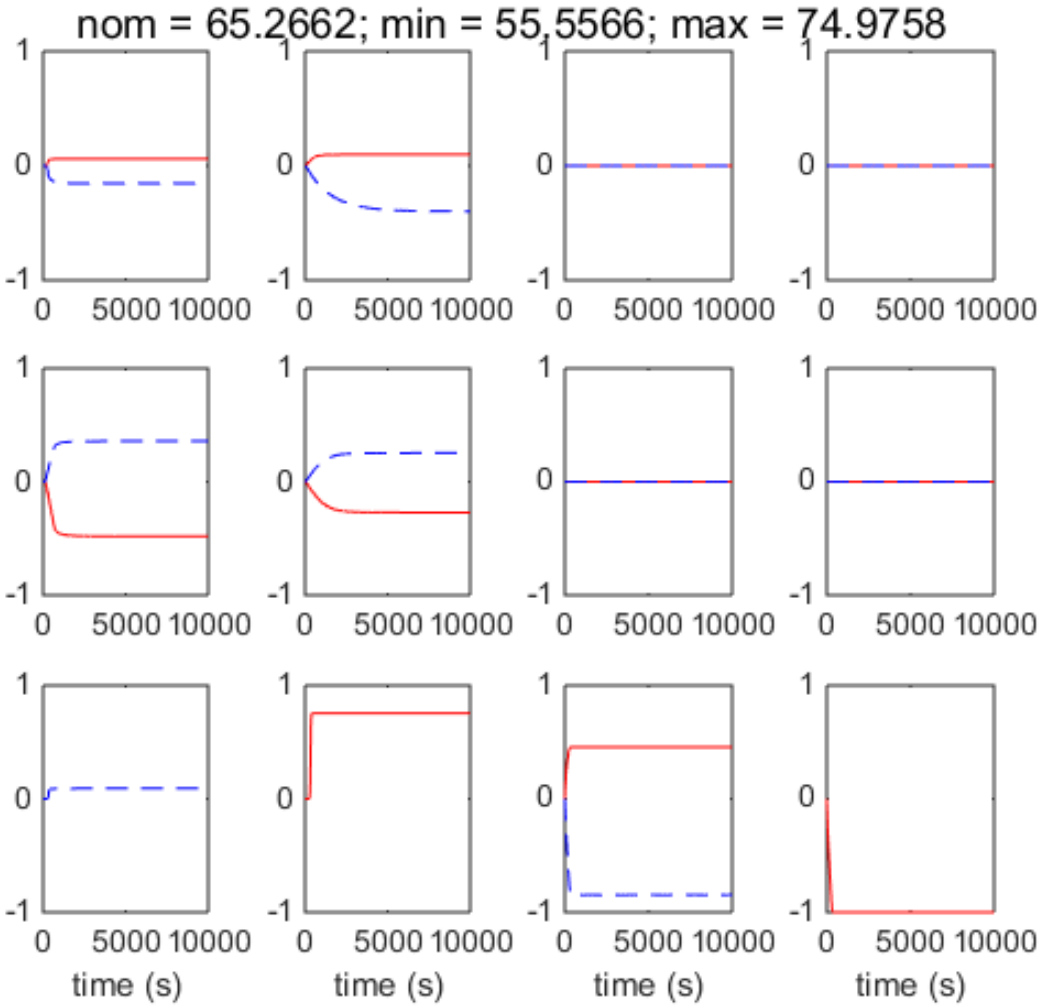

Figure 5.9: The normalized response of the average particle size at the exit of the second heat exchanger to step changes up (—) and down (- -) in the mass flow rate of cooling water for heat exchangers 1–4 (row 1), the inlet temperature of cooling water for heat exchangers 1–4 (row 2), and the slug stream temperature, concentration, growth prefactor, and growth exponent (row 3, left to right). See Table 5.2 for input ranges.

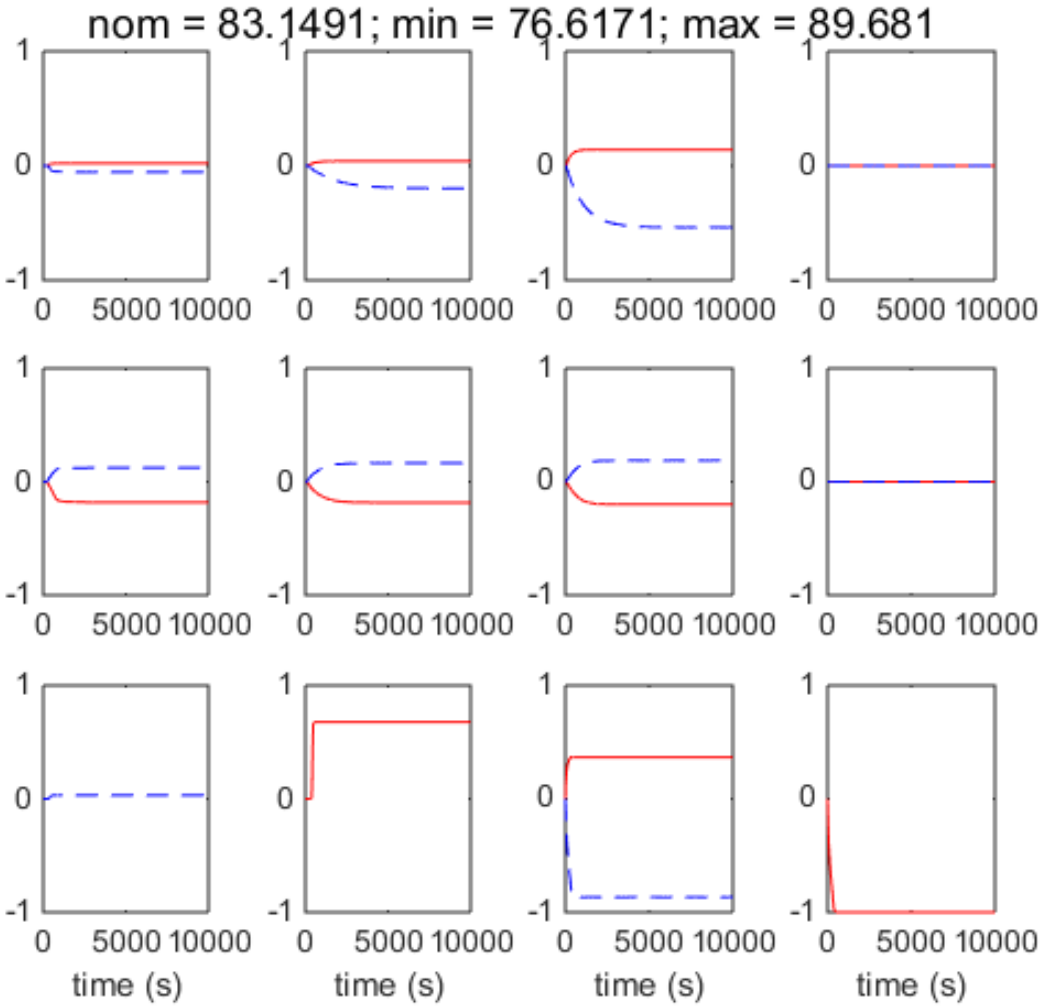

Figure 5.10: The normalized response of the average particle size at the exit of the third heat exchanger to step changes up (—) and down (- -) in the mass flow rate of cooling water for heat exchangers 1–4 (row 1), the inlet temperature of cooling water for heat exchangers 1–4 (row 2), and the slug stream temperature, concentration, growth prefactor, and growth exponent (row 3, left to right). See Table 5.2 for input ranges.

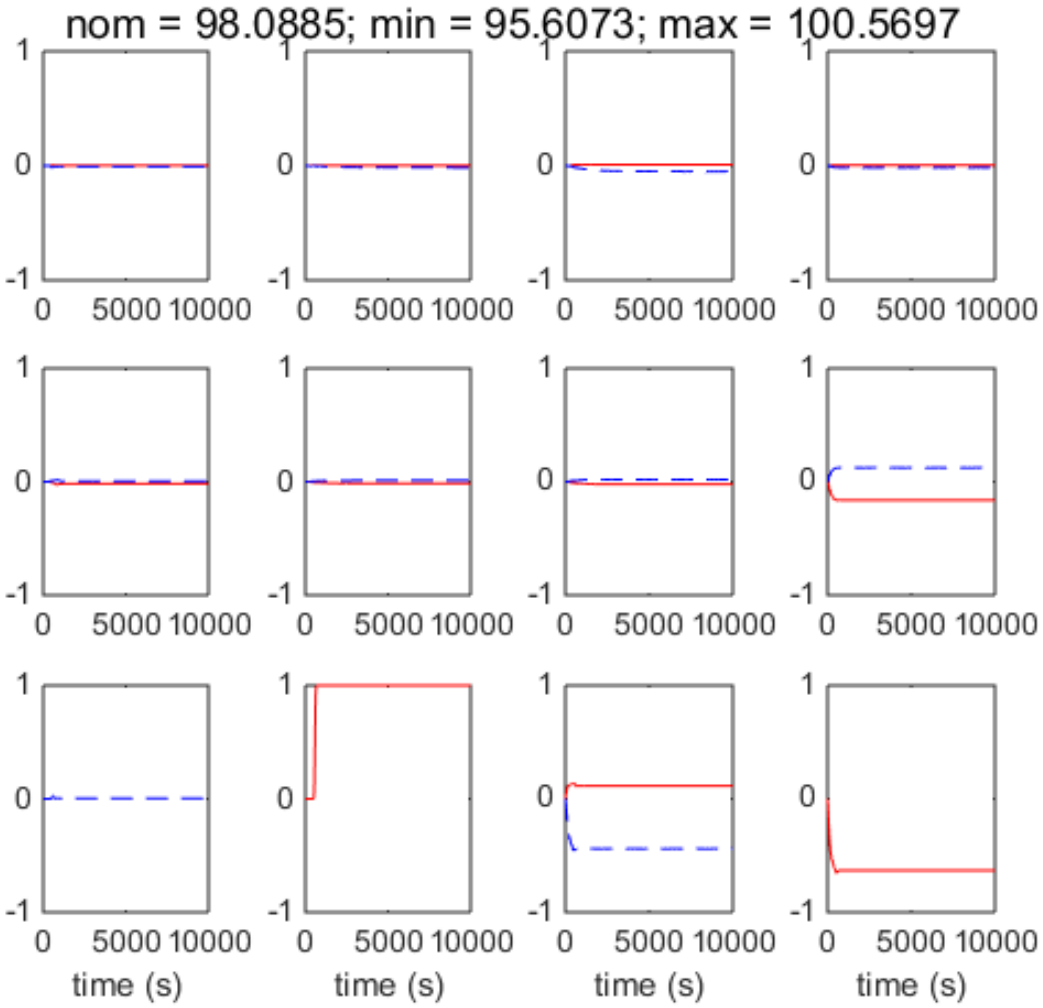

Figure 5.11: The normalized response of average particle size at the exit of the fourth heat exchanger to step changes up (—) and down (- -) in the mass flow rate of cooling water for heat exchangers 1–4 (row 1), the inlet temperature of cooling water for heat exchangers 1–4 (row 2), and the slug stream temperature, solute concentration, growth prefactor, and growth exponent (row 3, left to right). See Table 5.2 for input ranges.

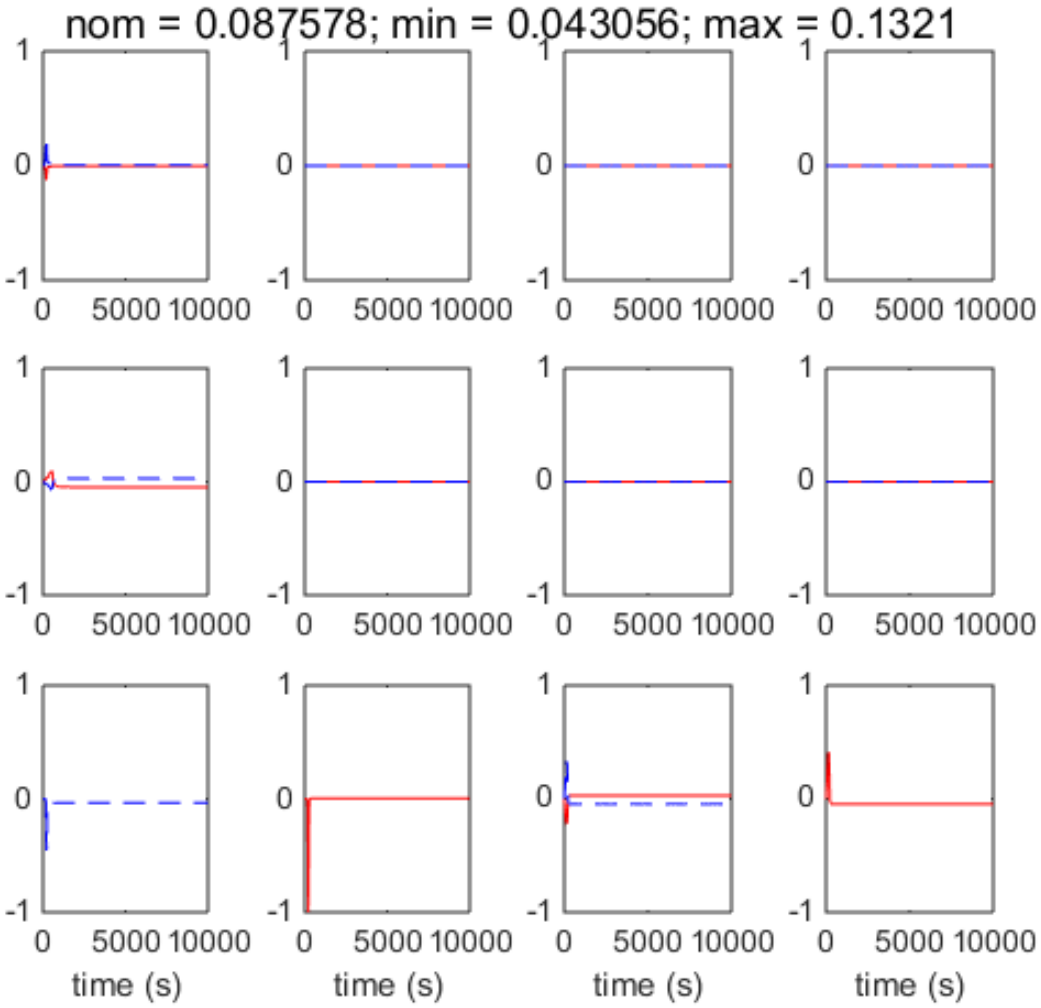

Figure 5.12: The normalized response of the coefficient of variance at the exit of the first heat exchanger to step changes up (—) and down (- -) in the mass flow rate of cooling water for heat exchangers 1–4 (row 1), the inlet temperature of cooling water for heat exchangers 1–4 (row 2), and the slug stream temperature, concentration, growth prefactor, and growth exponent (row 3, left to right). See Table 5.2 for input ranges.

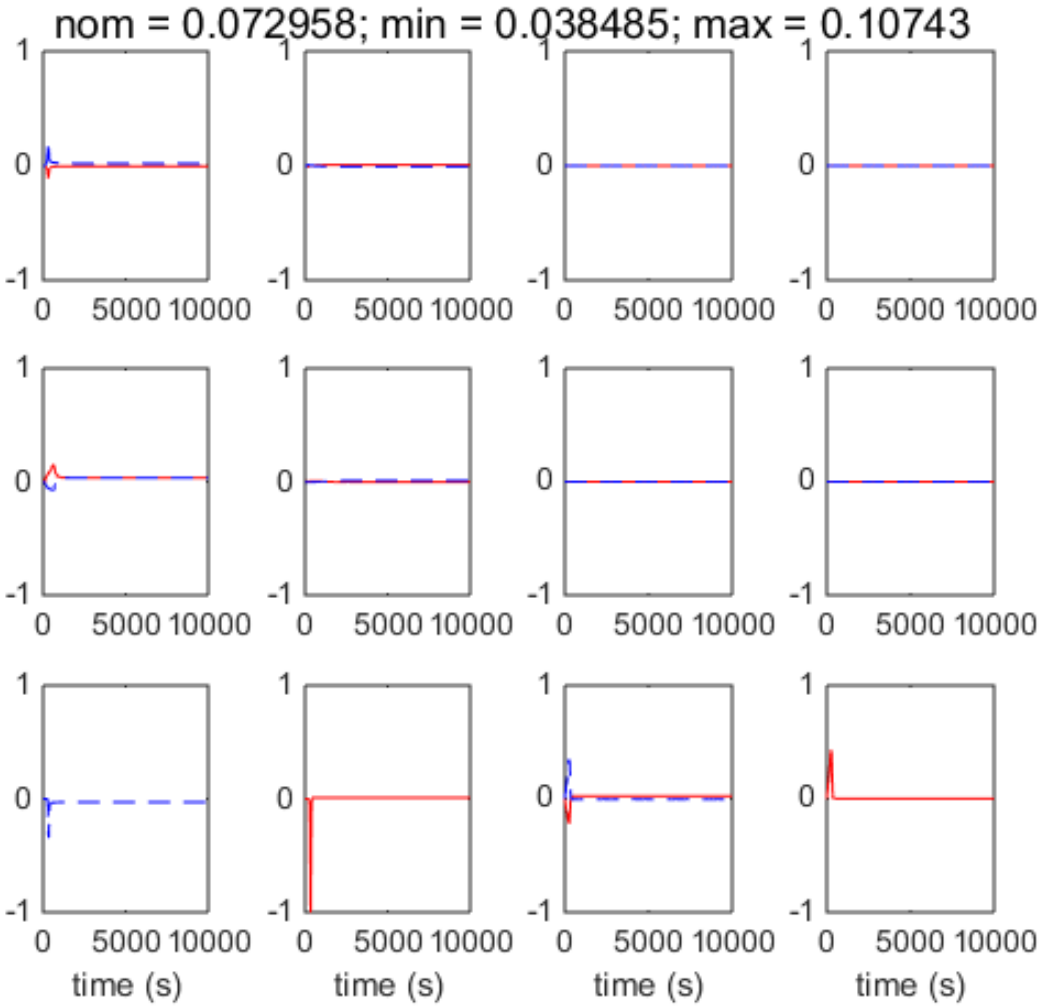

Figure 5.13: The normalized response of the coefficient of variance at the exit of the second heat exchanger to step changes up (—) and down (- -) in the mass flow rate of cooling water for heat exchangers 1–4 (row 1), the inlet temperature of cooling water for heat exchangers 1–4 (row 2), and the slug stream temperature, solute concentration, growth prefactor, and growth exponent (row 3, left to right). See Table 5.2 for input ranges.

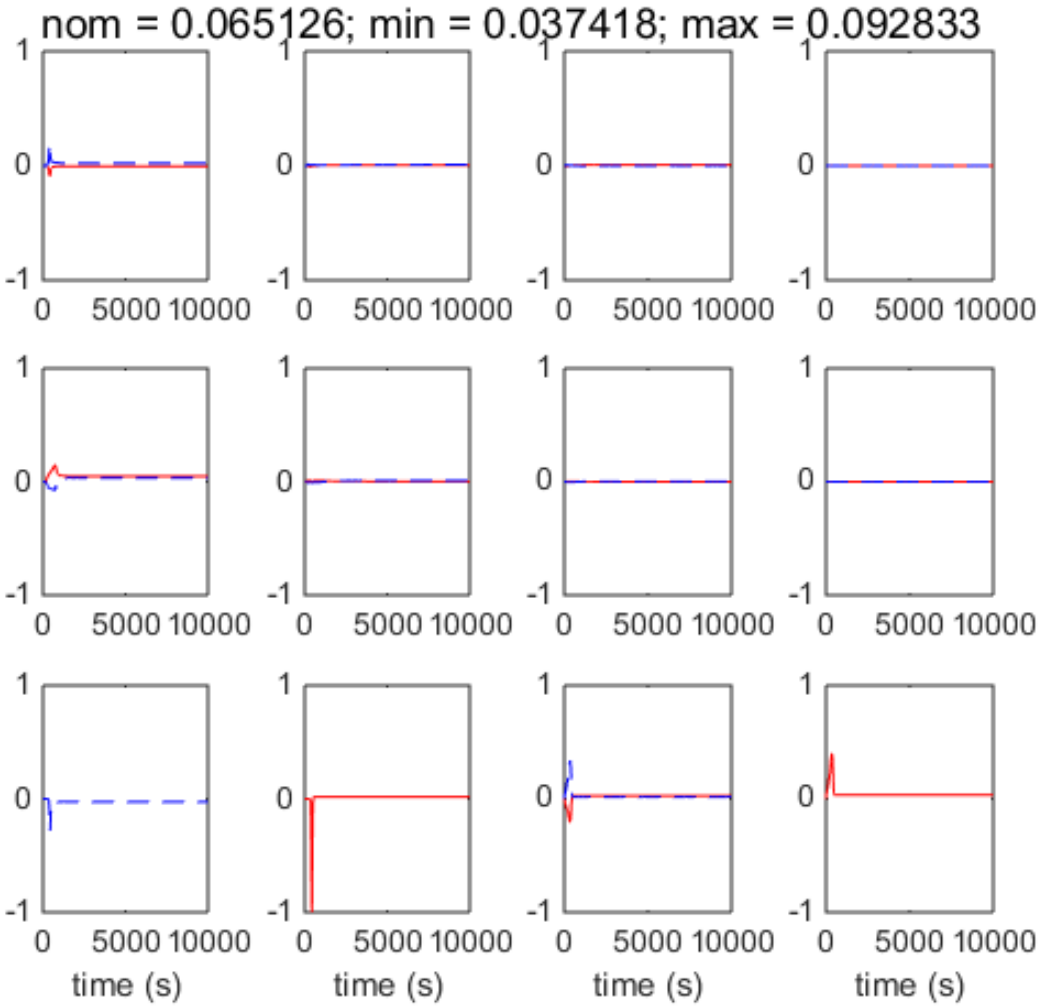

Figure 5.14: The normalized response of the coefficient of variance at the exit of the third heat exchanger to step changes up (—) and down (- -) in the mass flow rate of cooling water for heat exchangers 1–4 (row 1), the inlet temperature of cooling water for heat exchangers 1–4 (row 2), and the slug stream temperature, solute concentration, growth prefactor, and growth exponent (row 3, left to right). See Table 5.2 for input ranges.

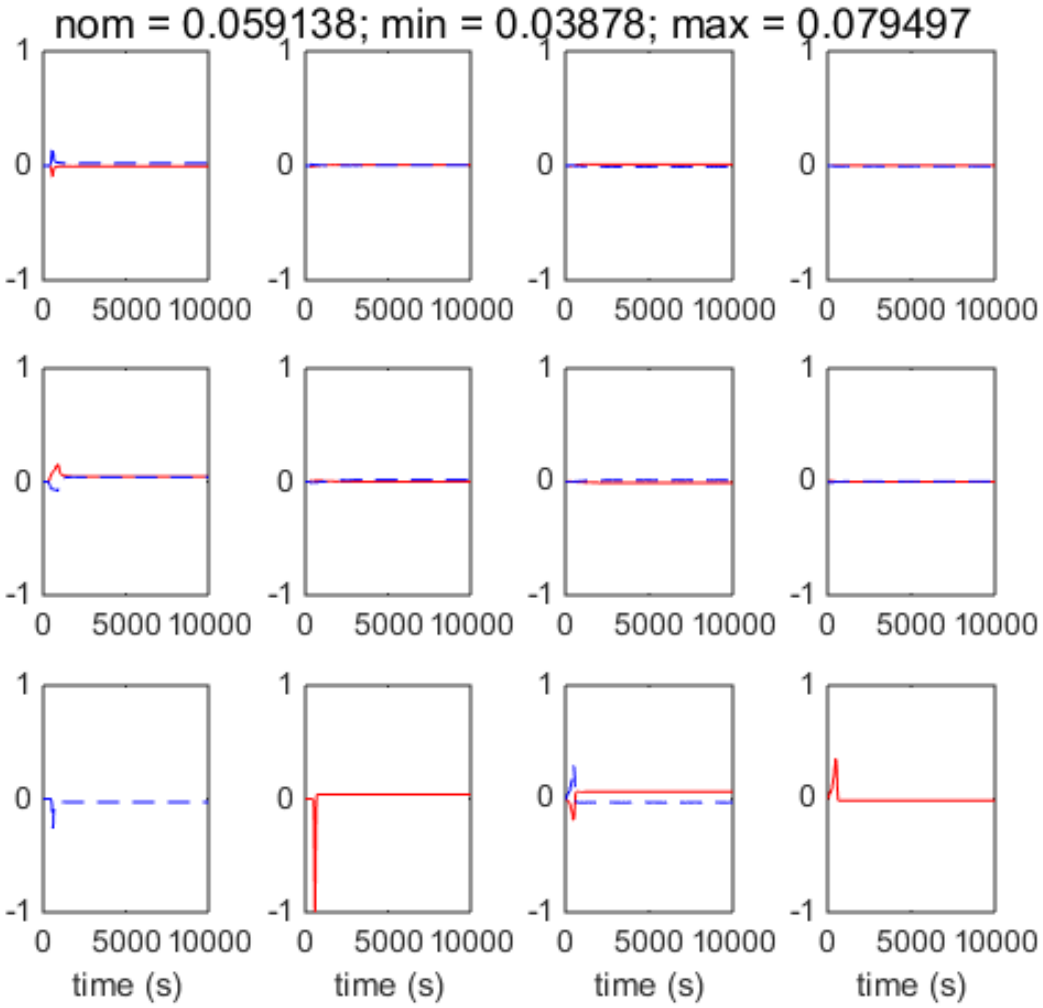

Figure 5.15: The normalized response of coefficient of variance at the exit of the fourth heat exchanger to step changes up (—) and down (- -) in mass flow rate of cooling water for heat exchangers 1–4 (row 1), inlet temperature of cooling water for heat exchangers 1–4 (row 2), and slug stream temperature, concentration, growth prefactor, and growth exponent (row 3, left to right). See Table 5.2 for input ranges.

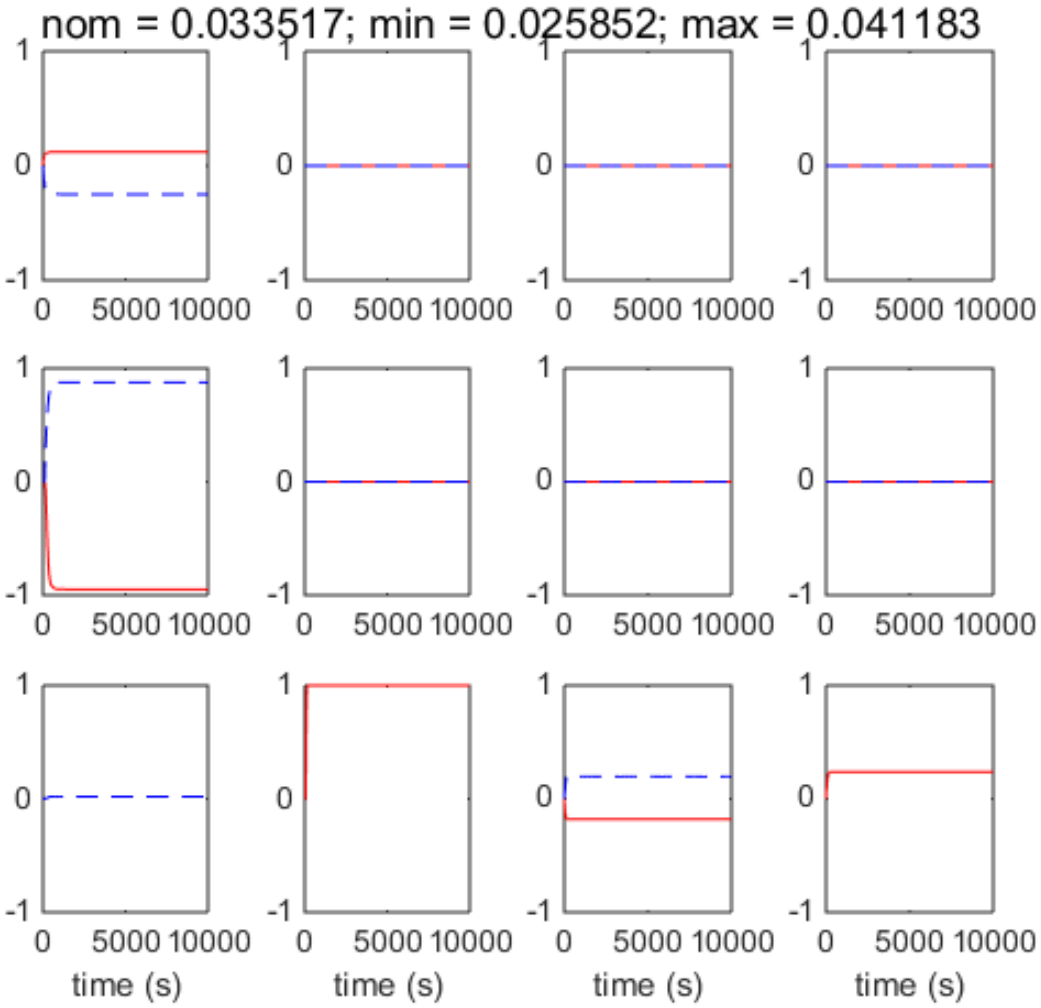

Figure 5.16: The normalized response of the maximum supersaturation within the first heat exchanger to step changes up (—) and down (- -) in mass flow rate of cooling water for heat exchangers 1–4 (row 1), the inlet temperature of cooling water for heat exchangers 1–4 (row 2), and the slug stream temperature, solute concentration, growth prefactor, and growth exponent (row 3, left to right). See Table 5.2 for input ranges.

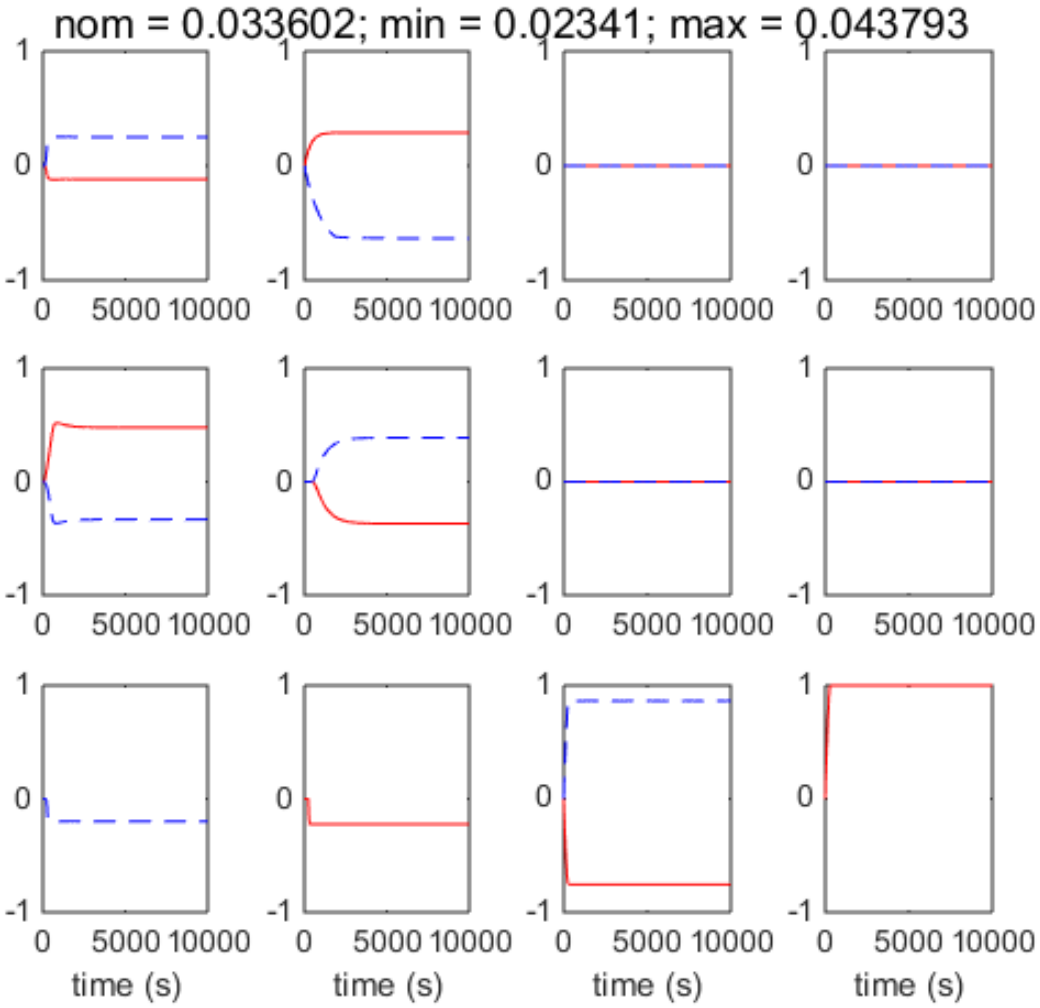

Figure 5.17: The normalized response of the maximum supersaturation within the second heat exchanger to step changes up (—) and down (- -) in the mass flow rate of cooling water for heat exchangers 1–4 (row 1), the inlet temperature of cooling water for heat exchangers 1–4 (row 2), and the slug stream temperature, concentration, growth prefactor, and growth exponent (row 3, left to right). See Table 5.2 for input ranges.

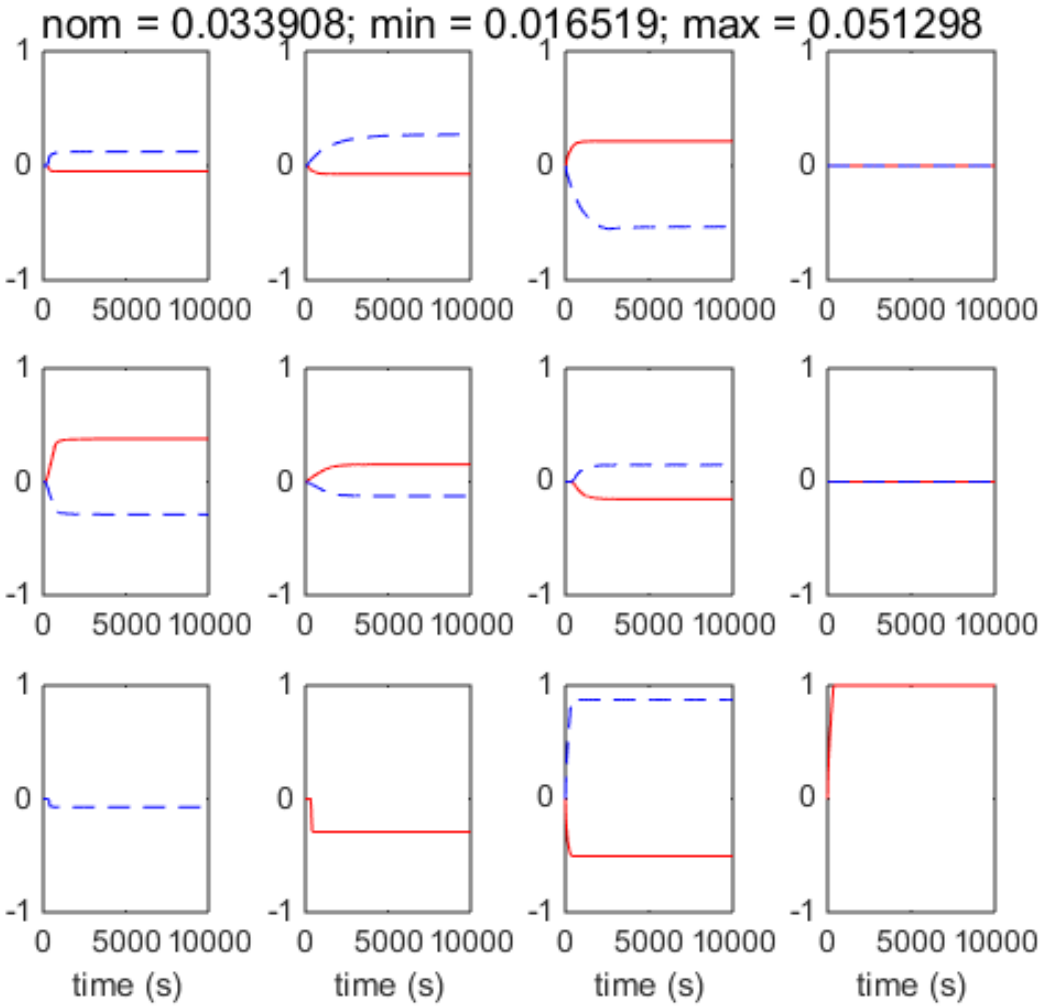

Figure 5.18: The normalized response of the maximum supersaturation within the third heat exchanger to step changes up (—) and down (- -) in the mass flow rate of cooling water for heat exchangers 1–4 (row 1), the inlet temperature of cooling water for heat exchangers 1–4 (row 2), and the slug stream temperature, concentration, growth prefactor, and growth exponent (row 3, left to right). See Table 5.2 for input ranges.

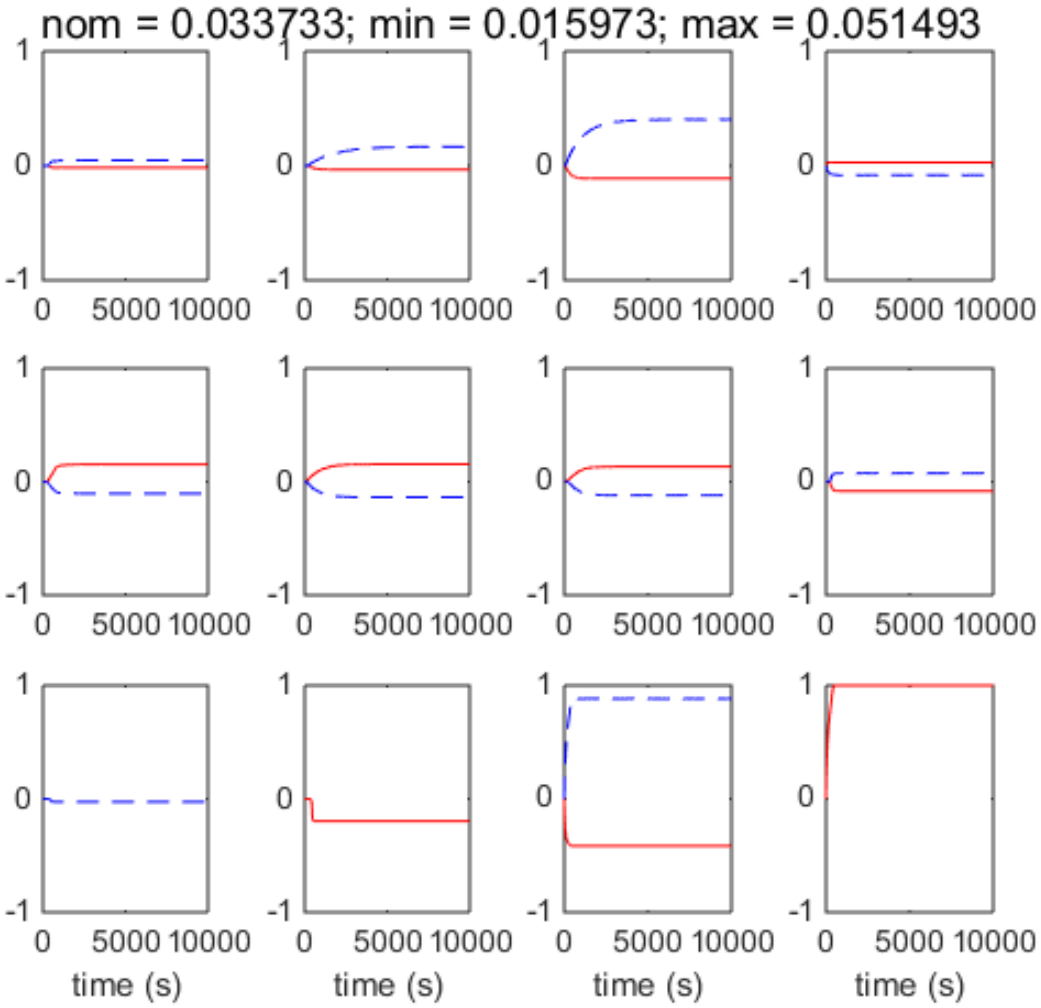

Figure 5.19: The normalized response of the maximum supersaturation within the fourth heat exchanger to step changes up (—) and down (- -) in the mass flow rate of cooling water for heat exchangers 1–4 (row 1), the inlet temperature of cooling water for heat exchangers 1–4 (row 2), and the slug stream temperature, concentration, growth prefactor, and growth exponent (row 3, left to right). See Table 5.2 for input ranges.

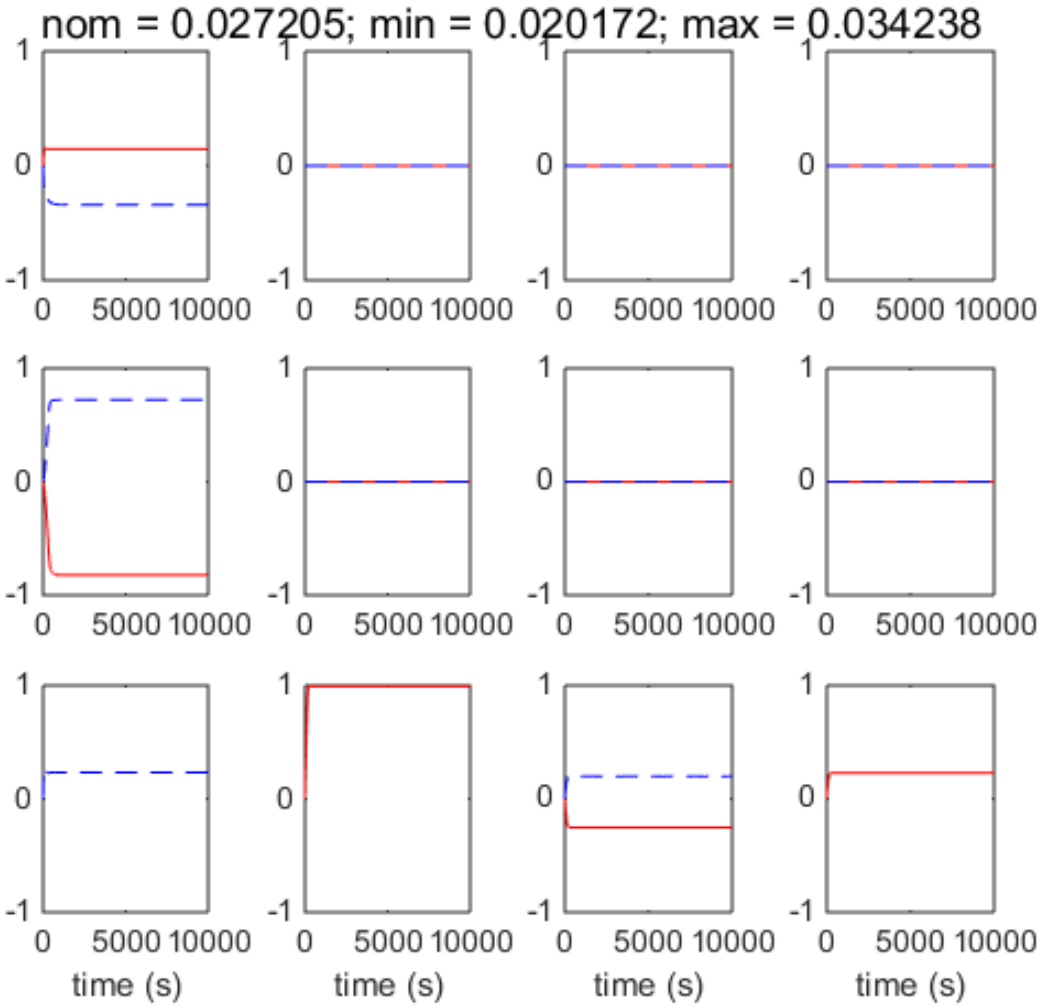

Figure 5.20: The normalized response of the average supersaturation within the first heat exchanger to step changes up (—) and down (- -) in the mass flow rate of cooling water for heat exchangers 1–4 (row 1), the inlet temperature of cooling water for heat exchangers 1–4 (row 2), and the slug stream temperature, concentration, growth prefactor, and growth exponent (row 3, left to right). See Table 5.2 for input ranges.

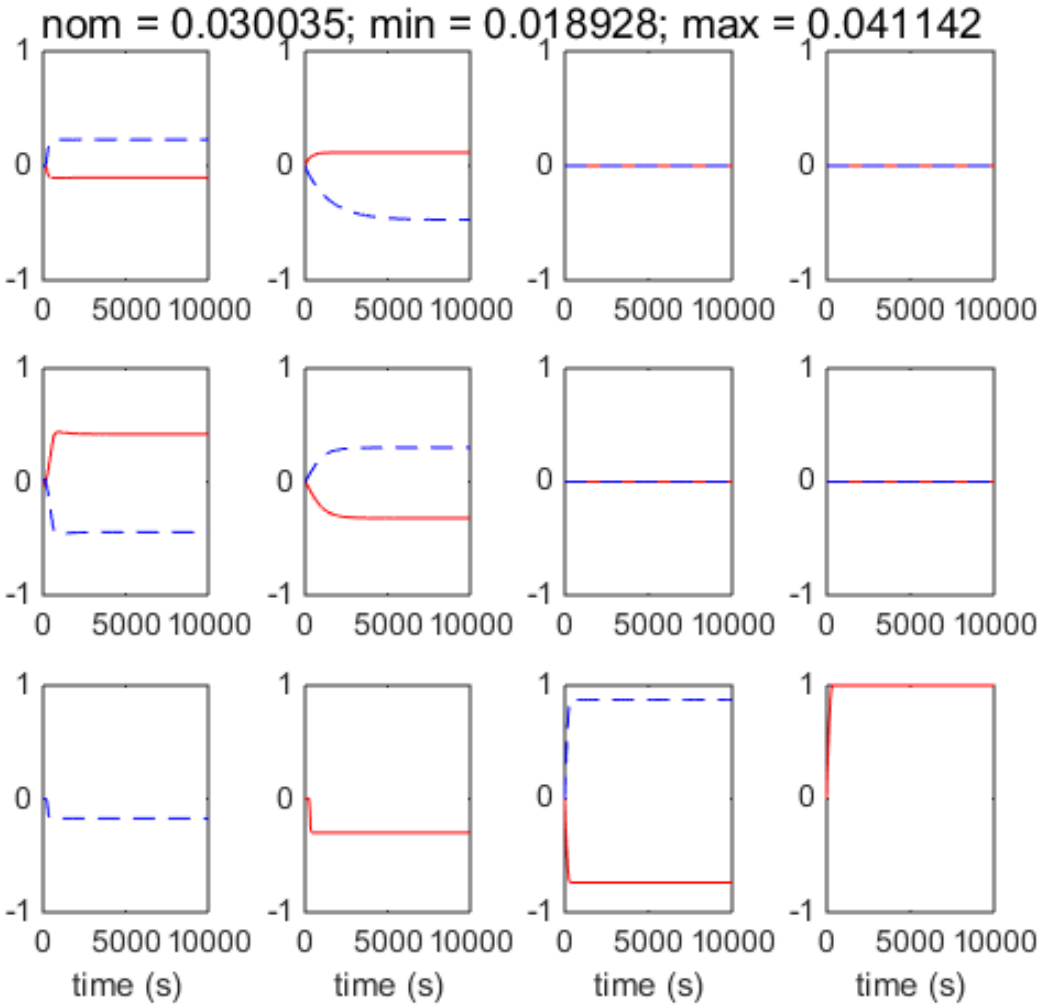

Figure 5.21: The normalized response of the average supersaturation within the second heat exchanger to step changes up (—) and down (- -) in the mass flow rate of cooling water for heat exchangers 1–4 (row 1), the inlet temperature of cooling water for heat exchangers 1–4 (row 2), and the slug stream temperature, concentration, growth prefactor, and growth exponent (row 3, left to right). See Table 5.2 for input ranges.

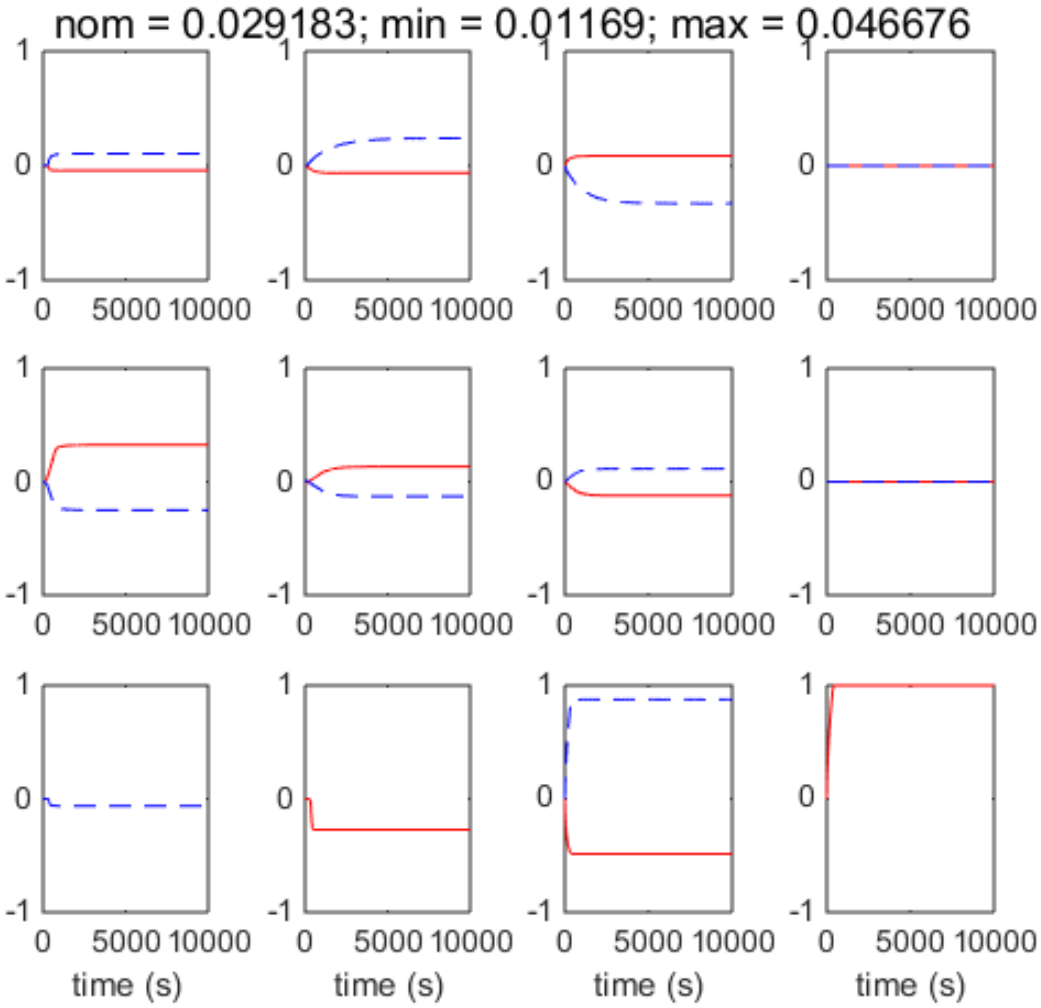

Figure 5.22: The normalized response of the average supersaturation within the third heat exchanger to step changes up (—) and down (- -) in the mass flow rate of cooling water for heat exchangers 1–4 (row 1), the inlet temperature of cooling water for heat exchangers 1–4 (row 2), and the slug stream temperature, concentration, growth prefactor, and growth exponent (row 3, left to right). See Table 5.2 for input ranges.

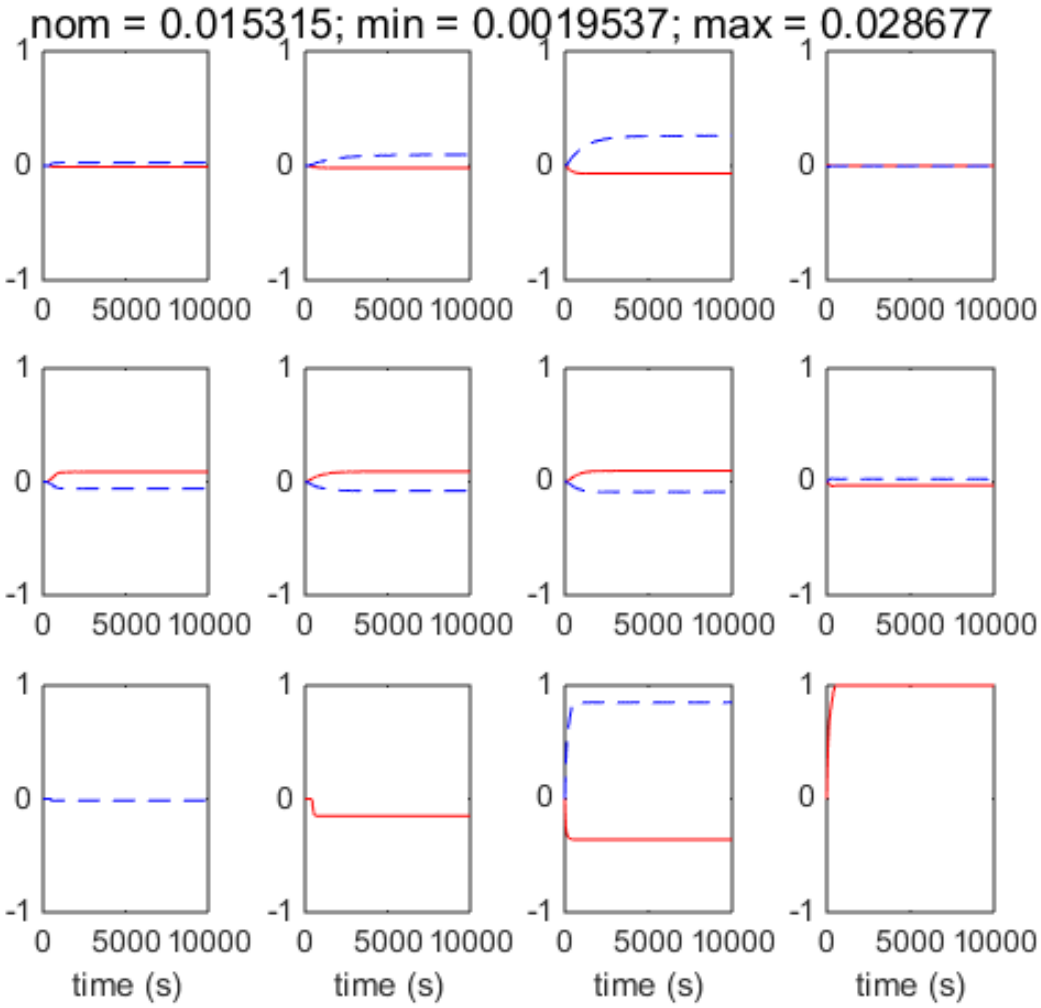

Figure 5.23: The normalized response of the average supersaturation within the fourth heat exchanger to step changes up (—) and down (- -) in the mass flow rate of cooling water for heat exchangers 1–4 (row 1), the inlet temperature of cooling water for heat exchangers 1–4 (row 2), and the slug stream temperature, concentration, growth prefactor, and growth exponent (row 3, left to right). See Table 5.2 for input ranges.

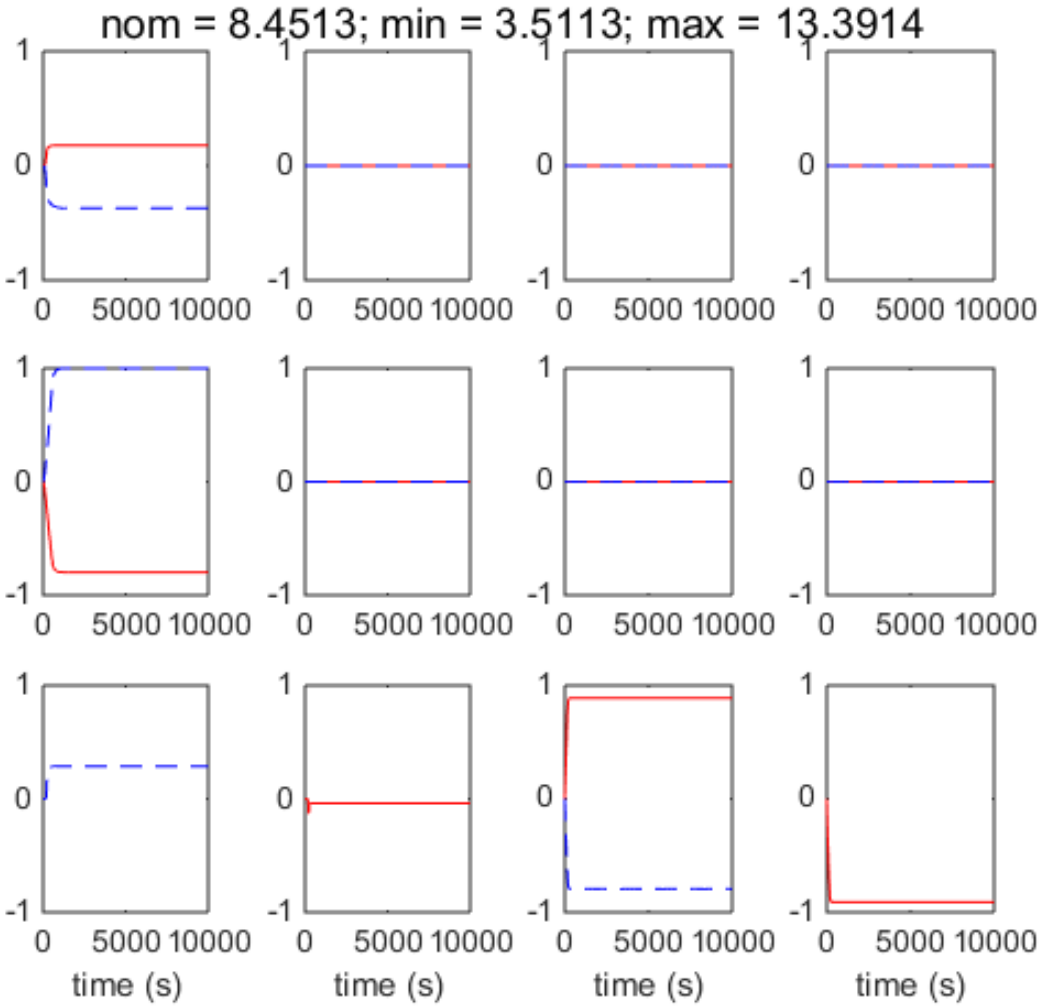

Figure 5.24: The normalized response of the yield at the exit of the first heat exchanger to step changes up (—) and down (- -) in the mass flow rate of cooling water for heat exchangers 1–4 (row 1), the inlet temperature of cooling water for heat exchangers 1–4 (row 2), and the slug stream temperature, concentration, growth prefactor, and growth exponent (row 3, left to right). See Table 5.2 for input ranges.

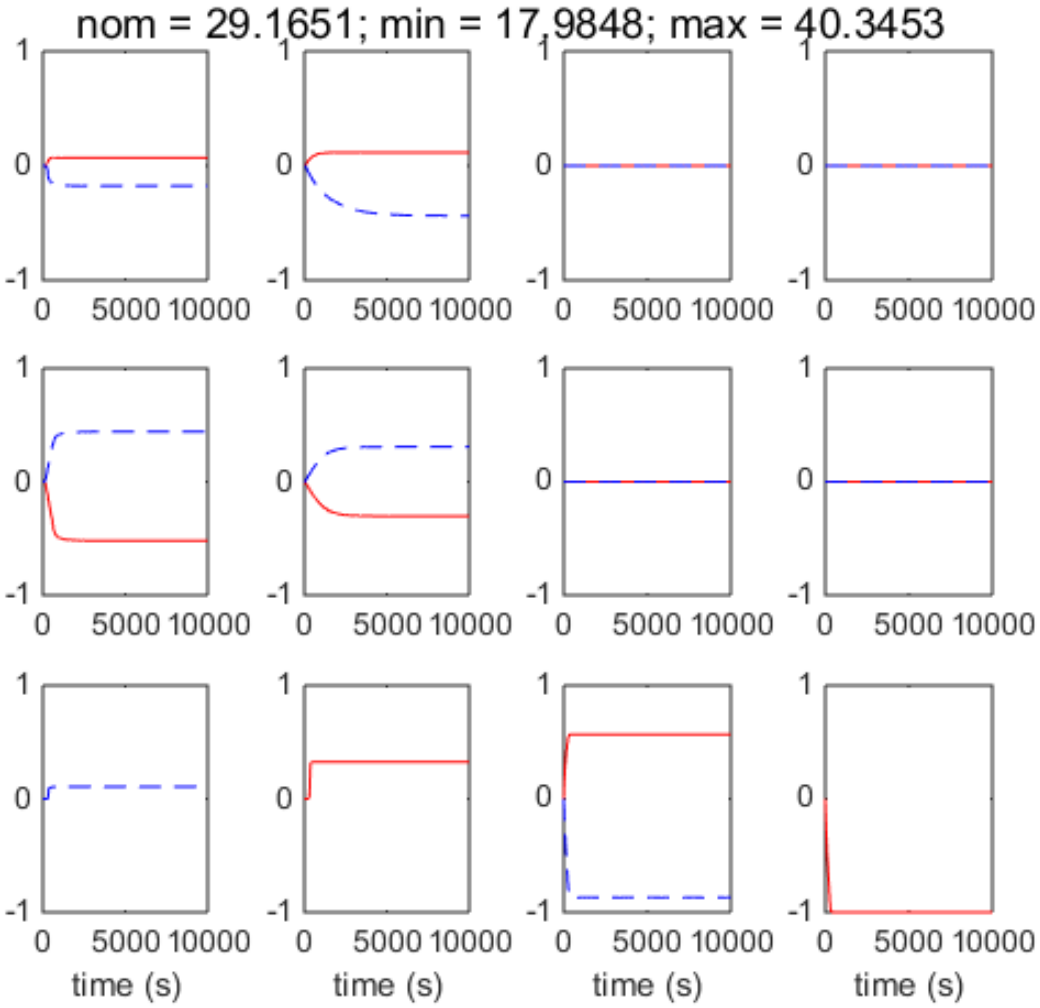

Figure 5.25: The normalized response of the yield at the exit of the second heat exchanger to step changes up (—) and down (- -) in the mass flow rate of cooling water for heat exchangers 1–4 (row 1), the inlet temperature of cooling water for heat exchangers 1–4 (row 2), and the slug stream temperature, concentration, growth prefactor, and growth exponent (row 3, left to right). See Table 5.2 for input ranges.

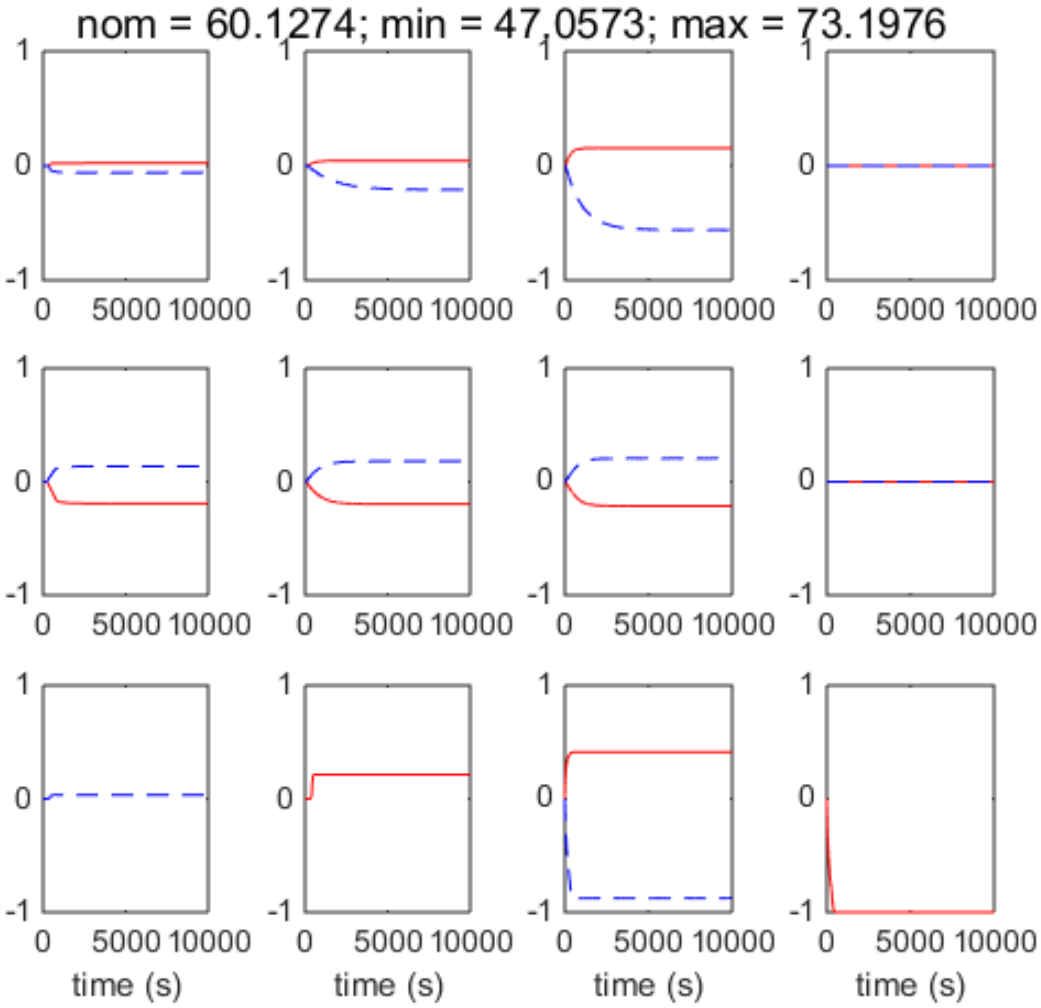

Figure 5.26: The normalized response of the yield at the exit of the third heat exchanger to step changes up (—) and down (- -) in the mass flow rate of cooling water for heat exchangers 1–4 (row 1), the inlet temperature of cooling water for heat exchangers 1–4 (row 2), and the slug stream temperature, concentration, growth prefactor, and growth exponent (row 3, left to right). See Table 5.2 for input ranges.

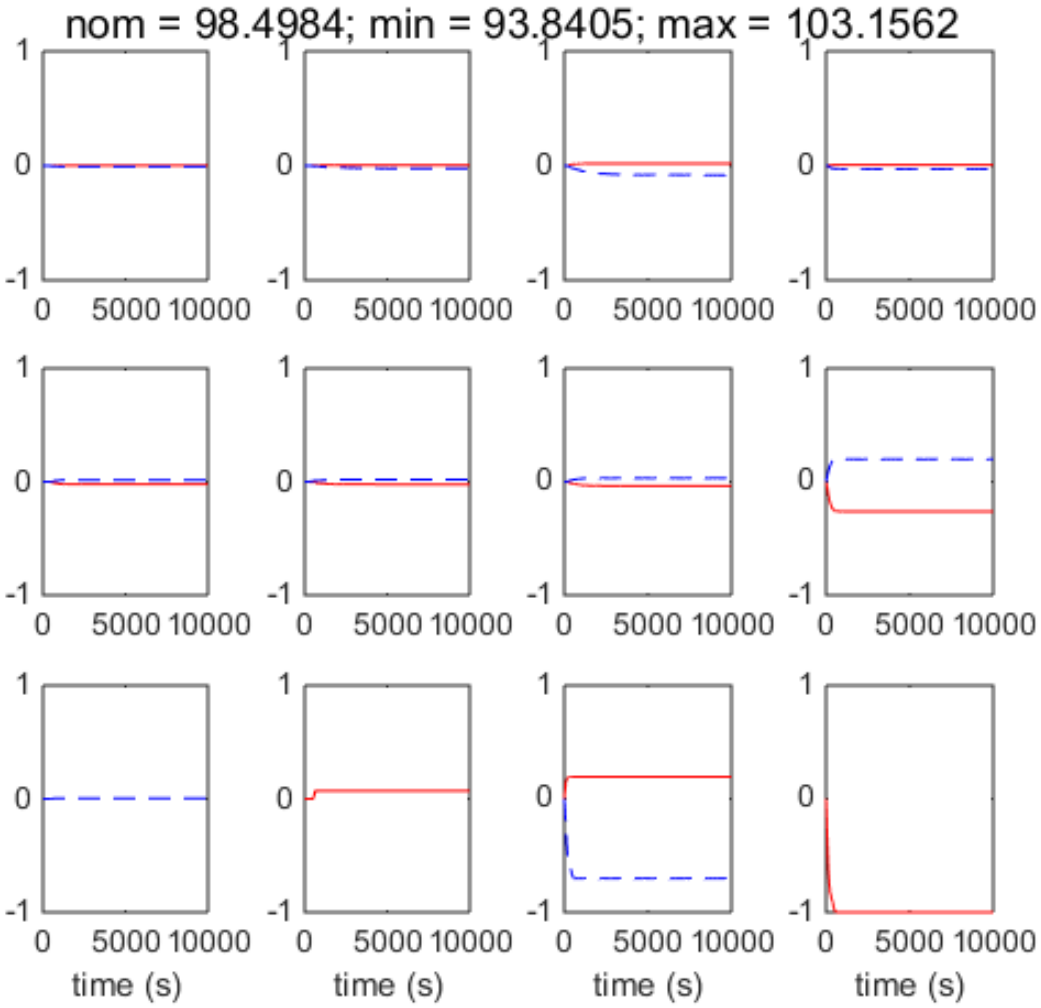

Figure 5.27: The normalized response of the yield at the exit of the fourth heat exchanger to step changes up (—) and down (- -) in the mass flow rate of cooling water for heat exchangers 1–4 (row 1), the inlet temperature of cooling water for heat exchangers 1–4 (row 2), and the slug stream temperature, concentration, growth prefactor, and growth exponent (row 3, left to right). See Table 5.2 for input ranges.

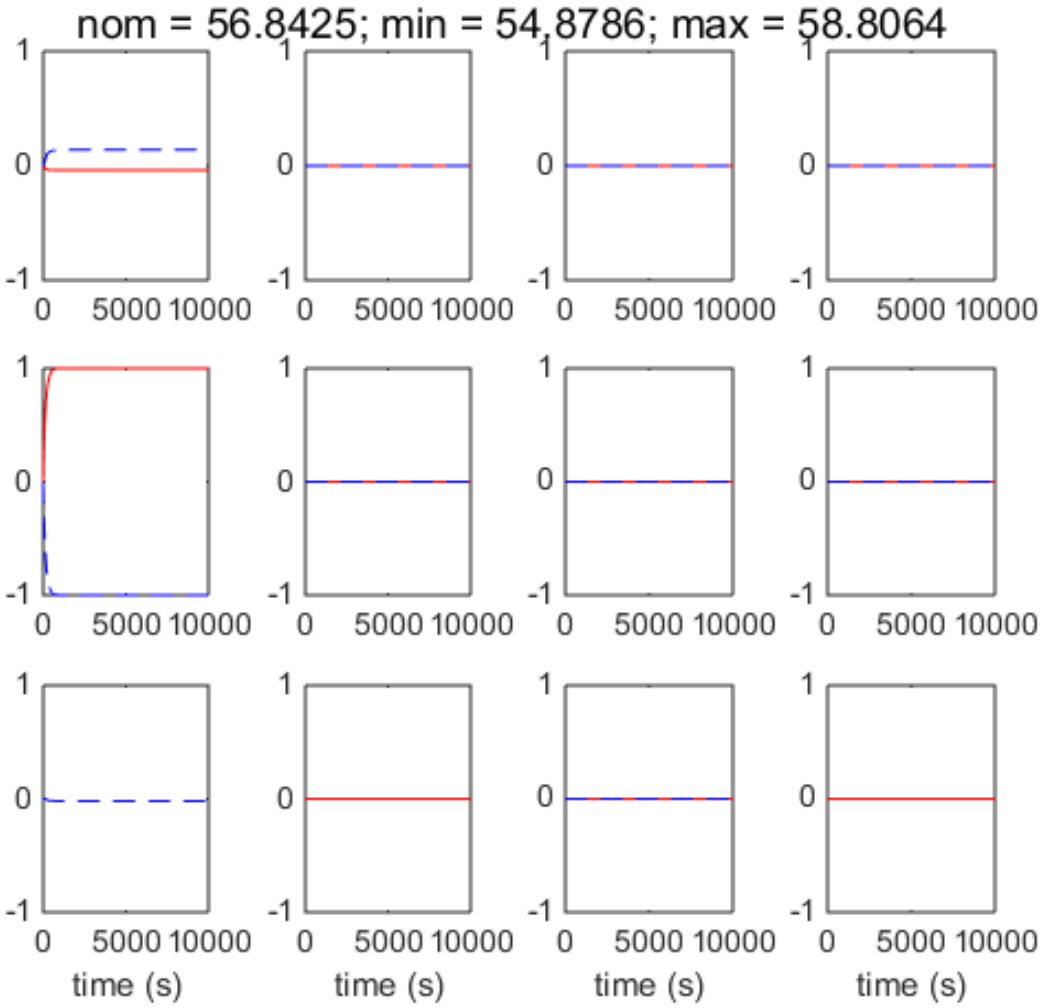

Figure 5.28: The normalized response of the slug stream temperature at the exit of the first heat exchanger to step changes up (—) and down (- -) in the mass flow rate of cooling water for heat exchangers 1–4 (row 1), the inlet temperature of cooling water for heat exchangers 1–4 (row 2), and the slug stream temperature, concentration, growth prefactor, and growth exponent (row 3, left to right). See Table 5.2 for input ranges.

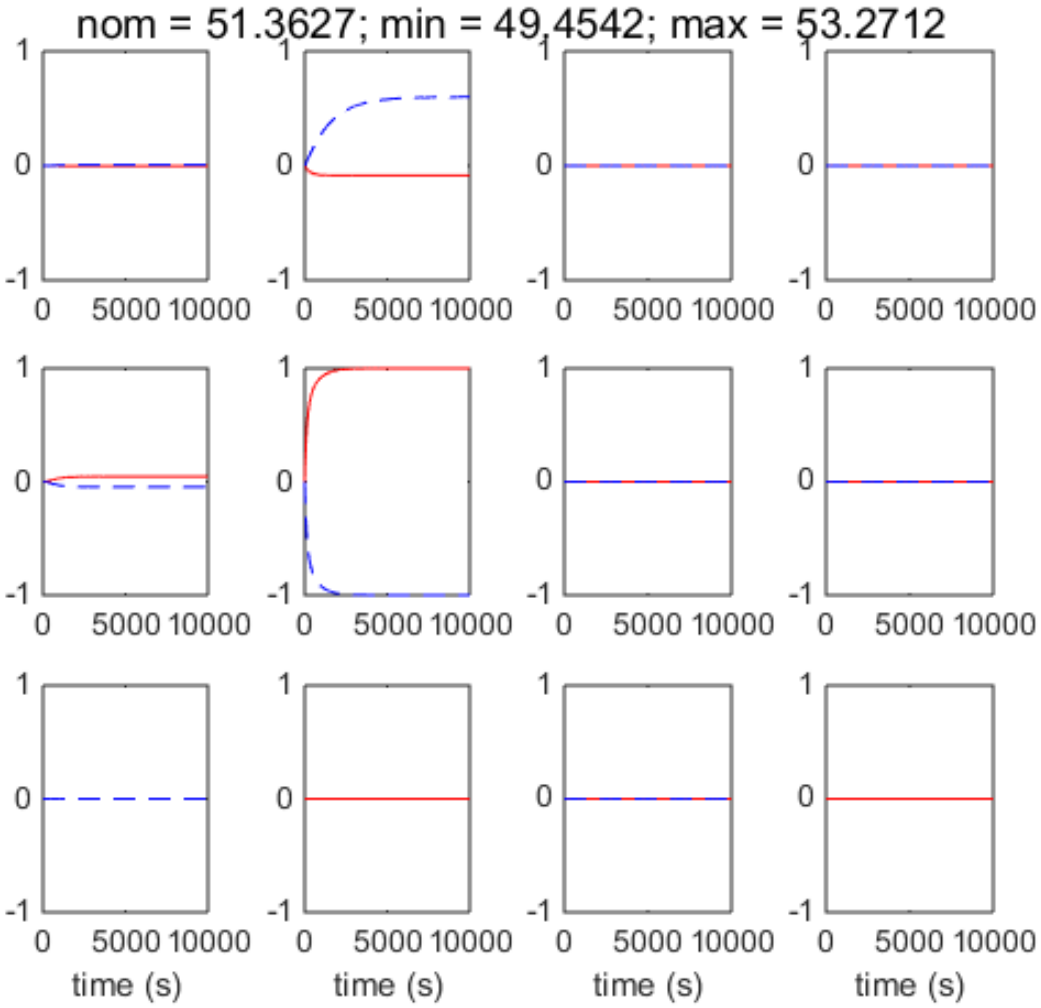

Figure 5.29: The normalized response of the slug stream temperature at the exit of the second heat exchanger to step changes up (—) and down (- -) in the mass flow rate of cooling water for heat exchangers 1–4 (row 1), the inlet temperature of cooling water for heat exchangers 1–4 (row 2), and the slug stream temperature, concentration, growth prefactor, and growth exponent (row 3, left to right). See Table 5.2 for input ranges.

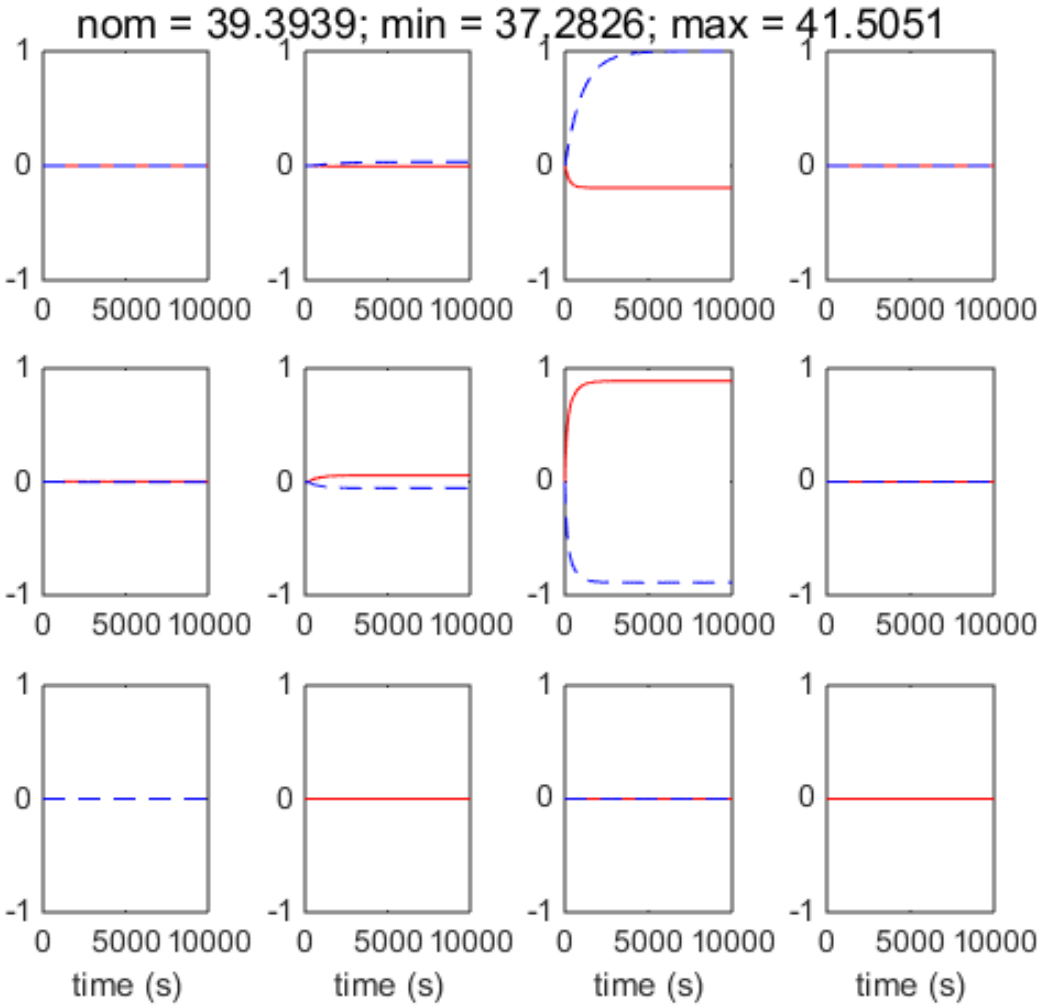

Figure 5.30: The normalized response of the slug stream temperature at the exit of the third heat exchanger to step changes up (—) and down (- -) in the mass flow rate of cooling water for heat exchangers 1–4 (row 1), the inlet temperature of cooling water for heat exchangers 1–4 (row 2), and the slug stream temperature, concentration, growth prefactor, and growth exponent (row 3, left to right). See Table 5.2 for input ranges.

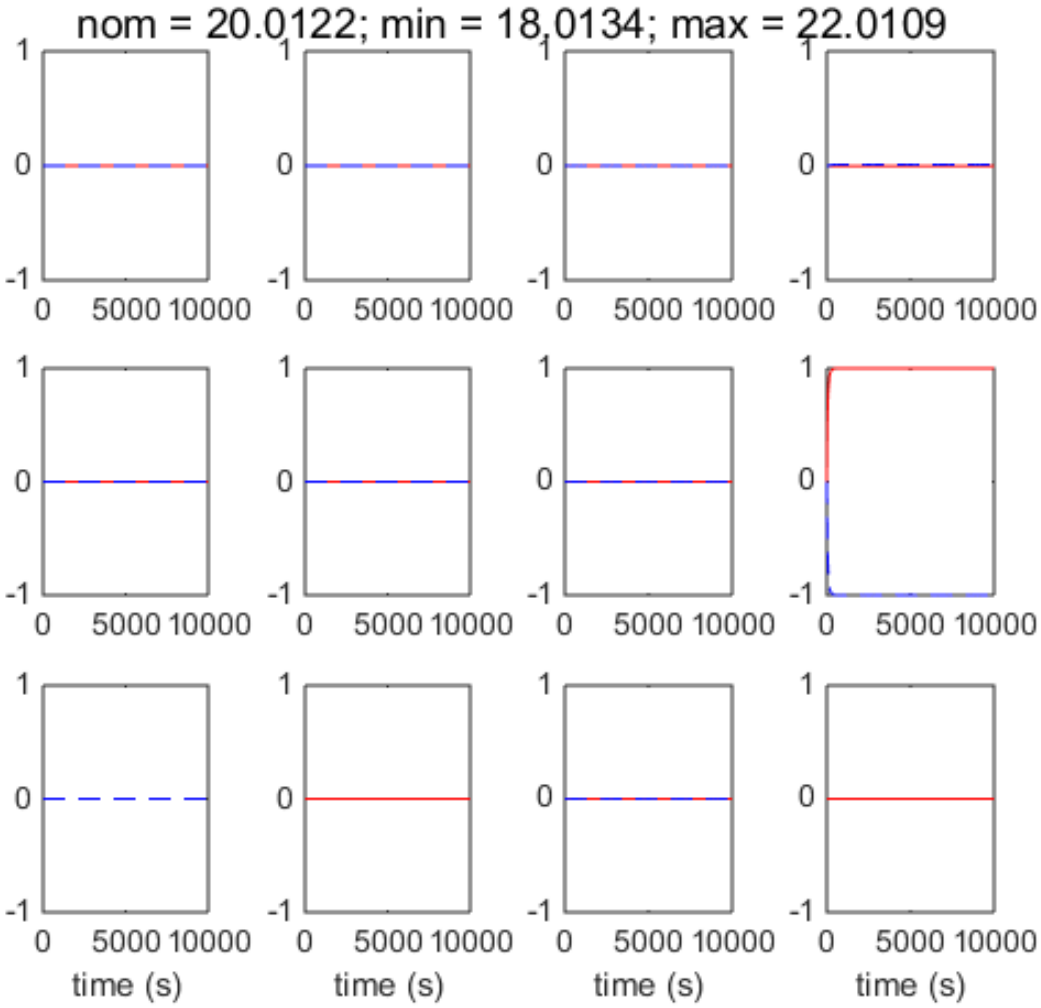

Figure 5.31: The normalized response of the temperature at the exit of the fourth heat exchanger to step changes up (—) and down (- -) in the mass flow rate of cooling water for heat exchangers 1–4 (row 1), the inlet temperature of cooling water for heat exchangers 1–4 (row 2), and the slug stream temperature, concentration, growth prefactor, and growth exponent (row 3, left to right). See Table 5.2 for input ranges.

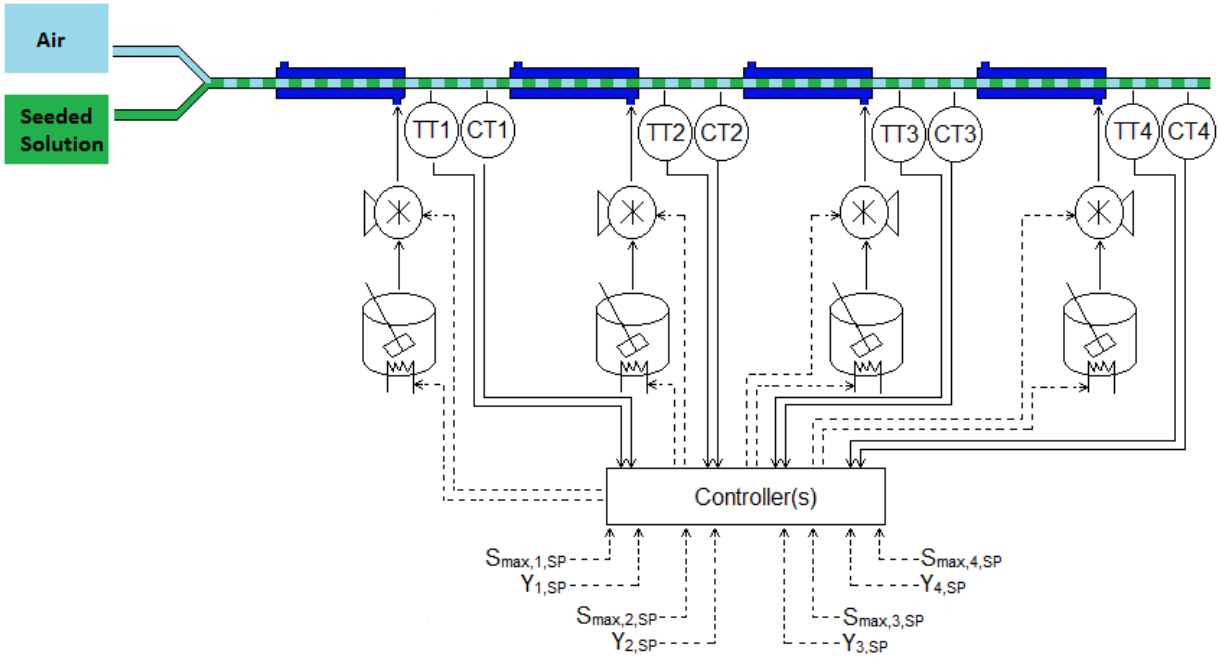

Figure 5.32: Control diagram for the complete set of eight measured and eight manipulated variables for the slug flow crystallizer. The unspecified control structure could use any of the suggested inputs/outputs.

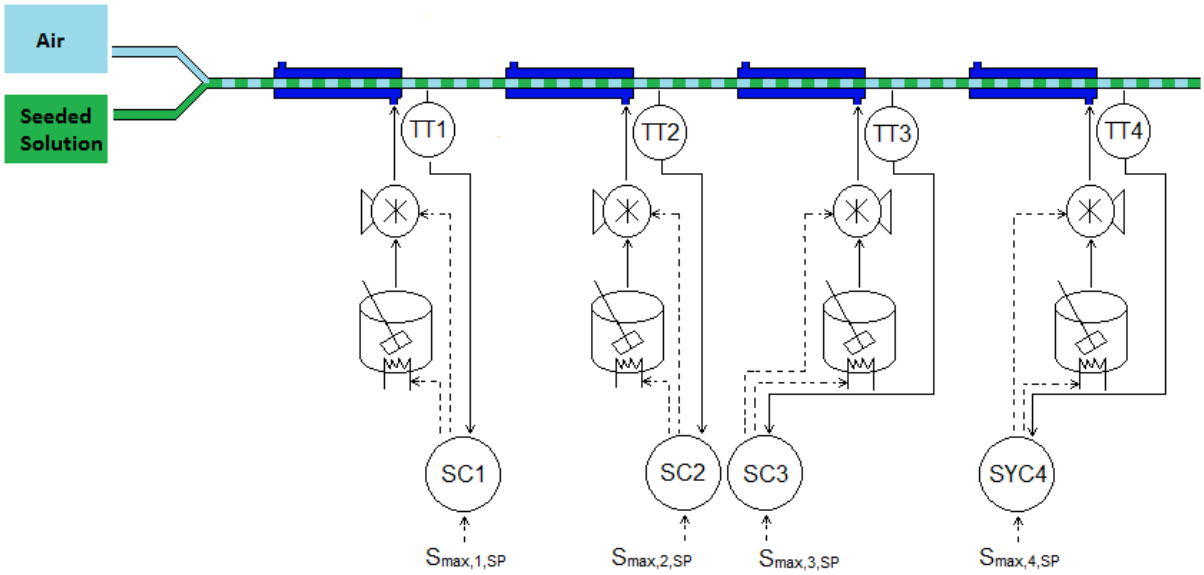

Figure 5.33: Example control diagram for the slug flow crystallizer using only the four measured slug stream temperatures and the four manipulated cooling water inlet temperatures.

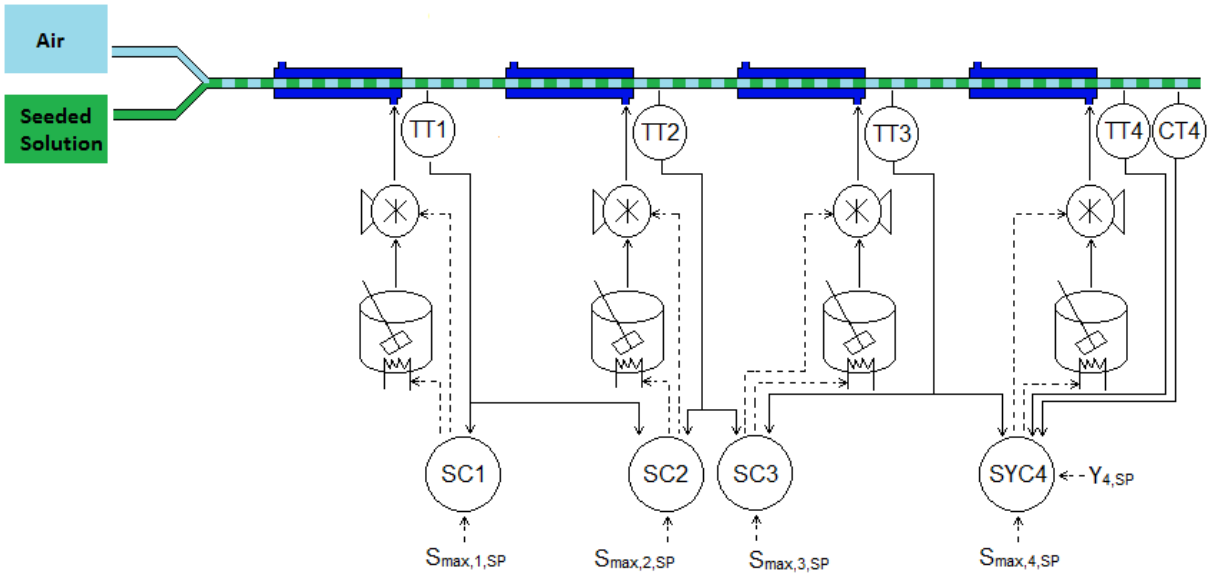

Figure 5.34: Control diagram for the slug flow crystallizer using five measured variables (the four exit temperatures and the outlet solute concentration) and eight manipulated variables (the four cooling water flowrates and four cooling water inlet temperatures). Each controller also receives the measured variable from the outlet of the previous heat exchanger.

5.6 Tables

Table 5.1: Optimal design parameters for Equation 5.40 which provide the value of 3.355 for the optimization argument when $\varepsilon_1 = 10^2$, $\varepsilon_2 = 10^3$, and $\varepsilon_3 = 2.0 \times 10^{-3}$. The length of the last heat exchanger is given by $\ell_4 = (15\text{ m}) - \sum_{i=1}^{3} \ell_i$. The final cooling water inlet temperature specified as $T_{c,in,4} = 20\,°\text{C}$.

Variable	Lower Bound	Upper Bound	Optimum	Units
ℓ_1	0.1	15	5.61	m
ℓ_2	0.1	15	3.00	m
ℓ_3	0.1	15	2.47	m
$\dot{m}_{c,1}$	70	500	348	mg/s
$\dot{m}_{c,2}$	70	500	72.0	mg/s
$\dot{m}_{c,3}$	70	500	74.9	mg/s
$\dot{m}_{c,4}$	70	500	304	mg/s
$T_{c,in,1}$	52	60	56.7	°C
$T_{c,in,2}$	45	52	51.1	°C
$T_{c,in,3}$	20	45	38.6	°C

Table 5.2: Values for step changes in the inputs to the simulation employed to elicit the dynamic responses of Figures 5.4-5.31. Converting the cooling water inlet temperatures from disturbances to manipulated variables would allow a greater stop change to be implemented for those four process inputs.

Variable	Nominal	Minimum	Maximum	Units
$\dot{m}_{c,1}$	348	213	483	mg/s
$\dot{m}_{c,2}$	72.0	38.2	106	mg/s
$\dot{m}_{c,3}$	74.9	41.2	109	mg/s
$\dot{m}_{c,4}$	304	169	439	mg/s
$T_{c,in,1}$	56.7	54.7	58.7	°C
$T_{c,in,2}$	51.1	49.1	53.1	°C
$T_{c,in,3}$	38.6	36.6	40.6	°C
$T_{c,in,4}$	20.0	18.0	22.0	°C
$T_{h,in}$	64.6	62.6	-	°C
C_{in}	0.16	-	0.17	g/g
k_g	6.353	4.765	7.941	(μm•g)/ (s•g)
g	1.0	-	1.1	-

CHAPTER 6

CONCLUSIONS

While reported here in the context of crystallization, processes involving the evolution of a particle size distribution are important in many industrial applications. Three distinct particulate processes are modeled and simulated in this thesis, which employs three distinct simulation solution methods for the population balance equation.

First, three possible breakage models describing the effects of ultrasonication on a distribution of aspirin crystals are developed and solved using matrix algebra. The models are evaluated by comparison to experimental data. A population balance model with two breakage parameters fit to data accurately described the effects of solvent viscosity and applied ultrasonic intensity, under the assumption that crystals broke in a binary fashion into equal-sized daughters. A computationally efficient algorithm for simulated particle breakage is developed. This computational model of sonofragmentation is the first that has been reported.

The second system investigated in this thesis involves a semi-batch antisolvent crystallization. The population balance equation was solved using the method of characteristics and a solute balance to derive a differential-algebraic system of equations. Optimization methods were used to determine parameters for growth and nucleation kinetics by comparison with concentration measurements. The desupersaturation information alone was shown to be sufficient to determine kinetic parameters that accurately predicted data not included in the kinetics estimation.

The third particulate process that was modeled and simulated is the slug-flow crystallizer, which is a tubular crystallizer developed for continuous crystallization in which slugs of well-

mixed supersaturated fluid are created spontaneously by hydrodynamics. A steady-state process model is derived and used to investigate two possible methods of multi-stage temperature control: thermal baths and shell-and-tube heat exchangers. The solution to the system of equations was obtained by the method of moments. Optimal designs for both temperature control systems were determined and described based on the criteria of maximizing yield while minimizing peak supersaturation. The shell-and-tube heat exchanger offered improved supersaturation values for the same length of tubing, and was therefore chosen for further evaluation.

A dynamic model of the shell-and-tube-based slug flow crystallizer was presented. While the dynamic model is consistent with the steady-steady state model, modifications to the design were necessary for the development of realistic control strategies. The dynamic responses of the process outputs were simulated that result from step changes in the process inputs (manipulated and disturbance variables as well as parameter uncertainty). Control strategies were then formulated based on the sensitivities.

REFERENCES

Alvarez, A.J., Myerson, A.S., 2010. Continuous plug flow crystallization of pharmaceutical compounds, Crystal Growth & Design, 56, 349-369.

Alvarez, A.J., Singh, A., Myerson, A.S., 2011. Crystallization of cyclosporine in a multistage continuous MSMPR crystallizer, Crystal Growth & Design, 11, 4392-4400.

Beck, J.V., Arnold, K.J., 1977. Parameter Estimation in Engineering and Science, New York: Wiley.

Bird, R.B., Stewart, W.E., Lightfoot, E.N., 2007. Transport Phenomena, 2nd edition, New York: John Wiley & Sons.

Braatz, R.D., 2012. The efficiency of the power of one (or zero), IEEE Control Systems, 32(1), 6-7.

Braatz, R.D., 2012. On internal stability and unstable pole-zero calculations, IEEE Control Systems, 32(5), 15-16.

Broadbent, S.R., Callcott, T.G., 1956. A matrix analysis of processes involving particle assemblies, Philosophical Transactions of the Royal Society of London A, 249, 99-123.

Bronk, B.V., 1979. Some inequalities for moments and coefficients of variation for a large class of probability functions, Journal of Applied Probability, 16(3), 665-670.

Bunce, D.J., 1995. The Transient Response of Heat Exchangers, M.S. Thesis, Rochester Institute of Technology.

Burton, J.A., Prim, R.C., Slichter, W.P., 1953. The distribution of solute crystals grown from the melt. Part 1. Theoretical, The Journal of Chemical Physics, 21, 1987-1991.

Chemical Book, CAS Database List, Accessed 28 October 2013. <http://www.chemicalbook.com/ChemicalProductProperty_EN_CB4380544.htm.>.

Chilton, T.H., Drew, T.B., Jenkins, R.H., 1944. Heat transfer coefficients in agitated vessels, Industrial & Engineering Chemistry, 36(6) 510-516.

Chung, S.H., Ma, D.L., Braatz, R.D., 1999. Optimal seeding in batch crystallization, The Canadian Journal of Chemical Engineering, 77, 590-596.

Colussi, A.J. Hung, H.M., Hoffmann, M.R., 1999. Sonochemical degradation rates of volatile solutes, Journal of Physical Chemistry A, 103, 2696-2699.

Crank, J., 1975. The Mathematics of Diffusion, 2nd edition, New York: Oxford University Press.

Curtain, R.F., Zwart, H., 1995. An Introduction to Infinite-Dimensional Linear Systems Theory, New York: Springer-Verlag.

Deen, W.M., 1998. Analysis of Transport Phenomena, New York: Oxford University Press.

Desoer, C.A., Wang, Y.T., 1980. On the generalized Nyquist stability-criterion, IEEE Transactions on Automatic Control, 25(2) 187-196.

Devarakonda, S., Evans, J.M.B., Myerson, A.S., 2004. Impact of ultrasonic energy on the flow crystallization of dextrose monohydrate, Crystal Growth & Design, 4, 687-690.

Dirker, J., Meyer, J.P., 2005. Convective heat transfer coefficients in concentric annuli, Heat Transfer Engineering, 26(2), 38-44.

Doktycz, S.J., Suslick, K.S., 1990. Interparticle collisions driven by ultrasound, Science, 247, 1067-1069.

Eder, R.J.P., Radl, S., Schmitt, E., Innerhofer, S., Maier, M., Gruber-Woelfler, H., Khinast, J.G., 2010. Continuously seeded, continuously operated tubular crystallizer for the production of active pharmaceutical ingredients, Crystal Growth & Design, 10(5), 2247-2257.

Eder, R.J.P., Schmitt, E.K., Grill, J., Radl, S., Gruber-Woelfler, H., Khinast, J.G., 2011. Seed loading effects on the mean crystal size of acetylsalicylic acid in a continuous-flow crystallization device, Crystal Research and Technology, 46(3), 227-237.

Eder, R.J.P., Schrank, S., Besenhard, O., Roblegg, E., Gruber-Woelfler, H., Khinast, J.G., 2012. Continuous sonocrystallization of acetylsalicylic acid (ASA): control of crystal size, Crystal Growth & Design., 12(10), 4733-4738.

Ferguson, S., Morris, G., Hao, H., Barrett, M., Glennon, B., 2012. In-situ monitoring and characterization of plug flow crystallizers, 18th International Symposium on Industrial Crystallization, 77, 105-111.

Fevotte, F., Fevotte, G., 2010. A method of characteristics for solving population balance equations (PBE) describing the adsorption of impurities during crystallization processes, Chemical Engineering Science, 65, 3191-3198.

Fujiwara, M., Chow, P.S., Ma, D.L., Braatz, R.D., 2002. Paracetamol crystallization using laser backscattering and ATR-FTIR spectroscopy: metastability, agglomeration, and control, Crystal Growth & Design, 2(5), 363-370.

Goh, L.M., Chen, K., Bhamidi, V., He, G., Kee, N.C.S., Kenis, P.J.A., Zukoski III, C.F., Braatz, R.D., 2010. A stochastic model for nucleation kinetics determination in droplet-based microfluidic systems, Crystal Growth & Design, 10(6), 2515-2521.

Goh, L.M., Kishida, M., Braatz, R.D., 2012. On the analysis of robust stability of metabolic pathways, IEEE Control Systems, 32(4), 92-94.

Grant, M.L., Saville, D.A., 1991. The role of transport phenomena in protein crystal growth, Journal of Crystal Growth, 108(1-2), 8-18.

Grant, M.L., Saville, D.A., 1995. Long term studies on tetragonal lysozyme crystals grown in quiescent and forced convection environments, Journal of Crystal Growth, 153(1-2), 23-54.

Guardani, R., Neiro, S.M.S., Bülau, H., Ulrich, J., 2001. Experimental comparison and simulation of static and dynamic solid layer melt crystallization, Chemical Engineering Science, 56, 2371-2379.

Gunawan, R., Fusman, I., Braatz, R.D., 2004. High resolution algorithms for multidimensional population balance equations with nucleation and size dependent growth, AIChE Journal, 50(11), 2738-2749.

Gunawan, R., Fusman, I., Braatz, R.D., 2008. Parallel high resolution simulation of particulate processes with nucleation, growth, and aggregation, AIChE Journal, 54, 1449-1458.

Guo, Z., Jones, A.G., Li, N., Germana, S., 2007. High speed observation of the effects of ultrasound on liquid mixing and agglomerated crystal breakage processes, Powder Technology, 171, 146-153.

Havighurst, R.J., 1953. Human Development and Education, New York: Longmans Green & Company.

Hua, H., Larson, R.G., 2005. Analysis of the microfluid flow in an evaporating sessile droplet, Langmuir, 21, 3963-3971.

Hua, H., Larson, R.G., 2005. Analysis of the effects of Marangoni stresses on the microflow in an evaporating sessile droplet, Langmuir, 21, 3972-3980.

Hulburt, H.M., Katz, S., 1964. Some problems in particle technology. A statistical mechanical formulation, Chemical Engineering Science, 19(8), 555-574.

Incropera, F.P., DeWitt, D.P., 2002. Fundamentals of Heat and Mass Transfer, 5th edition, Hoboken, NJ: Wiley.

Jiang, M., Wong, M.H., Zhu, Z., Zhang, J., Zhou, L., Wang, K., Ford Versypt, A.N., Si, T., Hasenberg, L.M., Li, Y.E., Braatz., R.D., 2012. Towards achieving a flattop crystal size distribution by continuous seeding and controlled growth, Chemical Engineering Science, 77, 2-9.

Jiang, M., Zhu, Z., Jimenez, E., Papageorgiou, C.D., Waetzig, J., Hardy, A., Langston, M., Braatz, R.D., 2014. Continuous-flow tubular crystallization in slugs spontaneously induced by hydrodynamics, Crystal Growth & Design, 14(2), 851-860.

Jiang, M., Zhu, X., Molaro, M.C., Rasche, M.L., Zhang, H., Chadwick, K., Raimondo, D.M., Kim, K.-K., Zhou, L., Zhu, Z., Wong, M.H., O'Grady, D., Hebrault, D., Tedesco, J., Braatz, R.D., 2014. Modification of crystal shape through deep temperature cycling, Industrial & Engineering Chemistry Research, 53(13), 5325-5336.

Kalinin, Y., Berejnov, V., Thorne, R.E., 2008. Controlling microdrop shape and position for biotechnology, Microfluid Nanofluidics, 5(4), 449-454.

Kashid, M.N., Gerlach, L., Goetz, S., Franzke, J., Acker, J.F., Platte, F., Agar, D.W., Turek, S., 2005. Internal circulation within the liquid slugs of a liquid-liquid slug flow capillary microreactor, 44(14) 5003-5010.

Kays, W.M., London, A.L., 1984. Compact Heat Exchangers, 3rd edition, New York: McGraw-Hill.

Krstic, M., Smyshlyaev, A., 2008. Boundary Control of PDEs: A Course on Backstepping Designs. Philadelphia, Pennsylvania: Society for Industrial and Applied Mathematics (SIAM).

Kubota, N., Mullin, J.W., 1995. A kinetic model for crystal growth from aqueous solution in the presence of impurity, Journal of Crystal Growth, 152(3), 203-208.

Lawton, S., Steele, G., Shering, P., Zhao, L., Laird, I., Ni, X.-Y., 2009. Continuous crystallization of pharmaceuticals using a continuous oscillatory baffled crystallizer, Organic Process Research & Development, 13(6), 1357-1363.

Levenspiel, O., 1962. Chemical Reaction Engineering: An Introduction to the Design of Chemical Reactors, New York: Wiley.

Lifshitz, D.A., Williams, Jr., J.C., Sturtevant, B., Connors, B.A., Evan, A.P, McAteer, J.A. 1997. Quantitation of shock wave cavitation damage *in vitro,* Ultrasound in Medicine & Biology, 23, 461-471.

Lin, H., Petsev, D.N., Yau, S.-T., Thomas, B.R., Vekilov, P.G., 2001. Lower incorporation of impurities in ferritin crystals by suppression of convection: modeling results, Crystal Growth & Design, 1(1), 73-78.

Ma, D.L., Tafti, D.K., Braatz, R.D., 2002. High resolution simulation of multidimensional crystal growth, Industrial & Engineering Chemistry Research, 41, 6217-6223.

Ma, D.L., Tafti, D.K., Braatz, R.D., 2002. Optimal control and simulation of multidimensional population balance equations, Computers and Chemical Engineering, 26, 1103-1116.

Mangun, C.L., Braatz, R.D., Economy, J.D., Hall, A.J., 1999. Fixed bed adsorption of acetone and ammonia onto oxidized activated carbon fibers, Industial & Engineering Chemical Research, 38(9), 3499-3504.

Miller, S.M., Rawlings, J.B., 1994. Model identification and control strategies for batch cooling crystallizers, AIChE Journal, 40(8), 1312-1327.

Milliken, W.J., Stone, H.A., Leal, L.G., 1993. The effect of surfactant on the transient motion of Newtonian drops, Physics of Fluids A, 5(1), 69-79.

Myerson, A.S., 2002. Handbook of Industrial Crystallization, 2nd edition, Boston: Butterworth-Heinemann.

Nagy, Z.K., Fujiwara, M., Braatz, R.D., 2008. Modeling and control of combined cooling and antisolvent crystallization processes, Journal of Process Control, 18, 856-864.

Quon, J.L., Zhang, H., Alvarez, A., Evans, J., Myerson, A.S., Trout, B.L., 2012. Continuous Crystallization of Aliskiren Hemifumarate, Crystal Growth & Design, 12, 3036-3044.

Raman, V., Abbas, A., 2008. Experimental investigations on ultrasound mediated particle breakage, Ultrasonics Sonochemistry, 15(1), 55-64.

Raman, V., Abbas, A., Zhu, W., 2011. Particle grinding by high intensity ultrasound: kinetic modeling and identification of breakage mechanisms, AIChE Journal, 57(8), 2025-2035.

Randolph, A.D., Larson, M.A., 1974. Theory of Particulate Processes: Analysis and Techniques of Continuous Crystallization, volume 2nd, New York: Academic Press.

Rosenberger, F., Riveros, H.G., 1974. Segregation in alkali halide crystallization from aqueous solutions, The Journal of Chemical Physics, 60, 668-673.

Ruthven, D.M., 1984. Principles of Adsorption and Adsorption Processes. New York: John Wiley & Sons.

Sieder, E.N., Tate, G.E., 1936. Heat transfer and pressure drop of liquid in tubes, Idustrial & Engineering Chemistry, 28(12) 1429-1435.

Skogestad, S., Postlethwaite, I., 2005. Multivariable Feedback Control: Analysis and Design. New York: Wiley.

Son, Y., Lim, M., Kim, J., 2009. Investigation of acoustic cavitation energy in a large-scale sonoreactor, Ultrasonics Sonochemistry, 16, 552-556.

Suslick, K.S., Didenko, Y., Fang, M.M., Hyeon, T., Kolbeck, K.J., Mcnamara III, W.B., Mdleleni, M.M., Wong, M., 1999. Acoustic cavitation and its chemical consequences, Philosophical Transactions of the Royal Society of London A, 357, 335-353.

Talreja, S., Kim, D.Y., Mirarefi, A.Y., Zukoski, C.F., Kenis, P.J.A., 2005. Screening and optimization of protein crystallization conditions through gradual evaporation using a novel crystallization platform, Journal of Applied Crystallography, 21(23), 10537-10544.

Tan, H.S., Salman, A.D., Hounslow, M.J., 2004. Kinetics of fluidized bed melt granulation IV. Selecting the breakage model, Powder Technology, 143-144, 65-83.

Teipel, U., Leisinger, K., Mikonsaari, I., 2004. Comminution of crystalline material ultrasonics, International Journal of Mineral Processing, 74, S183-S190.

Teipel, U., Mikonsaari, I., 2002. Size reduction of particulate energetic material, Propellants, Explosives, Pyrotechnics, 27, 168-174.

Togkalidou, T., Braatz, R.D., Johnson, B.K., Davidson, O., Andrews, A., 2001. Experimental design and inferential modeling in pharmaceutical crystallization, AIChE Journal, 47, 160-168.

Vacassy, R., Lemaitre, J., Hofmann, H., Gerlings, J.H., 2000. Calcium carbonate precipitation using new segmented flow tubular reactor. AIChE Journal, 46(6), 1241-1252.

Wagterveld, R.M., Boels, L., Mayer, M.J., Witkamp, G.J., 2011. Visualization of acoustic cavitation effecs on suspended calcite crystals, Ultrasonics Sonochemistry, 18, 216-225.

Wirz, D., 2009. Commercial Refrigeration for Air Conditioning Technicians, 2nd edition, Clifton Park, New York: Delmar.

Woo, X.Y., Tan, R.B.H., Chow, P.S., Braatz, R.D., 2006. Simulation of mixing effects in antisolvent crystallization using a coupled CFD-PDF-PBE approach, Crystal Growth & Design, 6, 1291-1303.

Woo, X.Y., Tan, R.B.H., Braatz, R.D., 2009. Modeling and computational fluid dynamics – population balance equation – micromixing simulation of impinging jet crystallizers, Crystal Growth & Design, 9, 156-164.

Woo, X.Y, Tan, R.B.H., Braatz, R.D., 2011. Precise tailoring of the crystal size distribution by controlled growth and continuous seeding from impinging jet crystallizers, CrystEngComm, 13, 2006-2014.

Yu, L.X., Lionberger, R.A., Raw, A.S., D'Costa, R., Wu, H., Hussain, A.S., 2004. Applications of process analytical technology to crystallization processes, Advanced Drug Delivery Reviews, 56, 349-369.

Zeiger, B.W., Suslick, K.S., 2011. Sonofragmentation of molecular crystals, Journal of the American Chemical Society, 133, 14530-14533.

Zhou, G.X., Fujiwara, M., Woo, X.Y., Rusli, E., Tung, H.-H., Starbuck, C., Davidson, O., Ge, Z., Braatz, R.D., 2006. Direct design of pharmaceutical antisolvent crystallization through concentration control, Crystal Growth & Design, 6(4), 892-898.

APPENDIX A

IMPURITY INCORPORATION DURING CRYSTALLIZATION

The main purpose of a crystallization as a purification process is to remove impurities from the mother liquor. Ironically, the vast majority of the literature on the modeling of crystallization from solutions ignores the modeling of impurities.

Impurity incorporation is limited by mass transport and equilibrium (Myerson, 2002). When a system is well-mixed, one might choose a model based only on equilibrium considerations. The most common methods involve defining a distribution coefficient, K_i', as a ratio of relative purity in the solid and liquid phase. For example (Alvarez et al., 2011; Quon et al., 2012),

$$K_i' = \frac{\left(C_{imp} / C\right)_{solid}}{\left(C_{imp} / C\right)_{liquid}}, \tag{A.1}$$

where C is the concentration of the compound to be purified, and C_{imp} is the concentration of the impurity. When the distribution coefficient is given in terms of a mole fraction, Equation A.1 becomes

$$K_i = \frac{\left(x_i / x\right)_{solid}}{\left(x_i / x\right)_{liquid}} \approx \frac{x_{i,solid}}{\left(x_i / x\right)_{liquid}}, \tag{A.2}$$

where under conditions of low impurity, the mole fraction of the desired solute molecule in the solid phase can be approximated as $x_{solid} = 1$.

One method of determining the distribution coefficients of Equations A.1 and A.2 is through the analysis of experimental data. When such data is unavailable, Rosenberger &

Riveros (1974) derived an expression for the distribution coefficient in Equation A.2 from the thermodynamics of aqueous solutions as

$$K_i = \frac{\gamma'_{i,liquid}}{\gamma^{sat}_{i,liquid}} \frac{x^{sat}_{liquid}}{x^{sat}_{i,liquid}} \exp\left(\frac{-\Delta H^{d}_{i,solid} + T\Delta S^{vibr}_{i,solid}}{RT} \right), \tag{A.3}$$

where $\gamma'_{i,liquid}$ is the activity coefficient for the interaction of impurity-solute and impurity-solvent, $\gamma^{sat}_{i,liquid}$ is the activity coefficient for the interaction of impurity-saturated solution, x^{sat}_{liquid} is the solubility of the solute compound, $x^{sat}_{i,liquid}$ is the solubility of impurity, $\Delta H^{d}_{i,solid}$ is the heat of dissolution of impurity in the solid phase, T is the average solution temperature, $\Delta S^{vibr}_{i,solid}$ is the vibrational entropy change of the impurity due to incorporation in the solid phase, and R is the ideal gas constant. Rosenberger & Riveros (1974) go on to suggest that the activity ratio of Equation A.3 is generally close to unity, and that the dominant term in the remaining product is $\exp\left(-\Delta H^{d}_{i,solid} / RT\right)$, with respect to the effect on the order of magnitude of the distribution coefficient, K_i.

Burton et al., (1953) modified the distribution coefficient (Equation A.3) to reflect transport limitations for crystallization in a melt by performing the following derivation. Beginning with the 1D conservation equation,

$$D\frac{d^2C}{dx^2} + G\frac{dC}{dx} = 0, \tag{A.4}$$

where D is the diffusion coefficient of the solute in solvent, and G is the crystal growth rate, with boundary conditions given by

$$C(x = \delta) = C_L, \tag{A.5}$$

$$\left(C_0 - C_S\right) + D\left.\frac{dC}{dx}\right|_{x=0} = 0, \tag{A.6}$$

where δ is the length of the diffusion boundary layer, C_L is the concentration of impurity in the liquid, C_0 is the concentration of impurity at the solid-liquid interface, and C_s is the concentration of impurity in the solid, Burton et al., (1953) modified the distribution coefficient (Equation A.3) to reflect transport limitations for crystallization in a melt by deriving the following equation:

$$K_e = C_S / C_L = \frac{K_i}{K_i + (1 - K_i)\exp(-\delta G / D)}, \tag{A.7}$$

where K_e is an effective distribution coefficient.

The presence of impurities in a crystalline lattice can also have the effect altering the growth rate (Kubota & Mullin, 1995; Guardani et al., 2001; Fevotte & Fevotte, 2010). Kubota and Mullin (1995) present the following relationship for the ratio of the actual step velocity, V, to the step velocity in the pure system, V_0 .

$$V / V_0 = 1 - \alpha\theta_{eq}, \tag{A.8}$$

where α is an efficiency factor which accounts for the size of the impurity compound relative to the solute it hinders, and θ_{eq} is the fractional coverage of the crystal surface onto which the impurity has adsorbed, commonly approximated by the Langmuir isotherm,

$$\theta_{eq} = KC_{imp,liquid} / (1 + KC_{imp,liquid}), \tag{A.9}$$

where K is the Langmuir constant. Making the assumption that the linear growth rate is proportional to the step velocity, i.e. $G \propto V$, and defining the efficiency factor as

$$\alpha = \frac{\gamma a}{kT\sigma L}, \tag{A.10}$$

where γ is the edge free energy, a is the surface area occupied by one crystallizing molecule, k is the Boltzmann constant, T is the absolute temperature , σ is the supersaturation, and L is the

separation of sites available for impurity adsorption, a modified growth rate was calculated by Fevotte & Fevotte (2010) so that

$$G(t) = G_0(t)\left(1-\alpha\frac{KC_{imp,liquid}}{1+KC_{imp,liquid}}\left[1-\exp\left(\frac{t-v}{\tau}\right)\right]\right). \quad \text{(A.11)}$$

In Equation A.11, the adsorption process has been modified to obey first order dynamics (Kubota et al., 2001) with time constant, τ. While the analysis of Fevotte & Fevotte (2010) defines v as the time at which a particular particle was formed (at nucleation) and therefore increases the dimension of the problem, in a case where nucleation and growth can be decoupled, the dimension of the problem is not increased (i.e. $v = 0$ for every particle). If it can further be assumed that the adsorption is instantaneous, then the time-dependency of Equation A.1 is removed and

$$G = G_0\left(1-\alpha\frac{KC_{imp,liquid}}{1+KC_{imp,liquid}}\right) \quad \text{(A.12)}$$

Equation A.12 can be combined with Equations A.3, A.7, and A.10 to provide an expression for the impurity incorporation at steady state. It is clear from Equation A.7 that the effective distribution coefficient is a monotonic function of growth rate, and therefore, that the impurity incorporation is a monotonic function of supersaturation (Equations A.3, A.10, and A.12). In the slug flow crystallizers of Chapter 4 and 5, impurity incorporation is minimized by minimizing the supersaturation.

APPENDIX B

ANALYTICAL BOUNDS FOR CRYSTALLIZATION IN A HANGING DROP EXPERIMENT

B.1 Problem Description

In chemical engineering practice, the characteristics of even simple systems can require the solution of complicated systems of equations – a fact that is evident to instructors attempting to develop exam problems that are not given in the textbook but are solvable within an exam period. Much of undergraduate chemical engineering education is focused on making enough assumptions to derive an approximate analytical solution, without considering whether each assumption would be expected to cause an increase or decrease in the variables to be estimated. Often upper and lower bounds can be determined without the full solution, and often these bounds provide enough information to make an engineering decision, even when the bounds are far apart and an undergraduate has long given up on trying to derive an analytical solution or has produced an analytical solution with unknown accuracy. Having both upper and lower bounds provides a bound on the accuracy of the analytical estimation and, at minimum, such bounds provide a route for assessing the reasonableness of more exact solutions determined by simulation software. It is our opinion that more attention should be paid to training undergraduate chemical engineers how to derive simple analytical bounds, and this brief note provides an example of the derivation of such bounds that can be used in a lecture or in a homework or exam problem.

The example involves bounding the protein concentration in a solution within an evaporating droplet. High-throughput droplet evaporation platforms can be used for the

search of polymorphic crystal forms or to estimate nucleation kinetics at high supersaturation for fundamental studies or in simulations of dual-impinging-jet crystallization (Goh et al., 2010; Woo et al., 2009; Talreja et al., 2005). Many of these platforms are based on the classical hanging drop experiment (Figure B.1). The particular platform in Figure B.1 is made of a polydimethylsiloxane (PDMS) layer about 7 mm thick with a cylindrical evaporation chamber of 5 mm in diameter and an evaporation channel that is 5-10 mm long with a 250×250 to 1000×1000 micron cross section (Talreja et al., 2005). A drop of saturated solution is placed on a glass substrate that is then fused to the PDMS layer. The evaporation rate is determined by the length and cross-sectional area of the evaporation channel.

The objective is to estimate the maximum difference in protein concentration within the evaporating drop as the solvent evaporates, before any protein has crystallized. As the solvent evaporates, a concentration gradient develops resulting in diffusive transport toward the center of the droplet (Figure B.2). The protein concentration within the droplet is governed by diffusion and buoyancy- and surface-driven convection (Grant & Saville, 1991; Grant & Saville, 1995), and the conservation equation for protein in solution within the drop is

$$\frac{\partial C}{\partial t}+\underline{u}\cdot\underline{\nabla}C=D\nabla^2C \tag{B.1}$$

where C is the protein concentration in solution, $\underline{u}$ is the velocity, D is the diffusion coefficient for dissolved protein in aqueous solution, and t is time. This equation assumes that the protein concentration is low enough that Fick's Law in terms of concentration is valid, and that the diffusion coefficient is independent of solution concentration. The velocity, $\underline{u}$, is described by the momentum balance equation solved simultaneously with a

mass continuity equation for the solution density whose spatial variation accounts for buoyancy-driven flow and the interfacial tension differences along the drop surface act as boundary conditions (Milliken et al., 1993; Lin et al., 2001; Hua & Larson, 2005; Hua & Larson, 2005). Both phenomena that induce convection are a result of evaporation-induced concentration and/or temperature differences.

The solution would involve combining phenomena that are best described by different coordinate systems; i.e. diffusion and Marangoni convection are spherical in this case, but natural (gravity-induced) convection is inherently Cartesian. An analytical solution for the convection-diffusion problem described above is not reported in the literature, but the pure diffusion case is expected to provide an upper bound on this maximum concentration difference, since convection would create increased mixing within the evaporating drop.

B.2 Bounding Method

Assuming an isothermal droplet undergoing a constant evaporation flux and retention of the hemispherical shape, the partial differential equations describing the concentration of water within the drop can be written as

$$\frac{\partial C}{\partial t} = \frac{D}{r^2}\frac{\partial}{\partial r}\left(r^2 \frac{\partial C}{\partial r}\right) \tag{B.2}$$

$$C(r, t=0) = C_0 \tag{B.3}$$

$$-D\frac{\partial C}{\partial r}(r = R, t) = F_0 \tag{B.4}$$

$$\frac{\partial C}{\partial r}(r = 0, t) = 0 \tag{B.5}$$

where r is the radial coordinate, R is the droplet radius, and F_0 is the evaporation flux.

The assumption of a hemispherical shape is an approximation. The real drop would be flatter than a hemisphere due to adhesion of the water to the glass slip. While the drop could be made more hemispherical by chemical and physical manipulation of the surface of the glass slip (Kalinin et al., 2008), some deviation from a hemispherical shape would still occur. This deviation would result in a reduced diffusion length scale compared to a perfectly hemispherical drop, so the assumption of a perfect hemisphere will still provide an upper bound on the maximum protein concentration difference in an evaporating drop. The concentration of water is used in the above equation instead of the protein concentration. Use of the protein concentration and a constant evaporation flux leads to a Robin boundary condition at the surface that makes the analytical solution much more difficult. By using the concentration of water, only a constant flux condition results; although this may raise "red flags" initially due to the high values of the concentration measurement, it is noted that the solution retains its status as "dilute" as required by Fick's Law (Deen, 1998, Bird et al., 2007). The analytical solution for this system for evaporation rates that are slow enough that the change in radius in negligible compared to the diffusion is given by Crank (1975) as

$$C_0 - C = \frac{F_0 R}{D}\left[\frac{3Dt}{R^2} + \frac{r^2}{2R} - \frac{3}{10} - \frac{2R}{r}\sum_{n=1}^{\infty}\frac{\sin(\alpha_n r)}{\alpha_n^2 R^2 \sin(\alpha_n R)}\exp(-D\alpha_n^2 t)\right] \tag{B.6}$$

where the coefficients, α_n, are the solutions to

$$\alpha_n R \cot(\alpha_n R) = 1 \tag{B.7}$$

For large times, Equation B.3 simplifies to

$$C_0 - C = \frac{F_0 R}{D}\left[\frac{3Dt}{R^2} + \frac{r^2}{2R^2} - \frac{3}{10}\right] \tag{B.8}$$

The maximum concentration difference is then

$$\Delta C_{\max} = C\left(r = 0, t >> 1\right) - C(r = R, t >> 1) = \frac{F_0 R}{2D} \tag{B.9}$$

B.3 Validation and Conclusions

The solution from Crank agrees with a COMSOL (version 3.4.0.248) simulation for the hanging drop with no moving boundaries, constant evaporation flux, constant density, and a uniform initial concentration of water (Table B.1). When moving boundaries are introduced, the solutions from Crank at the largest and smallest radii are lower and upper bounds, respectively, for the COMSOL solution, as would be expected from geometric considerations. The COMSOL solution used the computational domain pictured in Figure B.2 with a 2D axisymmetric solver. Parameters for the system are given in Table B.2.

While the initial problem was non-trivial, here is presented a simple method to bound the concentration difference within an evaporating droplet. A bounded solution is useful when determining the value of the assumption of uniformity (i.e., with respect to concentration or temperature) as well as the stability of the process.

B.4 Figures

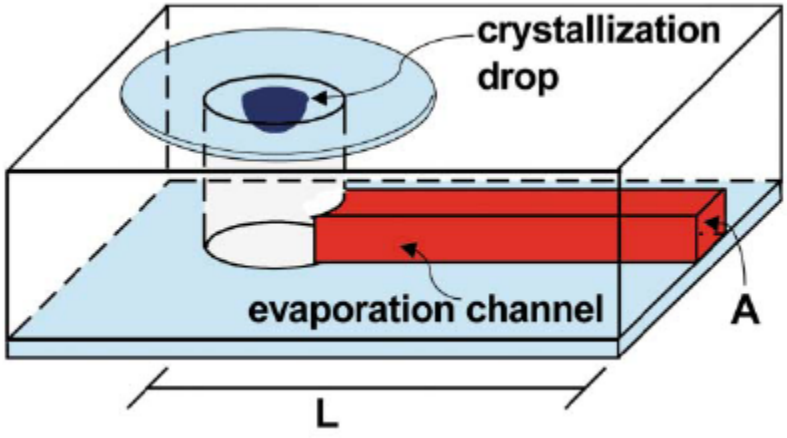

Figure B.1: A high throughput evaporation platform (Talreja et al., 2005).

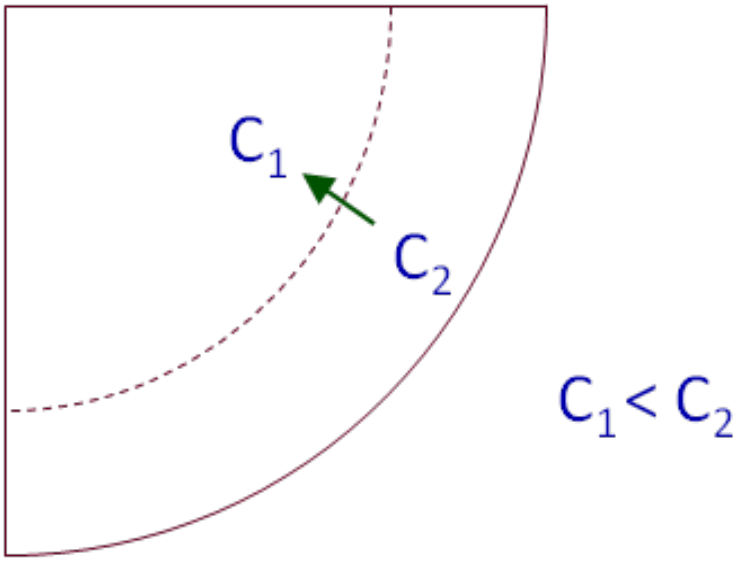

Figure B.2: The computational domain due to symmetry is half the hemispherical cross-section of an evaporating droplet. Evaporation causes the outer edge of the droplet to become more concentrated than the center.

B.5 Tables

Table B.1: Final minimum and maximum protein concentrations in a hanging drop during its evaporation from 2.0 to 1.6 mm. The Crank solution assumes constant radius. The row labeled "Var." shows the numerical results from COMSOL used a moving boundary as the droplet evaporated.

Radius (mm)	Method	Minimum (w/w)	Maximum (w/w)
2.0	COMSOL	0.1109	0.1156
2.0	Crank	0.1109	0.1156
1.6	Crank	0.1477	0.1546
Var.	COMSOL	0.1250	0.1299

Table B.2: Model parameters for the evaporating drop.

Parameter	Variable	Value
Evaporation Flux (kg/m^2-s)	F_0	2.0×10^{-6}
Diffusivity (m^2/s)	D	1.0×10^{-10}
Initial Protein Concentration (kg/m^3)	C_0	54
Protein Density (kg/m^3)	ρ_p	1025
Evaporation time	t	1.75×10^{5}

APPENDIX C

PITFALLS OF READILY AVAILABLE SOLUTIONS: PHYSICALLY CONSISTENT GLOBAL ANALYSIS OF SPECIES TRANSPORT FROM A SPHERICAL PARTICLE[1]

C.1 Problem Description

A common mistake when attempting to solve an engineering problem is to look up the solution from a textbook or paper, or to apply a mathematical technique, without carefully considering whether the solution or technique is actually valid. Numerous examples of this mistake arise in the literature on the analysis of the stability of dynamical systems, with some of the most common mistakes to avoid described in control textbooks and in past columns of IEEE Control Systems Magazine (Braatz, 2012; Goh et al., 2012; Braatz, 2012). This appendix gives an example of a more subtle mistake that can be used for setting up a teachable moment (Havighurst, 1953) for engineering students with a basic understanding of partial differential equations.

This particular example problem consists of assessing the global asymptotic stability of a system in which a molecular species is released from the external surface of a particle. The entry or release of molecules to/from the surfaces of particles arises in many industrial applications from commercial air conditioning systems (Wirz, 2009), to the removal of toxic chemicals from waste streams (Mangun et al., 1999; Ruthven, 1984), to the formation of protein crystals in microfluidic devices (Goh et al., 2010). In many of these applications, the concentrations of various species within the particle is of interest, for example, when

[1] This appendix was published as Rasche, M.L., Braatz, R.D., 2013. The pitfalls of readily available solutions: physically consistent global analysis of species transport from a spherical particle, IEEE Control Systems, 33 (5), 54-56.

determining the particle size that optimizes process efficiency or for developing an understanding of the spatiotemporal dynamics in fundamental studies (e.g. (Grant & Saville, 1991; Grant & Saville, 1995)). If the particle is solid, then the mass transfer of a species through the particle is via diffusion and is described by a linear model (Ruthven, 1984). If the particle is a liquid, then the mass transfer of a species through the particle is via convection and diffusion, and is described by a highly nonlinear model that is only solvable numerically, in which case the pure diffusion model can be used to compute analytical bounds on the maximum difference in species concentrations within the particle. As the species is released from the external surface of the particle, a concentration gradient develops in the particle, with the lowest concentration being at the external surface of the particle and the highest concentration in the center (Figure C.1).

Neglecting convection, the concentration of a species within an isothermal particle undergoing a constant flux at its external surface is described by the partial differential equation known as Fick's second law (Crank, 1975):

$$\frac{\partial C}{\partial t} = \frac{D}{r^2}\frac{\partial}{\partial r}\left(r^2 \frac{\partial C}{\partial r}\right), \tag{C.1}$$

$$C(r, t=0) = C_0, \tag{C.2}$$

$$-D\frac{\partial C}{\partial r}(r=R, t) = F_0, \tag{C.3}$$

$$\frac{\partial C}{\partial r}(r=0, t) = 0, \tag{C.4}$$

where $F > 0$ is the molar flux of a species being released from the external surface of the particle [(moles of species)/(external surface area of particle)(time), mol/m^{2}s], $C(r,t)$ is the species concentration [(moles of species)/(volume of solution), mol/m^3], D is a constant

diffusion coefficient of the species through the particle [m^2/s], r is the radial position ranging from the center of the particle at $r = 0$ to the outside surface of the particle at $r = R$ [m], and t is time [s]. Fick's second law (Equation C.1) follows from the insertion of Fick's first law (that is, that flux is proportional to the concentration gradient) into the mass conservation equation for the species molecules in the particle (Ruthven, 1984). The initial species concentration, C_0 [mol/m^3], is assumed to be spatially uniform in Equation C.2, and the particle is assumed to retain its spherical shape. The condition in Equation C.4 holds due to the assumed spherical symmetry of the particle. The problem statement with model (Equations C.1-C.4) is described in many publications including what most engineers would consider the definite book on the mathematics of diffusion (Crank, 1975).

The species concentration is the state variable in the model (Equations C.1–C.4). The student problem is to assess whether the system of equations is globally asymptoticall stable, that is, whether the state variable, $C(r,t)$, approaches a single steady-state value for long time regardless of the value of the initial state, $C(r,0) = C_0$.

One way to analyze the global asymptotic stability of a linear partial differential equation that does not require knowledge of Lyapunov theory (Krstic & Smyshlyaev, 2008), complex analysis (Curtain & Zwart, 1995), or the generalized Nyquist stability criterion (Desoer & Wang, 1980), is to analyze the boundedness of analytical solution for its state variable. An engineer well-versed in the solution of mass transfer problems will go to the most widely used book on the mathematics of diffusion (Crank, 1975) to look up the analytical solution for the model (Equations C.1–C.4), which is given as

$$C(r,t) = C_0 - \frac{FR}{D}\left[\frac{3Dt}{R^2} + \frac{r^2}{2R^2} - \frac{3}{10} - \frac{2R}{r}\sum_{n=1}^{\infty}\frac{\sin(\alpha_n r)}{\alpha_n^2 R^2 \sin(\alpha_n R)}\exp(-D\alpha_n^2 t)\right], \qquad \text{(C.5)}$$

where the coefficients, α_n, are solutions to

$$\alpha_n R \cot(\alpha_n R) = 1. \tag{C.6}$$

Alternatively, an engineer less familiar with mass transfer problems could directly apply the separation of variables (Crank, 1975) to obtain the analytical solution, Equations C.5–C.6. For large times, Equation C.5 simplifies to

$$C(r,t) = C_0 - \frac{FR}{D}\left[\frac{3Dt}{R^2} + \frac{r^2}{2R^2} - \frac{3}{10}\right]. \tag{C.7}$$

Based on inspection of either Equation C.5 or C.7, the obvious answer to question of global asymptotic stability is that the system is not stable, since each expression has a term that is a linear function of time, t, with all other terms being bounded for all time. But is this answer correct?

C.2 Discussion

Let's consider the actual physical system in which a species leaves a spherical particle with a nonzero flux over time. A species cannot have a negative concentration, so a physically consistent lower bound on the species concentration, $C(r,t)$, is zero. Continuous removal of the species from the particle would eventually deplete the species in the particle, so the species concentration at long time would be expected to approach zero; this physical understanding would suggest that the system is globally asymptotically stable. This asymptotic behavior is in direct contradiction to the analytical solution (Equations C.5–C.6) reported in the literature that indicates that the species concentration, $C(r,t)$, approaches negative infinity as time, t, goes to infinity.

Why does analysis based on the analytical solution (Equations C.5–C.6) produce an incorrect conclusion concerning stability? The key issue is that the original problem statement with model (Equations C.1–C.4), although published in many papers and textbooks, does not describe a physical problem for all time, t. An upper bound for values of the time, t, when the model (Equations C.1–C.4) is physically valid can be derived by writing an overall species balance on the particle,

$$\frac{4}{3}R^3 C_0 = 4R^2 F t_{\text{u.b.}}, \tag{C.8}$$

where $4R^3/3$ is the particle volume and $4R^2$ is the external particle surface area. Rearranging, this equation implies that the model (Equations C.1–C.4) cannot be physically valid for any time greater than

$$t_{\text{u.b.}} = \frac{RC_0}{3F}, \tag{C.9}$$

as any later time would attempt to release more species mass from the particle than was initially in the particle. At this point, a student might try to correct the analytical solution (Equations C.5–C.6) by including the condition that $t \le \frac{RC_0}{3F}$. Such a condition does not correct the problem, however.

A way to gain an understanding of why such reasoning would be invalid is to inspect Figure C.2 which is a plot of the analytical solution (Equation C.5) for different values of the flux F with

$$C_0 = 10{,}000 \text{ mol/m}^3, \tag{C.10}$$

$$D = 1.0 \times 10^{-13} \text{ m}^2/\text{s}, \tag{C.11}$$

$$R = 0.001 \text{ m}. \tag{C.12}$$

The species concentration becomes negative at some time before $t_{\text{u.b.}} = \frac{RC_0}{3F}$. For example, for the flux

$$F = 10^{-5} \text{ mol/m}^2, \tag{C.13}$$

the species concentration, C, at the external particle surface, $r = R$, computed from Equations C.5-C.6 is negative at time, $t = 10^{-5}$ seconds, which is less than $\frac{RC_0}{3F} = 3.33 \times 10^{-5}$ seconds. This analysis shows that the analytic solution (Equations C.5–C.6) becomes not physically meaningful at time much earlier than the time at which all of the species in the particle is depleted. The analytical solution (Equations C.5–C.6) is only a physically meaningful solution for the model (Equations C.1–C.4) as long as its predicted species concentration at the surface is nonnegative.

$$C(R,t) \geq 0, \tag{C.14}$$

which is equivalent to

$$3Dt - 2\sum_{n=1}^{\infty} \frac{1}{\alpha_n^2} \exp(-D\alpha_n^2 t) \leq \frac{DC_0 R}{F} - 1.7R^2. \tag{C.15}$$

Either inequality can be tested at time, t, to assess whether the solution remains physically meaningful. This solution exploits the information that the lowest species concentration occurs at the external surface, which can be argued from physical considerations or proving that $C(r,t)$ is a monotonically decreasing function in r.

C.3 Conclusions

The above discussion focusing on the analytical solution (Equations C.5–C.6) may give some students the impression that Equations C.5–C.6 are somehow at fault, but the problem

is really in the original problem statement, with Equations C.1–C.4. When the time, t, is high enough that the inequality (Equation C.15) is violated, the value of the specified constant flux, F, becomes higher than is physically possible, that is, higher than the species can diffuse through the particle to reach the external surface. For any constant positive flux at the surface, it is physically impossible for that flux to be constant at long time, due to the limitation in the rate at which the species can diffuse through the particle.

Now let's return to the question of global asymptotic stability. We have established that the original problem statement with the model given by Equations C.1–C.4 was not physically meaningful when specifying a positive constant flux for all time. So instead, consider the problem with the condition that the flux, F, is always positive but is some function of time that is physically selected so that the species in the particle can diffuse to the external surface at a high enough rate for the flux to be physically achievable. Now let's consider the global asymptotic stability for this modified system.

The simplest way to approach this stability analysis problem is to exploit some physical knowledge about the system, in this case, that the species concentration is directly related to the total mass of species in the particle. An overall species mass balance on the particle is

$$\frac{dm}{dt} = -4R^2 F(t), \tag{C.16}$$

where

$$m(t) = \int_0^R 4\pi r^2 C(r,t)\,dr \tag{C.17}$$

is the total mass of species in the particle, and $F(t) > 0, \forall t \geq 0$. The time derivative of the Lyapunov function, $V(m) = m^2$,

$$\frac{dV(m)}{dt} = 2m\frac{dm}{dt} = -8R^2 m(t)F(t) < 0, \forall t, \tag{C.18}$$

is negative definite, which implies that $m(t) \to 0$ as $t \to \infty$. From Equation C.17, this limit implies that

$$\int_0^R r^2 C(r,t)dr \to 0. \tag{C.19}$$

Since the flux was stated to be physically meaningful, $C(r,t) \geq 0$ for all r. This condition implies that the integrand in Equation C.19 is nonnegative for all r, so the limit in Equation C.19 can only hold if $C(r,t) \to 0$. This physically consistent system is globally asymptotically stable for any positive flux of species from its surface for all time.

C.4 Comments

In this particular diffusion problem, global asymptotic stability was proved simply by exploiting physical understanding of the problem. It is important to assign physical problems for analyzing stability to engineering students rather than mathematical abstractions. Otherwise, students will forget to take practical considerations into account once the model has been written, and will turn to a textbook, paper, Mathematica, or the World Wide Web to obtain an analytical solution without evaluating whether the problem statement or its solution is physically meaningful or correct.

C.5 Figures

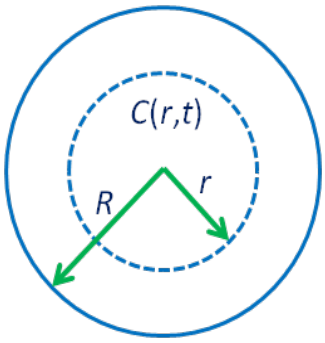

Figure C.1: A species of concentration, $C(r,t)$, diffusing through a spherical particle of radius, R, and released from its external surface produces a concentration gradient in the particle. The species release at the external surface, at $r = R$, causes the outer edge of the particle to become less concentrated than its interior.

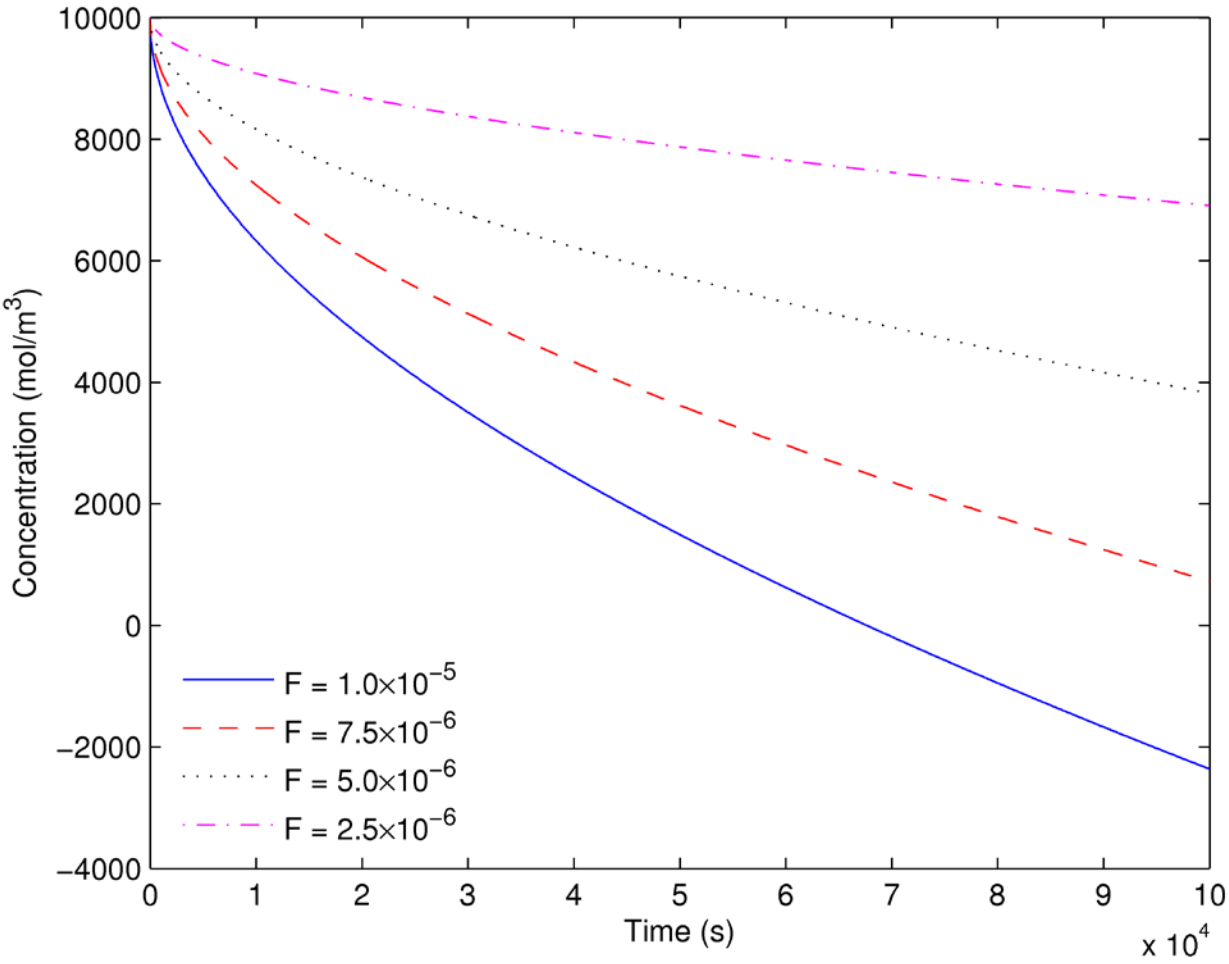

Figure C.2: Species concentration at the external surface, $C(R,t)$, in the spherical particle of radius, R, and with species released from its external surface at four different constant fluxes, F, as calculated from the analytical solution (Equations C.5–C.6). The values for the other system parameters are given in Equations C.10–C.12. The analytical solution is only physically meaningful when the species concentration is nonnegative.